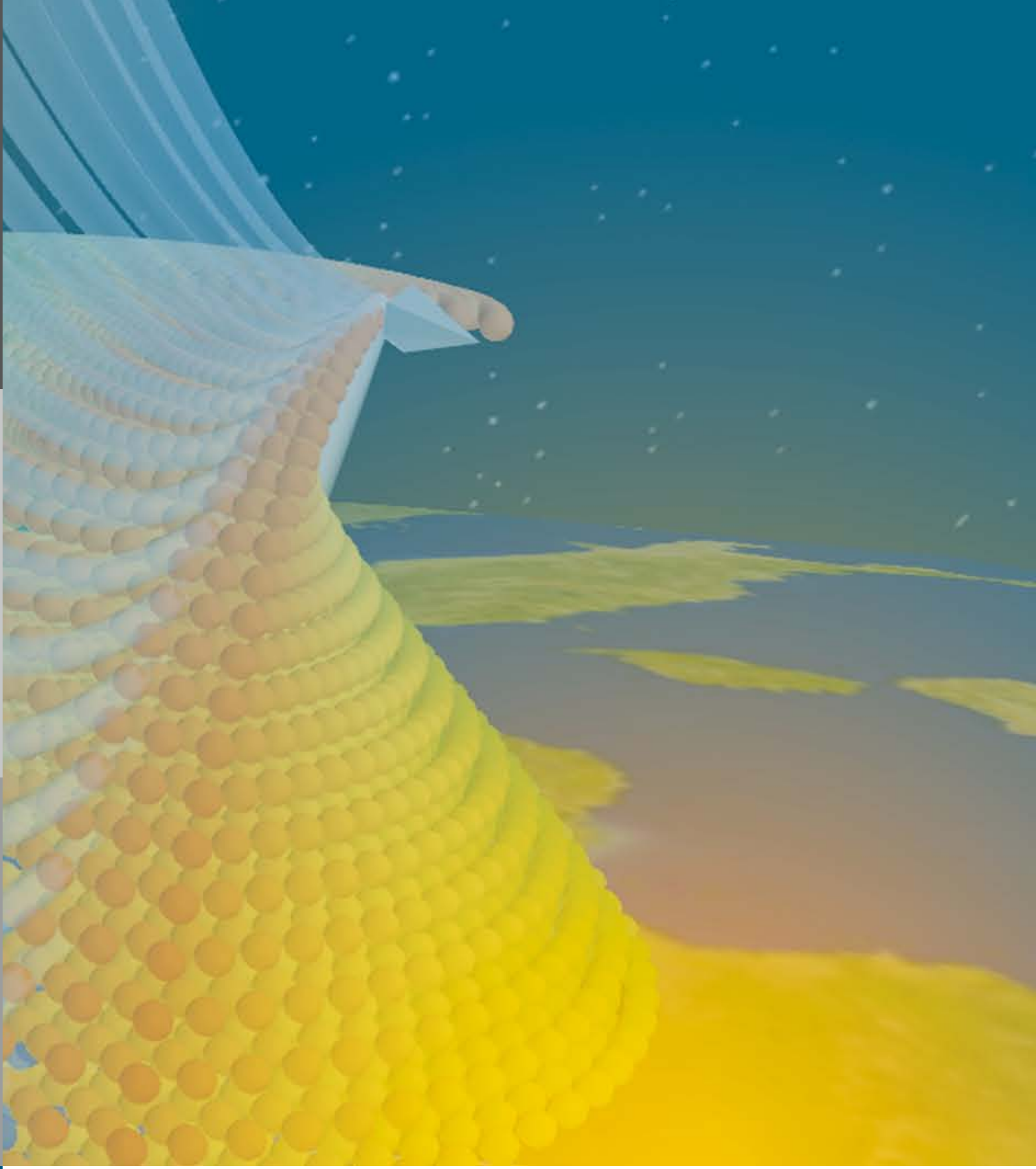

Tomographic reconstruction of atmospheric volumes from infrared limb-imager measurements

Jörn Ungermann

Mitglied der Helmholtz-Gemeinschaft

JÜLICH
FORSCHUNGSZENTRUM

Schriften des Forschungszentrums Jülich
Reihe Energie & Umwelt / Energy & Environment	Band / Volume 106

Forschungszentrum Jülich GmbH
Institute of Energy and Climate Research (IEK)
Stratosphere (IEK-7)

Tomographic reconstruction of atmospheric volumes from infrared limb-imager measurements

Jörn Ungermann

Schriften des Forschungszentrums Jülich
Reihe Energie & Umwelt / Energy & Environment Band / Volume 106

ISSN 1866-1793 ISBN 978-3-89336-708-5

Bibliographic information published by the Deutsche Nationalbibliothek.
The Deutsche Nationalbibliothek lists this publication in the Deutsche
Nationalbibliografie; detailed bibliographic data are available in the
Internet at http://dnb.d-nb.de.

Publisher and Distributor: Forschungszentrum Jülich GmbH
Zentralbibliothek
52425 Jülich
Phone +49 (0) 24 61 61-53 68 · Fax +49 (0) 24 61 61-61 03
e-mail: zb-publikation@fz-juelich.de
Internet: http://www.fz-juelich.de/zb

Cover Design: Grafische Medien, Forschungszentrum Jülich GmbH

Printer: Grafische Medien, Forschungszentrum Jülich GmbH

Schriften des Forschungszentrums Jülich
Reihe Energie & Umwelt / Energy & Environment Band / Volume 106

D 468 (Diss., Wuppertal, Univ., 2011)

ISSN 1866-1793
ISBN 978-3-89336-708-5

The complete volume ist freely available on the Internet on the Jülicher Open Access Server (JUWEL) at
http://www.fz-juelich.de/zb/juwel

Abstract

State-of-the art nadir and limb-sounders, but also in situ measurements, do not offer the capability to highly resolve the atmosphere in all three dimensions. This leaves an observational gap with respect to small-scale structures that arise frequently in the atmosphere and that still lack a quantitative understanding. For instance, filaments and tropopause folds in the upper troposphere and lower stratosphere (UTLS) are crucial for its composition and variability. One way to achieve a highly resolved three-dimensional (3-D) picture of the atmosphere is the tomographic evaluation of limb-imager measurements.

This thesis presents a methodology for the tomographic reconstruction of atmospheric constituents. To be able to deal with the large increase of observations and unknowns compared to conventional retrievals, great care is taken to reduce memory consumption and processing time. This method is used to evaluate the performance of two upcoming infrared limb-imager instruments and to prepare their missions.

The first examined instrument is the infrared limb-imager on board of PREMIER (Process Exploration through Measurements of Infrared and millimetre-wave Emitted Radiation), one of three remaining candidates for ESA's 7th Earth Explorer mission. Scientific goals of PREMIER are, among others, the examination of gravity waves and the quantification of processes controlling atmospheric composition in the UTLS, a region of particular importance for climate change.

Simulations based on the performance requirements of this instrument deliver a vertical resolution that is slightly better than its vertical field-of-view (about 0.75 km) and a horizontal resolution of ≈25 km × 70 km. Non-linear end-to-end simulations for various gravity wave patterns demonstrate that the high 3-D resolution of PREMIER considerably extends the range of detectable gravity waves in terms of horizontal and vertical wavelength compared to previous observations.

The second examined instrument is GLORIA (Gimballed Limb Observer for Radiance Imaging of the Atmosphere). This new remote sensing instrument combines a two-dimensional Fourier transform infrared spectrometer with a highly flexible gimbal mount. It is jointly developed by the Research Centre Jülich and the Karlsruhe Institute for Technology for deployment on the German research aircraft HALO (High Altitude and LOng range research aircraft) and the high-flying Russian aircraft Geophysica. GLORIA can be panned horizontally from 45° to 135° and thereby allows for tomographic measurements of mesoscale events for a wide variety of atmospheric constituents.

Ozone is used as a test species for optimising the flight path and measurement mode of the instrument for tomographic retrievals. For the first time, it is demonstrated that 3-D tomographic retrievals are possible using such an instrument with an unprecedented 3-D resolution of 200 m in the vertical direction and 20 to 30 km in the horizontal direction for special flight paths. The long duration of tomographic measurements necessitates the consideration of atmospheric advection. Its effect on tomographic retrievals is therefore quantified and partially compensated by a dedicated method.

Kurzfassung

Drei-dimensional (3-D) hochaufgelöste Messungen der Atmosphäre können weder von aktuellen Nadir- und Horizontsondierern noch von in-situ Messgeräten durchgeführt werden. Kleinskalige Strukturen können deshalb nicht in ihrer Gänze beobachtet werden und sind daher quantitativ schlecht verstanden. Ein Beispiel für solche Strukturen sind Filamente von Spurengasen oder auch Tropopausenfalten in der oberen Troposphäre und unteren Stratosphäre (UTLS), die entscheidend zur Zusammensetzung und Variabilität dieser Region beitragen. Eine Möglichkeit, ein hochaufgelöstes 3-D Bild der Atmosphäre zu erlangen, ist die tomographische Auswertung von Horizontsondierermessungen.

Diese Arbeit stellt eine Methode zur tomographischen Rekonstruktion von atmosphärischen Zustandsgrößen vor. Dazu muss eine deutlich größere Menge an Messungen und Unbekannten verarbeitet werden, als das für herkömmliche Retrieval der Fall ist. Das hier vorgestellte Auswerteverfahren ist daher darauf optimiert, den Speicherverbrauch und die Laufzeit des Retrievals möglichst klein zu halten. Seine praktische Anwendung findet das Verfahren bei der Beurteilung der tomographischen Retrievalqualität von zwei zukünftigen bildgebenden Infrarot-Horizontsondierern zur Vorbereitung ihres Einsatzes auf Messkampagnen.

Das erste dieser Instrumente ist der Infrarot-Horizontsondierer an Bord von PREMIER (Process Exploration through Measurements of Infrared and millimetre-wave Emitted Radiation), einem von drei verbliebenen Kandidaten für die siebte Earth Explorer Satellitenmission der ESA. Zwei wissenschaftliche Zielsetzungen von PREMIER sind u.a. die Untersuchung von Schwerewellen und die Quantifizierung der für die Zusammensetzung der UTLS relevanten Prozesse, da dieser Bereich der Atmosphäre von besonderer Bedeutung für den Klimawandel ist.

Mit simulierten Messungen durchgeführte tomographische Retrievalstudien ergeben ein vertikales Auflösungsvermögen, das etwas besser als das Gesichtsfeld des PREMIER Infrarot-Horizontsondierers (etwa 0,75 km) ist, und eine horizontale Auflösung von etwa 25 km × 70 km. Diese hohe 3-D Auflösung von PREMIER wird die Detektion von deutlich kurzwelligeren Schwerewellen erlauben, als das bisher möglich war.

Das zweite untersuchte Instrument ist GLORIA (Gimballed Limb Observer for Radiance Imaging of the Atmosphere). Dieses neue Fernerkundungsinstrument

verbindet ein zwei-dimensionales Fourier-Transformations-Infrarotspektrometer mit einem flexiblen Kardanrahmen. Diese Gemeinschaftsentwicklung des Forschungszentrums Jülich und des Karlsruher Instituts für Technologie soll auf dem deutschen Forschungsflugzeug HALO (High Altitude and LOng range research aircraft) und dem russischen Höhenflugzeug Geophysica zum Einsatz gebracht werden. GLORIA kann horizontal zwischen 45° und 135° geschwenkt werden und erlaubt dadurch tomographische Messungen von mesoskaligen Ereignissen für viele atmosphärische Spurengase.

Am Beispiel von Ozon wird die Auswirkung des Flugpfads und des Messmodus auf die tomographische Rekonstruktionqualität bestimmt. Für tomographische Flüge ist den Simulationen zufolge eine 3-D Auflösung von 200 m in der Vertikalen und 20 bis 30 km in der Horizontalen erreichbar. Die lange Messzeit eines solchen Fluges erfordert zwingend die Berücksichtigung der Advektion in der Atmosphäre. Ihr Einfluss auf das Ergebnis wird daher quantifiziert und mittels einer dedizierten Methode teilweise kompensiert.

Contents

1 Introduction **1**

2 A retrieval approach for large-scale inverse problems **9**

2.1 Inverse problems 9
2.2 Forward model 12
    2.2.1 Radiative transfer model 14
    2.2.2 Instrument model 15
    2.2.3 Error sources 17
    2.2.4 Discrete representation of the atmosphere 17
    2.2.5 Jacobian matrix calculation 19
2.3 Retrieval 21
    2.3.1 Regularisation 25
    2.3.2 Minimisers 28
    2.3.3 Solving linear sub-problems 32
2.4 Diagnostics 39
    2.4.1 Measurement contribution and resolution 40
    2.4.2 Retrieval noise 42
    2.4.3 Calculation of diagnostics using conjugate gradients 43
2.5 Chapter summary 44

3 Mesoscale gravity wave observations by the PREMIER IRLS **45**

3.1 Gravity wave observations by the PREMIER infrared limb-sounder 45
3.2 The PREMIER infrared limb-sounder 47
3.3 Simulation setup 49
3.4 Analysis of baseline setup 54
3.5 Gravity wave observational filter 58
    3.5.1 Deduction from end-to-end simulations 59
    3.5.2 Sensitivity to retrieval grid 61

3.5.3 Trade-off between retrieval noise and resolution 62
3.5.4 Comparison of 2-D and 1-D retrievals 64
3.5.5 Deducing the gravity wave observational filter from the averaging kernel matrix 65
3.5.6 Gravity wave observational filter for denser measurement grids 67
3.6 Chapter summary 69

4 A 3-D tomographic retrieval setup for the limb-imager GLORIA 71
4.1 The GLORIA infrared limb-imager 73
4.2 Simulation setup 75
4.3 Tracks following closed curves 81
4.3.1 Measurement geometry 81
4.3.2 Analysis of baseline setup 82
4.3.3 Choice of regularisation strength 87
4.3.4 Effect of panning 91
4.3.5 Choice and effect of flight track 93
4.3.6 Comparison with individual 1-D retrievals 94
4.4 Linear flight tracks 99
4.4.1 Analysis of linear flight track 100
4.5 Circular flight track with advection 103
4.5.1 4-D analysis of the baseline setup 104
4.5.2 Incorporating advection 107
4.5.3 Trajectory enhanced retrievals 109
4.6 Chapter summary 118

5 Summary and outlook 121

A Appendices 127
A.1 List of abbreviations 127
A.2 Mathematical notation 128
A.3 Algorithmic differentiation and adjoints 129
A.4 Setup of $\mathbf{L}_1^z$ for Tikhonov regularisation 133
A.5 Analytical inverse of $\mathbf{S_a}$ for the autoregressive model 134
A.6 Analytical root of $\mathbf{S_a}^{-1}$ for the autoregressive model 136
A.7 Conjugate gradient algorithm 136
A.8 Parametrisation of the conjugate gradient algorithm 137

Acknowledgments **141**

Bibliography **143**

List of Figures

1.1 The viewing geometry of a limb-sounder. 2
1.2 The observation geometry of PREMIER. 4
1.3 Tomographic flight paths for GLORIA. 5

2.1 Simulated radiance spectra for the GLORIA instrument operating in "dynamics mode" calculated with JURASSIC2. 14
2.2 Simulation of field-of-view. 16
2.3 A typical Jacobian matrix for a small 3-D retrieval setup. 20
2.4 A comparison of computation time for the evaluation of one Jacobian matrix using different methods. 21
2.5 Wall clock time and parallelisation speedup factor for the PREMIER baseline retrieval. 22
2.6 The computational effort for creating and decomposing the linear equation system matrix. 34
2.7 The required wall-clock time to solve a linear equation system for different problem sizes. 37
2.8 The memory consumption for different retrieval setups and dense or sparse inversion schemes. 38
2.9 The calculation of resolution along different axes. 42

3.1 Simulated radiance spectra for the PREMIER IRLS band A and B. 49
3.2 Illustration of the PREMIER IRLS dynamics mode measurement grid. 50
3.3 Line-of-sight of the central measurement track in the PREMIER IRLS dynamics mode. 51
3.4 The temperature weighting functions for the PREMIER IRLS at 12.6 µm for mid-latitude atmospheric conditions. 53

3.5 Retrieval end-to-end test used to generate the gravity wave observational filter. 55
3.6 The averaging kernel matrix row of a single atmospheric state vector element located in the middle of the atmosphere at 40 km height. 56
3.7 The measurement contribution for a baseline retrieval with no wave structure. 57
3.8 The vertical and horizontal resolution for a baseline retrieval with no modulated wave structure. 57
3.9 The gravity wave observational filter for the PREMIER IRLS. . . . 60
3.10 The gravity wave observational filter derived with a horizontal retrieval grid spacing of 50 km. 61
3.11 The effect of vertical correlation length on vertical resolution and noise error. 63
3.12 The retrieval result for a series of conventional 1-D retrievals and a 2-D retrieval. 65
3.13 The gravity wave observational filter derived by a series of a 1-D retrievals. 66
3.14 The gravity wave filter as deduced from the averaging kernel matrix. 66
3.15 The gravity wave observational filters for different horizontal measurement grids. 68

4.1 The design of the GLORIA instrument. 72
4.2 Simulated limb radiance spectra of the GLORIA instrument operating in dynamics mode. 75
4.3 Simulation of ozone distribution by the GEM-AQ model. 76
4.4 Radiances and transmittance for an exemplary retrieval setup. . . 79
4.5 The accuracy of $\boldsymbol{F}$ and $\mathbf{F}'$ in relation to the number of pencilbeams used to simulate a single image. 80
4.6 The visualisation of a circular flight path. 82
4.7 Two cutting planes through the full 3-D true atmospheric state. . 83
4.8 The retrieval result of the baseline setup with added instrument noise. 83
4.9 The retrieval result of the baseline setup without added instrument noise. 84
4.10 3-D averaging kernel matrix rows for two retrieved ozone values. 85
4.11 The vertical resolution of the baseline setup. 86

4.12 The horizontal resolution in longitudinal direction of the baseline setup. 87
4.13 The effect of different regularisation strengths. 89
4.14 The L-curve for the baseline setup. 91
4.15 A tomographic retrieval without panning. 92
4.16 The retrieval result and relative error of a tomographic reconstruction with panning being reduced to 50°. 92
4.17 Visualisation of a square flight path and relative retrieval error. . . 94
4.18 Visualisation of an octagonal flight path and relative retrieval error. 95
4.19 The retrieval result for 12 km height of 1-D retrievals. 96
4.20 The rays of an exemplary 1-D retrieval. 97
4.21 The rows of gain and averaging kernel matrices for 12 km altitude. 98
4.22 The effect of the assumption of horizontal homogeneity on a single 1-D retrieval. 98
4.23 The atmospheric situation and measurement geometry of the linear flight track numerical experiment. 100
4.24 The retrieval result for a linear flight track. 101
4.25 The horizontal resolution for a linear flight track. 101
4.26 3-D averaging kernel matrix rows for two retrieved ozone values for the linear flight track. 102
4.27 A comparison between one row of the 3-D averaging kernel matrix and its 4-D/3-D equivalent for a central element. 105
4.28 A comparison between one row of the 3-D averaging kernel matrix and its 4-D/3-D equivalent for a border element. 106
4.29 The temporal change caused by advection. 110
4.30 The retrieval result of a run with advection and perfect a priori knowledge thereof. 111
4.31 3-D averaging kernel matrix rows that are slightly outside the region encircled by the instrument. 112
4.32 Horizontal and vertical resolution of a retrieval with perfect wind speed knowledge. 113
4.33 The retrieval result of a run with advection and no compensation during the retrieval. 114
4.34 The atmospheric state averaged over time and the relative error of the retrieval result without wind compensation. 114

4.35 The resolution of the retrieval without a priori wind speed information related to the atmospheric state prevalent during the first measurement. 116
4.36 The retrieval result of a run with advection and an averaged a priori wind speed knowledge. 117
4.37 The resolution of the retrieval run with advection and an averaged a priori knowledge. 118

A.1 The effect of parameterising the conjugate gradient scheme on solving tomographic problems. 138

List of Tables

3.1 PREMIER IRLS instrument characteristics. 48

4.1 GLORIA instrument characteristics. 74
4.2 Regularisation strength for 3-D retrieval experiments. 77

A.3 The conjugate gradient algorithm in pseudo code. 137

Far better an approximate answer to the right question,
which is often vague,
than an exact answer to the wrong question,
which can always be made precise.

(John W. Tukey)

1. Introduction

Remote sensing is the act of measuring physical quantities without being in physical contact with the measured object. It has a long tradition in atmospheric sciences, starting with the measurement of ozone by Dobson (1968) in the 1920's. Remote sensing has the unique advantage that a large volume of air can be examined from a distance, whereby in situ measurements must bring an instrument into the air mass to be examined. Combining a remote sensing instrument with a fast moving carrier, for example an aircraft or a satellite, gives the opportunity to get mesoscale or even global coverage.

An important subfield of remote sensing in atmospheric science is passive infrared limb-sounding. Figure 1.1 shows the principal viewing geometry of such a limb-sounder. This technique measures infrared radiation emitted by molecular vibrational and rotational bands along the ray path or line-of-sight (LOS) of the instrument, which is directed towards the limb of the Earth's atmosphere. The point of the LOS closest to the surface is called the tangent point and the shortest distance between the tangent point and the surface of the Earth is called the tangent altitude. The LOS is curved towards the surface due to refraction. As the atmosphere is densest at the tangent point, the part of the LOS around this location generally contributes most to the measured radiation if absorption can be neglected. Limb-sounders typically take measurements at different tangent altitudes to collect information about the vertical structure of the atmosphere.

Using, e.g., an interferometer, one can spectrally resolve the measured radiance to reveal characteristic emission and absorption bands. Many important trace gas species exhibit emission bands within the mid-infrared spectral region that coincides with an "atmospheric window", which is a spectral region that is nearly transparent from the surface of the Earth to space. From the intensities of the spectrally resolved radiance measurements, temperature, a variety of trace gases, aerosols, clouds, etc. can then be simultaneously deduced. This

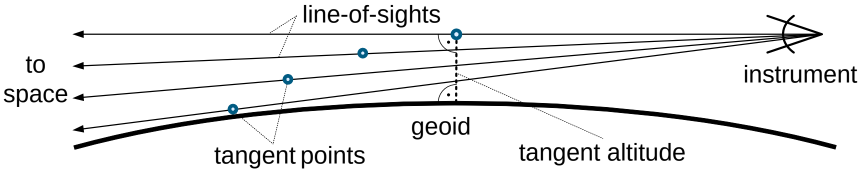

Figure 1.1: The viewing geometry of a limb-sounder.

makes infrared limb-sounding very efficient for the examination of a wide range of trace gas species.

Numerous previous satellite missions have used the infrared limb-sounding technique for atmospheric remote sensing. Global observation of atmospheric infrared limb-emissions represents a reliable technique to obtain vertically resolved profile data of atmospheric constituents, at daytime and at nighttime. First global infrared limb-emission observations of an extensive number of atmospheric trace gas species were made by LIMS (Limb Infrared Monitor of the Stratosphere; Gille and Russel III, 1984) and SAMS (Stratospheric and Mesospheric Sounder; Drummond et al., 1980) aboard the Nimbus 7 satellite. Trace gas fields obtained from these sensors and follow-on instruments such as the CRISTA instrument (Cryogenic Infrared Spectrometers and Telescopes for the Atmosphere; Riese et al., 1997; Offermann et al., 1999) greatly contributed to our understanding of the three-dimensional composition, structure and large-scale dynamics of the middle atmosphere. Early 2002, ESA launched Envisat, a polar-orbiting Earth observation satellite, which includes the MIPAS instrument (Michelson Interferometer for Passive Atmospheric Sounding; Fischer et al., 2008) for infrared limb-emission observations with high spectral resolution. MIPAS significantly expanded the number of detectable species and the corresponding height range compared to previous space missions. The recent HIRDLS (High Resolution Dynamics Limb Sounder; e.g. Gille et al., 2003) on board of the NASA Aura satellite offers a very dense along track spacing of measurements of less than 100 km, albeit at a rather large azimuth angle with respect to its orbital plane. The close spacing of HIRDLS measurements could extend our knowledge on gravity waves by providing absolute values of gravity wave momentum flux (Alexander et al., 2008; Wright et al., 2009) using the techniques developed by Ern et al. (2004).

Aircraft carriers allow examining finer structures in great detail but lack the coverage provided by satellites. Current limb-emission sensors such as MIPAS-

STR (Michelson Interferometer for Passive Atmospheric Sounding on STRatospheric aircraft; e.g. Höpfner et al., 2001; Keim et al., 2008) and CRISTA-NF (Cryogenic Infrared Spectrometers and Telescopes for the Atmosphere - New Frontiers; e.g. Spang et al., 2008; Hoffmann et al., 2009; Weigel et al., 2010) on-board the high-flying Russian aircraft Geophysica provide adequate spatial sampling in two dimensions (vertical and along the flight track).

Due to technological limitations, all previous instruments have used telescopes with scanning mirrors or one-dimensional detector arrays to obtain profile information of atmospheric trace species. Thereby, they were restricted to take relatively few measurements. For satellites, hundreds of kilometres usually lie between consecutively measured profiles. Also, the special viewing geometry of limb-sounders inherently provides a very good vertical sampling and consequently vertical resolution, but has difficulties to deliver a good horizontal resolution along the LOS. This becomes problematic when dynamic structures of the atmosphere shall be examined that are smaller than 200 km, a typical figure for the achievable resolution of limb-sounders along their LOS.

Such small-scale structures arise frequently in the atmosphere. They are not well understood, as they cannot yet be properly observed by current in situ, limb, or nadir observations (nadir sounders look vertically from space to earth). Quite often, model calculations are the only way to examine such structures. For example, simulations of deep convection in the tropics found that forced small-scale gravity waves are seemingly quite influential for the quasi-biennial oscillation (Piani et al., 2000; Lane et al., 2001). However, such waves are not observable by current in situ or remote sensing instruments and the smallest of these will remain so for some time. Another example are mesoscale structures like filaments and tropopause folds in the upper troposphere/lower stratosphere (UTLS), which are crucial for the UTLS composition and variability (Konopka et al., 2009). While limb-sounders offer a sufficient vertical resolution, their horizontal resolution only allows for undistorted retrievals, if the usually long-drawn atmospheric structure is properly aligned with the LOS of the instrument (e.g. Weigel, 2009). As numerical simulations for dynamic structures are currently not accurate enough to reliably predict the exact location and sometimes even existence of structures of interest, one cannot ensure the proper alignment of the measuring instrument with the structure at hand. Consequently, remote sensing instruments with high resolution along all three spatial axes are required to properly examine such structures and increase our knowledge about the atmosphere.

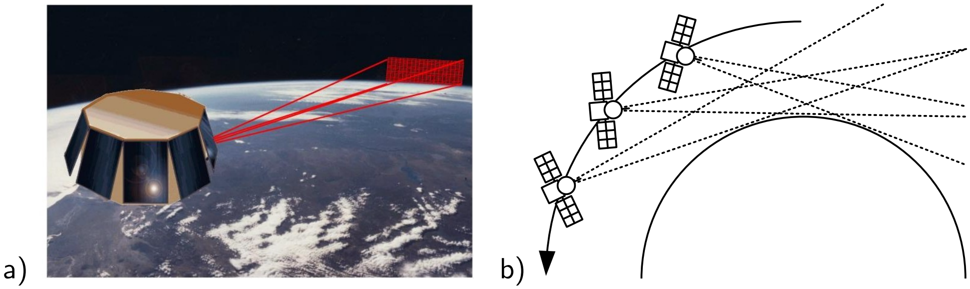

Figure 1.2: The observation geometry of PREMIER. Panel **(a)** shows a single image that provides ≈10 000 simultaneous limb-views within the altitude range from ≈3 to 55 km and with a swath width of 320 km (reprinted from Riese et al., 2005). The overlapping of consecutively taken images is shown in panel **(b)**. In practise, the measurement density is much denser than depicted here.

One way to improve the achievable resolution in the desired way is tomography, which employs multiple views of the same volume from different angles to produce a spatially resolved reconstruction of the examined object (e.g. Natterer, 2001). First steps towards tomographic evaluation of satellite measurement data have already been taken by combining the measurements of multiple consecutive vertical profiles to recreate a 2-D slice of atmosphere with presumably better horizontal resolution. Such retrievals for limb-sounding measurements were first explored by a variety of authors for different purposes and instruments (e.g. Solomon et al., 1984). Practical implementations for the large-scale retrieval of atmospheric constituents from satellite measurements were first produced by Carlotti et al. (2001) for MIPAS and Livesey et al. (2006) for the Microwave Limb Sounder. However, current infrared limb-sounding satellites were not designed for tomographic evaluation and either do not measure along their orbital plane or their horizontal sampling is too coarse to fully exploit the potential of tomographic evaluation.

Recent advances in measurement technology offer the opportunity to lift previous limitations. New two-dimensional detector technology has become available that allows for the implementation of limb-imaging techniques with an unprecedented spatial sampling as shown in Fig. 1.2. The PREMIER infrared limb-sounder (Process Exploration through Measurements of Infrared and millimetre-wave Emitted Radiation; a candidate for ESA's 7th Earth Explorer mission; see Chap. 3) and the GLORIA instrument (Gimballed Limb Observer for Radiance Imaging of the Atmosphere; see Chap. 4) are the first instruments exploiting

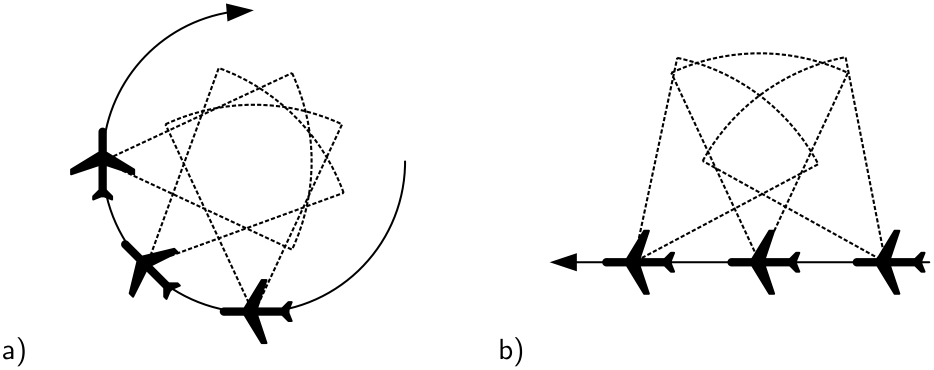

Figure 1.3: Tomographic flight paths for GLORIA. A circular flight path is schematically shown in panel **(a)**, while a linear flight path is depicted in panel **(b)**. In practise, the measurement density is much denser than depicted here.

this technology for infrared limb-sounding. They will be able to take an unprecedented number of spectral and spatial samples allowing, for the first time, a true three-dimensionally resolved reconstruction of the atmosphere. The PREMIER infrared limb-sounder will achieve this aim by individually reconstructing several parallel 2-D slices, while GLORIA measurements require a full 3-D reconstruction. Either way, the large number of involved measurements makes this a daunting task, as hundred thousands up to millions of spectral samples need to be combined and evaluated within a single reconstruction of an atmospheric representation of similar size. Handling problems of such size is inherently difficult and requires dedicated algorithms with tuned implementations to keep memory consumption and processing time manageable, even for high-performance computers. Most state of the art algorithms and retrieval systems from the field of atmospheric remote sensing cannot deal with such a huge amount of data.

For the evaluation of PREMIER infrared limb-sounder measurements, proven concepts for 2-D tomography suffice, whereas the 3-D tomographic evaluation of measurements made by the GLORIA instrument is a new conceptual approach for atmospheric limb-sounding. In this work, measurements from an air-borne limb-sounder are for the first time truly three-dimensionally evaluated. Figure 1.3 shows the tomographic measurement principle for GLORIA, which relies on the capability to pan the instrument to measure the same volume from multiple angles. The 3-D tomographic retrieval is not a simple extension of 2-D tomography due to the different observation geometries between forward- or backward-looking satellite instruments and side-ways looking air-borne instruments on the one hand and due to the different carrier speeds on the other hand. For instance, a satellite-borne instrument moves fast enough so that the atmospheric state does not change significantly between measurements with overlapping LOSs (see Fig. 1.2(b)), whereas performing an air-borne tomographic measurement flight as shown in Fig. 1.3(a) may take hours. Further, retrieving a 3-D volume from measurements taken during a typical linear flight path of its air-borne carrier as shown in Fig. 1.3(b) poses a notoriously difficult limited-angle problem (e.g. Natterer, 2001, p.144ff), as the atmospheric volume cannot be measured from all directions. Lastly, large parts of the LOSs of GLORIA measurements run through parts of the atmospheric volume, which cannot be viewed from multiple angles (and therefore not resolved with good quality) for practical matters.

Consequently, this thesis provides an encompassing framework for the tomographic evaluation of new limb-imager instruments. For the first time, it is possible to practically evaluate such large-scale problems. The following main questions will be examined in detail:

- How to best ensure the existence and uniqueness of a physically meaningful solution of large-scale 2-D or 3-D inversion problems?
- How to numerically solve and diagnose the regularised inverse problem posed by 2-D or 3-D tomographic retrievals?
- What kind of spatial resolution can be expected from near-future limb-imager instruments?
- How does the flight path of the carrier influence the achievable retrieval result for air-borne limb-imager instruments?
- How does the temporal variability of the atmosphere relate to the slow carrier speed of air-borne carriers in the context of 3-D tomographic retrievals?

Answering these questions allows estimating the future performance of the new PREMIER infrared limb-sounder and GLORIA. For PREMIER, these results are available early enough to ascertain or re-evaluate requirements regarding its measurement geometry. For GLORIA, answers to these questions are a necessary prerequisite to properly plan and execute its first campaign planned for autumn 2011.

Following these main questions, Chap. 2 introduces the inverse problem posed by the evaluation of infrared limb-emission spectra in the context of atmospheric science. It describes the mathematical problem and provides an overview over tomographic inversion techniques and numerical algorithms currently in use, concluding with a new algorithm that, for the first time, allows performing large-scale three-dimensional retrievals in the context of atmospheric limb-sounding including the calculation of diagnostic information.

With the retrieval algorithm available, first a 2-D problem is examined in Chap. 3 by a study of the proposed PREMIER infrared limb-sounder instrument. A 2-D tomographic retrieval setup is presented that is comparatively straightforward to handle and replicates setups already in practical use, for example for MIPAS (Carlotti et al., 2001). Still, it is a very demanding and complex task that requires an efficient treatment, especially as the PREMIER infrared limb-sounder will produce two orders of magnitudes more measurements than previous instruments, which all need to be evaluated in near-real time. The achievable spatial resolution of the PREMIER infrared limb-sounder is examined and it is determined how this benefits the detection of gravity waves, one of the main scientific goals of the PREMIER mission.

The most challenging use case, the 3-D tomographic evaluation of measurements of the GLORIA instrument, is presented in Chap. 4. This work examines the feasibility of the approach and demonstrates the successful 3-D retrieval of ozone for a circular flight pattern. It then proceeds to examine the effect of different flight routes on the retrieval and also investigates the effect of the variability of the atmosphere during the measurement period. A framework is presented that allows to examine, quantify, and compensate the influence of advection on 3-D tomographic retrievals.

The greatest challenge to any thinker is stating the
problem in a way that will allow a solution.

(Bertrand Russell)

2. A retrieval approach for large-scale inverse problems

This chapter presents a short overview of the mathematics behind the reconstruction of atmospheric constituents from remote sensing measurements, a process that is usually called retrieval. A special focus is placed upon treating large-scale, tomographic retrieval problems involving several hundred thousands of unknowns and measurements. The mathematical notation used in this and the following chapters is described in appendix A.2, where also the most important mathematical symbols are collected.

2.1. Inverse problems

An inverse problem is given, when any function $\boldsymbol{F} : \mathbb{R}^n \mapsto \mathbb{R}^m$ shall be inverted. Thereby, $\boldsymbol{F}$ is usually straightforward to evaluate but not easily invertible. The term “inverse problem” directly brings to mind: the inverse of what? Mainly for historical reasons, the corresponding direct problem is often the prediction of the future development or emissions of a system from its current state. Quite often this was examined earlier than the inverse problem, which tries to invert the process, to calculate the evolution of the system backward in time, or to derive the system state from its emissions. One finds that inverse problems do not often have a solution in the strict sense, which means that the solution might not exist, might not be unique, and/or might be very sensitive to any measurement errors (Engl et al., 1996, p. 3).

Accordingly, an inverse problem is called well-posed, if all of the following conditions are met (Hadamard, 1902):

1. the problem has a solution,
2. the solution is unique, and

3. the solution depends continuously on the data.

Otherwise, the problem is called ill-posed.

In the field of atmospheric passive infrared limb-sounding, an inverse problem consists of reconstructing an atmospheric state from radiance measurements made by, e.g., an interferometer. In this case, the function $\boldsymbol{F}$ maps the atmospheric state, for example a discretised vertical profile, onto emission spectra of different tangent altitudes. Simulating these emission spectra is the forward problem; its implementation is called the forward model and is referred to by $\boldsymbol{F}$. The forward model used in this work is presented in Sect. 2.2, where also the modelled physical processes are briefly discussed. The atmospheric state describes temperature, pressure, and abundance of trace gases. Using a discrete representation, it is possible to model the radiative transfer and the instrument effects to generate simulated "ideal" measurements $\boldsymbol{y}_\mathrm{t} \in \mathbb{R}^m$, which are unaffected by measurement errors. Thereby, $\boldsymbol{F}$ represents the actual physics as accurately as possible under consideration of physical understanding, knowledge about the instrument, and also performance constraints. For simplicity's sake, this work does not formally distinguish between the true physical processes and the approximations thereof implemented in the forward model as a more rigorous analysis would require.

The measurements are affected by various error sources (see Sect. 2.2.3). Representing these errors by $\boldsymbol{\epsilon} \in \mathbb{R}^m$ and capturing the true state of the atmosphere by $\boldsymbol{x}_\mathrm{t} \in \mathbb{R}^n$, the sampling of the real measurements $\boldsymbol{y} \in \mathbb{R}^m$ can be mathematically described as

$$\boldsymbol{y} = \boldsymbol{F}(\boldsymbol{x}_\mathrm{t}) + \boldsymbol{\epsilon}. \tag{2.1}$$

The inverse problem is then defined as finding an atmospheric state $\boldsymbol{x} \in \mathbb{R}^n$ that is mapped by the forward model $\boldsymbol{F}$ onto the measured $\boldsymbol{y}$:

$$\boldsymbol{x} = \boldsymbol{F}^{-1}(\boldsymbol{y}). \tag{2.2}$$

This process is called retrieval and the practicalities of performing the actual inversion for large-scale, tomographic problems are dealt with in Sect. 2.3. Please note that the measurement error vector $\boldsymbol{\epsilon}$ does not appear in Eq. (2.2), as it cannot be separated from the measurements in practice. Due to the addition of $\boldsymbol{\epsilon}$, $\boldsymbol{y}$ may not lie within the image of $\boldsymbol{F}$, which would imply that the inverse of $\boldsymbol{F}$ is not defined for $\boldsymbol{y}$. This introduces problems even for normally well-posed problems and turns them into an ill-posed one. However, the reconstruction of an atmospheric state from limb-emission spectra is an ill-posed problem regardless (e.g. Geppert, 2010), so that special care needs to be taken to approximate it by a well-posed one. Usually, it is thus impossible to perfectly reconstruct the true state $\boldsymbol{x}_\mathrm{t}$ and an approximation $\boldsymbol{x}_\mathrm{f} \in \mathbb{R}^n$ with known error bounds is the best one can achieve.

First, one has to assure that the inverse problem has a solution. This can be achieved by relaxing the definition of solution. Instead of requiring an exact solution as in Eq. (2.2), the $\boldsymbol{x}$ that minimises the expression

$$\min_{\boldsymbol{x}} \|\boldsymbol{F}(\boldsymbol{x}) - \boldsymbol{y}\|_2 \tag{2.3}$$

is selected instead. In this way, the non-linear inversion problem is approximated by a non-linear minimisation problem, which always has at least one solution. If a solution of the original problem exists, it is also a solution of the minimisation problem. Solving such minimisation problems is a standard task of numerical optimisation unless the problem size becomes as large as given for 3-D tomographic problems involving hundred thousands of measurements and unknowns. In Sect. 2.3.2, algorithms employed in recent 2-D tomographic evaluations of satellite measurements (e.g. Carlotti et al., 2001, 2006; Steck et al., 2005; Livesey et al., 2006) are examined and are found to be not suitable for 3-D problems. Instead, a more scalable algorithm based on Newton-type minimisers and iterative linear equation system solvers is presented in the same section.

Second, one has to assure the uniqueness of the solution. The lacking uniqueness is usually handled by adding constraints to the minimisation problem that add so called “a-priori knowledge” into the problem. The simplest constraint is to choose the least square solution $\boldsymbol{x}$ with the smallest norm $\|\boldsymbol{x}\|_2$. In atmospheric remote sensing, typically more complex constraints are used, which are described in Sect. 2.3.1. The basic idea is to discard solutions that contradict common knowledge about the atmosphere.

Third, one has to deal with the problem that the solution may not depend continuously on the measurements. Due to the discretisation usually employed, which transforms the problem from an infinite-dimensional, continuous one to a finite-dimensional, discrete one, continuity is usually less problematic and problems may arise “only” from the non-linearity of $\boldsymbol{F}$. However, the problem is almost certainly still ill-conditioned, meaning that small variations in the measurements $\boldsymbol{y}$ caused by measurement errors can cause large oscillations in the least-square solution. Gladly, either problem is also mitigated by the introduction of proper a priori constraints.

Once a solution is attained, it is important to quantify how it may deviate from the true state of the atmosphere and what influence is exerted on the solution by measurement noise and a priori constraints. The solution is essentially meaningless without this diagnostic information. Therefore, the chapter concludes by describing a method for analysing the errors and distortions of the retrieval result of large-scale retrievals with respect to the true state of the atmosphere.

2.2. Forward model

The forward model simulates the radiative transfer in the atmosphere along the line-of-sight (LOS) including instrument effects to accurately describe how much spectral radiance is measured by an infrared limb-sounder instrument for a given atmospheric state, naturally excluding measurement errors.

Assuming a local thermodynamic equilibrium and neglecting scattering, the spectral radiance of a given wave number ν arriving at the instrument from a certain direction can be described as

$$I(\nu) = \int_0^\infty B(\nu, T(s)) \frac{d\tau(\nu, s)}{ds} ds, \tag{2.4}$$

integrating along the LOS (s) starting at the instrument location ($s = 0$). The Planck function B is defined as

$$B(\nu, T) = \frac{c_1 \nu^3}{\exp(\frac{c_2 \nu}{T}) - 1} \tag{2.5}$$

with spectroscopic constants c_1 and c_2 and temperature T. The transmissivity τ is given as integral along the LOS between the instrument ($x = 0$) and the position s:

$$\begin{aligned}\tau(\nu, s) = \exp\Bigg(&- \int_0^s \sigma_{\text{ext}}(\nu, x) dx \\ &- \sum_i \sum_j \int_0^s k_{ij}(T(x)) f_{ij}(\nu, p(x), T(x)) \rho_i(x) dx \Bigg).\end{aligned} \tag{2.6}$$

Thereby p is pressure, σ_{ext} is the aerosol extinction coefficient, k_{ij} is the line strength, f_{ij} is the line profile of emitter i and spectral line j, and ρ_i is the density of emitter i. From the equations above, it is easy to see the non-linear relationship between temperature, pressure, and emitter densities on the one hand and received radiation on the other.

To accurately model the radiation measured by the detector, the field-of-view (FOV) and instrument-line-shape (ILS) need to be accounted for. The sensitivity of the interferometer for all directions (FOV) is represented by the weighting function $w_1^k(\phi,\theta)$, which is defined on the sphere (with azimuth $\phi \in [0,2\pi]$ and elevation angle $\theta \in [-\pi/2,\pi/2]$). Naturally, the support (that is the set of points where the function is non-zero) of the w_1^k is much smaller and covers usually only a few degrees for azimuth and elevation with an even better localised peak (see Fig. 2.2 for an example). The sensitivity of the detector for radiance at different wave numbers (ILS) for measurement k is modelled by a second weighting function $w_2^k(\nu)$ determining the spectral resolution. Using these functions, the radiance obtained from an idealised measurement (i.e. a single element of $\boldsymbol{y}$ without measurement errors) is given by

$$I^k = \int_0^{2\pi} \int_{-\pi/2}^{\pi/2} w_1^k(\phi,\theta) \int_0^{\infty} w_2^k(\nu) I(\nu,\phi,\theta) d\nu d\theta d\phi. \tag{2.7}$$

$I(\nu,\phi,\theta)$ is the I of Eq. (2.4) with a line integral in the direction defined by the angles ϕ and θ taking into account refraction. Each I^k determines one element of the vector of measurements $\boldsymbol{y}$.

Some exemplary results of such a forward calculation can be seen in Fig. 2.1. Usually, not the full spectral range is simulated, but one focuses on emission lines of individual species, like the CO_2 Q-branch located around 12.6 µm.

A fast radiative transfer model is essential to solve large inverse problems in atmospheric remote sensing. The Python/C++ based Jülich Rapid Spectral Simulation Code Version 2 (JURASSIC2) was developed to efficiently handle imager instruments and tomographic retrievals. It is based on JURASSIC (Hoffmann, 2006), which was previously used as forward model for the evaluation of several satellite- and air-borne remote sensing experiments (e.g. Hoffmann et al., 2008, 2009; Eckermann et al., 2009; Hoffmann and Alexander, 2009; Weigel et al., 2010).

The implementation of the forward model $\boldsymbol{F}$ is split into a non-linear function $\boldsymbol{P} : \mathbb{R}^n \mapsto \mathbb{R}^p$ simulating the radiative transport including the ILS (i.e. the inner integral of Eq. (2.7), further detailed in Sect. 2.2.1) and a linear function $\boldsymbol{H} : \mathbb{R}^p \mapsto \mathbb{R}^m$ simulating the instrument characteristics excluding the ILS (described in Sect. 2.2.2) with $\boldsymbol{F}(\boldsymbol{x}) = \boldsymbol{H}(\boldsymbol{P}(\boldsymbol{x}))$.

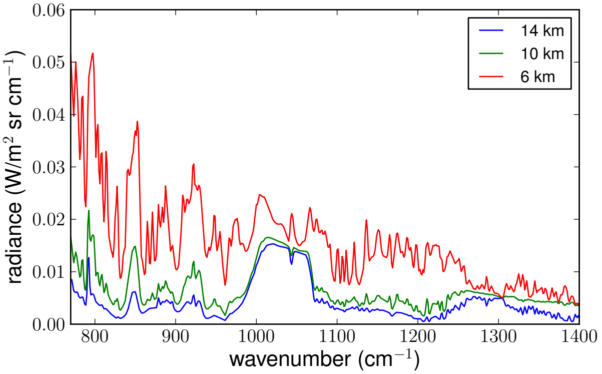

Figure 2.1: Simulated radiance spectra for the GLORIA instrument operating in "dynamics mode" (see Chap. 4) calculated with JURASSIC2. Given are three spectra taken from an observer altitude of 15 km altitude and pointing to tangent heights of 6, 10, and 14 km. The employed atmospheric situation is described in Sect. 4.2.

2.2.1. Radiative transfer model

A single radiative transfer calculation of JURASSIC2 simulates an infinitesimal thin beam of radiation, also called a "pencilbeam" that neglects effects of FOV, etc. Each pencilbeam maps the atmospheric state onto a single radiance value. To properly capture FOV effects, each measurement usually requires the simulation of multiple pencilbeams looking into different directions. As usually many measurements need to be simulated, each evaluation of the forward model $\boldsymbol{F}$ usually requires the computation of thousands of pencilbeams. The function $\boldsymbol{P}$ represents the evaluation of all pencilbeams and the combination of all simulated radiances into a single vector of length p.

Each pencilbeam is determined by an observer position, a viewing direction, and a spectral range. First, a ray-tracing step is performed using a flexible 3-D ray-tracing routine (Hase and Höpfner, 1999). The outcome of the ray-tracing is a LOS as shown in Fig. 1.1. The atmosphere is interpolated along the LOS using an appropriate interpolation function (see Sect. 2.2.4). The representation of the LOS and thus the ray-tracing step length is crucial for the accuracy of the forward model. The step length must be small enough to sample variations of the atmosphere with sufficient accuracy. This was examined in detail by Hoffmann (2006) for horizontally stratified atmospheres. For other atmospheres, additional care needs to be taken so the step length is small enough to also sample all horizontal variations (see also Sect. 4.2). This ray-tracing creates the path needed by Eq. (2.4).

Using this interpolated LOS, the emissivity growth approximation method (EGA; e.g. Weinreb and Neuendorffer, 1973; Gordley and Russell, 1981 is applied to approximate the rightmost integral of Eq. (2.7). Compared to conventional line-by-line calculations, this approach is about a factor 1 000 faster, since the radiative transfer is based on pre-calculated spectrally averaged values of emissivity stored in lookup tables that account already for the ILS. The emissivity lookup tables for the forward model are prepared by means of exact line-by-line calculations utilising the Reference Forward Model (RFM; Dudhia et al., 2002). Please refer to Hoffmann (2006) for a comprehensive discussion of the radiative transport model. Processing actual GLORIA measurements of the troposphere will likely require additional steps to reduce the error introduced by the approximate EGA method. One such scheme was implemented by Weigel (2009) in JURASSIC and was used to successfully evaluate measurements made by the air-borne CRISTA-NF instrument. It combines the EGA method with the Curtis-Godson Approximation (CGA; Curtis, 1952; Godson, 1953) and a linear regression based on the radiance supplied by the EGA and CGA method and several minor predictors based on Francis et al. (2006) to significantly reduce the error of the forward model.

2.2.2. Instrument model

JURASSIC2 provides a flexible handling of different types of observation geometries, for instance nadir, sub-limb, limb, or zenith viewing and even combinations thereof within a single retrieval. In addition, FOV effects of the instrument can be simulated using a generic scheme that also allows for the combination of instruments with different characteristics in a single setup.

Each measurement is affected by the FOV of the instrument. FOV in this context encompasses the effects due to finite size of the detector pixels, cross-talks on the 2-D detector array, and refraction within the instrument. These are simulated by a FOV weighting function w_1 over azimuth and elevation angles that is convoluted with the radiance coming from the given directions. To account for the effect of the FOV, JURASSIC2 discretises the FOV weighting function and performs several pencilbeam calculations per measurement.

A simple case with only two measurements is shown in Fig. 2.2. Two observations with typical vertical spacing and FOV for the discussed limb-imagers are shown as coloured horizontal lines. To simulate these observations, in this ex-

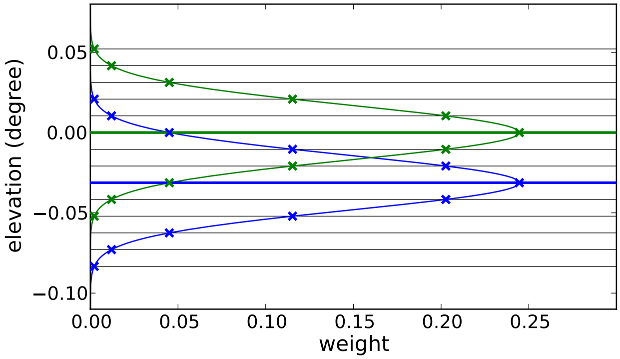

Figure 2.2: Simulation of FOV. The green and blue horizontal lines represent simulated instrument measurements taken at different elevation angles and the black lines represent calculated pencilbeams. The Gaussian describing the vertical FOV of each measurement is shown in the same colour as its associated instrument measurement. The weight with which each pencilbeam radiance enters the simulated measurement is indicated by coloured crosses.

ample more than three times as many pencilbeams are employed that are shown as black lines. Each observation has a FOV with a full width at half maximum (FWHM) of 0.04° shown in the appropriate colour. The weight with which each pencilbeam enters the observations is shown by the coloured crosses. If the weight drops below a threshold the pencilbeam is disregarded for an observation. Please note that individual pencilbeams typically influence multiple observations.

The discretisation of the FOV weighting function depends in turn on the representation of the atmospheric state. If the atmosphere is by design horizontally homogeneous, the FOV needs to be sampled only in the vertical direction (as in Fig. 2.2), whereas for an atmosphere varying in all three spatial dimensions the FOV weighting function needs to be sampled both in azimuth and elevation direction requiring additional pencilbeams in the horizontal direction. As a matter of simplification, the pencilbeams are not cast from the location of the individual detector pixel, but from the centre of the detector array. This allows the reuse of a single pencilbeam for the simulation of measurements from different detector pixels and has no effect on the calculated radiance. Especially for imager instruments that take many measurements in fixed spatial relationship towards one another, this enables a drastic reduction of required computation time. Consequently, the instrument model $\boldsymbol{H}$ consists of a pre-calculated linear map, which combines the radiances of the pencilbeams provided by $\boldsymbol{P}$ to error-free simulated measurements.

In addition, $\boldsymbol{H}$ also modifies the measurements with a multiplicative gain and an additive offset component. It is possible to assign the same gain or offset component to arbitrary measurements. For instance, it is possible to have a single unique offset for all images, a unique offset per image, an individual offset per detector pixel, or completely arbitrary assignments. In addition, it is possible to correlate the parameters according to time of the measurement, spectral wave length of measurement, azimuth angle of measurement, and elevation angle of measurement.

2.2.3. Error sources

The measurements are subject to both stochastic and systematic errors (jointly captured in ϵ), while the forward model is only affected by systematic errors. A stochastic error is defined as an error that has a mean of zero averaged over many measurements and is usually assumed to have a Gaussian distribution. A typical stochastic error would be white additive noise on the measurements. Systematic errors on the other hand can have a wide range of sources. This ranges from peculiarities of the employed detector over uncertainties in spectroscopic data for the various emitters to simplifying assumptions within the forward model.

The software JURASSIC2 supports to simulate and retrieve an additive offset and a multiplicative gain component as instrument effects for individual or multiple measurements with a wide range of spectral, spatial, and temporal correlation options. The error covariance matrix describing the error can be set up to include uncertainties with respect to quantities that are not retrieved, for example the concentration of relevant but not retrieved trace gas species, uncertainties of spectroscopic data and various other systematic error sources. FOV effects and detector cross-talks are modelled within the instrument model.

A thorough discussion of error analysis is given by Rodgers (2000, p.48ff) and will not be repeated here as the methodological studies presented later in this work assume only stochastic Gaussian noise as error source for simplicity's sake.

2.2.4. Discrete representation of the atmosphere

The atmospheric state needs to be stored in a finite discrete representation, for which the JURASSIC2 forward model internally uses a four-dimensional atmosphere (three spatial and one temporal dimension). JURASSIC2 is however capable of assuming and exploiting homogeneity for various dimensions. For instance, one can assume that trace gas concentrations vary only vertically and are thereby horizontally homogeneous and static in time. This gives the classic 1-D atmosphere (i.e. a vertical profile). But also 2-D slices, 3-D volumes, and even time-varying atmospheres are possible that account for atmospheric variability within a measurement period. Requests for atmospheric constituents at a certain location and time are mapped to an appropriate interpolation routine for the discrete representation of the chosen atmosphere type. The atmosphere consists of temperature, pressure, aerosol and a configurable number of trace gas species. In the following, the most important atmospheric representations and interpolation routines are shortly described. These interpolations are mostly used to map the discrete state of the atmosphere onto temperature and trace gas concentrations along the LOSs of the pencilbeams.

The classic 1-D representation stores one vertical profile, meaning that latitude, longitude and time information are disregarded for this interpolation. This representation assumes spherical symmetry, meaning that the atmosphere is horizontally homogeneous. All entities except pressure and aerosol are interpolated linearly. Pressure and aerosol are interpolated exponentially (i.e. the logarithm of their value is interpolated linearly and then the exponential function is applied on the result).

The 2-D representation stores a number of vertical profiles following a great circle. First the two vertical profiles closest to the point to be interpolated are identified. These profiles are vertically interpolated (like a 1-D profile above) according to the altitude of the point. The point is then projected onto the plane spanned by the two profiles and the result of the two vertical interpolations is weighted according to the distance of the projected point from the two profiles. Time information is ignored for 2-D interpolation.

The 3-D representation uses a rectilinear grid of longitudes, latitudes and altitudes. The grid structure allows for easy identification of the four profiles surrounding a point to be interpolated. Each of the four profiles performs a vertical interpolation (like for a 1-D atmosphere) and the results are combined using bilinear interpolation according to the horizontal coordinates. Time information is ignored for 3-D interpolation. A 3-D natural neighbour interpolation (e.g. Sibson, 1981) for irregular data (e.g. for processing data generated by atmospheric trajectory models) is also implemented, but is currently too slow to practically perform retrievals with it.

Lastly, two 4-D representations are implemented in JURASSIC2. The first just adds time as a fourth dimension to the rectilinear 3-D representation so that the final bi-linear interpolation step is replaced by a tri-linear one including time.

The second uses a trajectory model to simulate advection and is described in detail in Sect. 4.5.2.

2.2.5. Jacobian matrix calculation

Many inversion algorithms do not only need to evaluate $\boldsymbol{F}$ but require also the Jacobian matrix $\mathbf{F}'$ (also called the kernel matrix) that contains the derivatives of the measured radiance values with respect to atmospheric state variables and instrument parameters. Further, the Jacobian matrix is an important diagnostic quantity, as its rows consist of the weighting functions that indicate which part of the atmosphere contributes most to the received radiance of a given single measurement.

Each column of the Jacobian matrix can be approximately calculated by the finite difference of $(\boldsymbol{F}(\boldsymbol{x}+\boldsymbol{h})-\boldsymbol{F}(\boldsymbol{x}))/\|\boldsymbol{h}\|_2$, where $\boldsymbol{h} \in \mathbb{R}^n$ perturbs only one element of $\boldsymbol{x}$. Given a fast enough forward model and exploiting the sparsity of the Jacobian matrix, this approach is feasible even for tomographic problems. A sparse matrix is a matrix, which consists mostly of zero entries. Still, calculating the full Jacobian matrix in this way is the most time-consuming feature of the retrievals presented later in this work.

The Jacobian matrix $\mathbf{F}'(\boldsymbol{x})$ of $\boldsymbol{F}$ for typical tomographic 2-D or 3-D problems is sparse, as a single measurement is influenced only by a small fraction of the volume defined by $\boldsymbol{x}$. For example, Fig. 2.3 shows a Jacobian matrix for a 3-D tomographic retrieval from simulated GLORIA measurements employing a circular flight track (as shown schematically in Fig. 1.3(a)). About 99 % of the matrix entries are zero. The vertical stripes are caused by the order of the atmosphere points and the wave-like structure is a consequence of the circular flight path.

This sparsity can be exploited to speed up the calculation of the Jacobian matrix with finite differences. By generating a data structure that tracks, which points of the atmosphere influence which pencilbeams, it is possible to simply skip the calculation of pencilbeams unaffected by the current perturbation. In effect, generating zeros within the Jacobian matrix consumes nearly no processing time. This technique results in an overall speedup of ≈100 for the type of problems considered here.

JURASSIC2 also offers means to employ algorithmic differentiation (e.g. Giering and Kaminski, 1998) for the calculation of $\mathbf{F}'$. Algorithmic differentiation exploits the chain rule and partial derivatives to calculate the exact directional derivative (to machine accuracy) of a function implemented in a programming

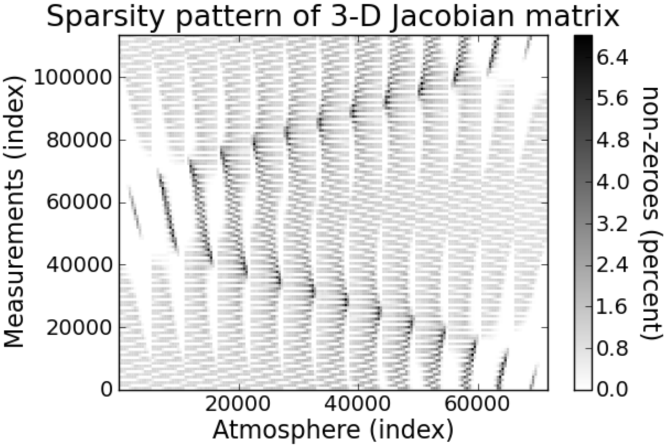

Figure 2.3: A typical Jacobian matrix for a small 3-D retrieval setup consisting of 71 487 atmosphere points and 113 600 measurements. The colour code of each dot represents the number of non-zero matrix entries for 3×3 full vertical profiles and twelve consecutive images comprised of 768 measurements.

language during its execution (Lotz, 2010). A brief introduction into the topic of algorithmic differentiation and its applications in JURASSIC2 is given in appendix A.3. Using in particular the adjoint approach, the computational effort for calculating the Jacobian matrix $\mathbf{F}'$ is only a small constant factor times the effort for evaluating $\boldsymbol{F}$ instead of the factor $n+1$ required for pure finite differences. This becomes obviously the more advantageous the larger the treated problem sizes are. As the option to efficiently calculate the Jacobian matrix with this method became available only recently, the numerical experiments presented in Chap. 3 and 4 all use finite differences with tracking.

The efficiency of the three methods is compared in Fig. 2.4. The time required to calculate the Jacobian matrix is depicted for three different use-cases and three different methods. On the left is a very simple 1-D test case. Here, half of the Jacobian matrix consists of zeros, so the computation with tracking (“FD+TRK”) brings a speed-up of about two compared to pure finite differences (“FD”). Even for this small test case, the adjoint method of computation (“ADJ”) is much faster. For the larger 2-D and 3-D test cases, the speed-up is even more pronounced. While finite differences with tracking is ≈100 times faster than pure finite differences, the algorithmic differentiation provides another factor of ≈100, being therefore ≈10 000 times faster than pure finite differences for the two examined tomographic problems on the right.

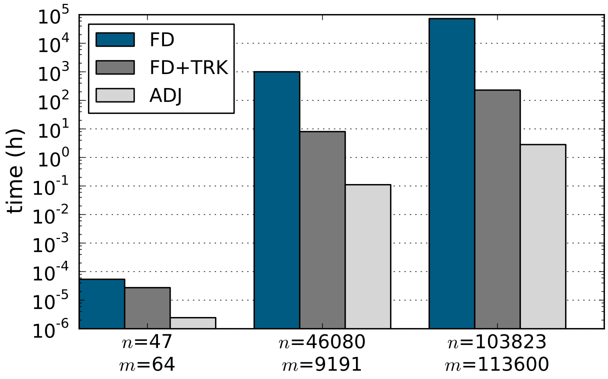

Figure 2.4: A comparison of computation time for the evaluation of one Jacobian matrix using different methods. Three different problems representing single-target 1-D, 2-D and 3-D problems are used as example. The method "FD" uses finite differences without any optimisation. The method "FD+TRK" exploits the sparsity of the Jacobian matrix to calculate only the non-zero entries with finite differences. The method "ADJ" uses algorithmic differentiation. No parallelisation was employed.

Another way to reduce the wall-clock time needed for the calculation of the Jacobian matrix is parallelisation. Figure 2.5 shows the speedup of a full retrieval using finite differences with tracking for the Jacobian matrix calculation realised with an OpenMP parallelisation of the forward model. From the curve can be deduced that about 93% of the retrieval code are parallelised.

2.3. Retrieval

This section describes how to derive an atmospheric state from limb-sounder measurements, a process that is usually called retrieval. First, the fundamentals are presented, whereas the succeeding sections fill in the details. As the employed algorithms and their implementations are of utmost importance when dealing with large-scale problems, a slightly technical overview over the algorithms recently employed in (2-D) tomographic atmospheric remote sensing and related fields is provided, concluding with a scalable algorithm suitable for 3-D retrievals.

The inversion of the forward model $\boldsymbol{F}$ presents a non-linear, ill-posed, and in many cases both under-determined and over-determined inversion problem.

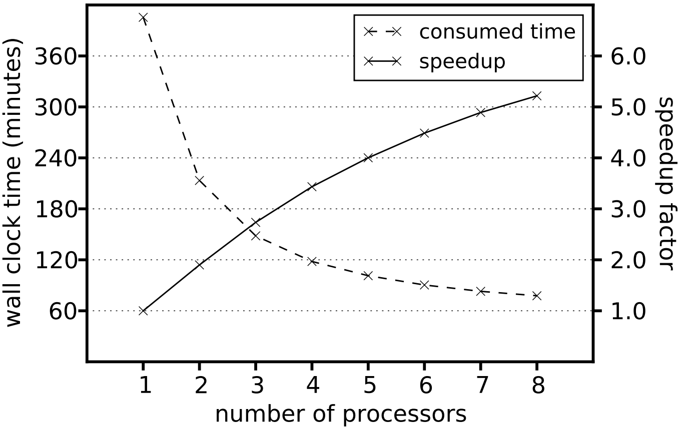

Figure 2.5: Consumed wall clock time and achieved speedup factor for the PREMIER baseline retrieval (see Sect. 3.3) if an OpenMP parallelisation is applied.

This implies that no exact solution may exist, as the measurement noise may cause the measurements $\boldsymbol{y}$ to lie outside the image of $\boldsymbol{F}$ (i.e. no $\boldsymbol{x} \in \mathbb{R}^n$ exists with $\boldsymbol{F}(\boldsymbol{x}) = \boldsymbol{y}$). If fewer measurements than retrieval targets are given, the solution is under-determined and thereby certainly not unique. If measurements are repeated or are not independent from one another, differing measurement errors cause the problem to be over-determined. Further, the discretised problem is usually ill-conditioned in the way that small changes in the measurements $\boldsymbol{y}$ (e.g. due to measurement errors) cause large changes in the solution $\boldsymbol{x}$.

The first step in handling the ill-posedness is to approximate the inversion problem by a least-squares minimisation problem as given in Eq. (2.3). This ensures the existence of a solution, but not its uniqueness. One way to obtain a unique and physically reasonable solution is regularisation. Regularisation usually approximates the original ill-posed problem by a similar well-posed problem. Aside the regularising effect of discretisation itself, this thesis makes use of an additional quadratic constraint on the solution, which encompasses the regularisation techniques “Tikhonov regularisation” (e.g. Tikhonov and Arsenin, 1977; Twomey, 1977) and “optimal estimation” (e.g. Rodgers, 2000; Tarantola, 2004). Thereby, the regularised problem converges in the limit to the original problem, when the added constraint is reduced towards zero.

These constraints represent so called a priori knowledge about the state of the atmosphere and thereby ensure a physically meaningful solution. Thereby, the vector $\boldsymbol{x}_\mathbf{a} \in \mathbb{R}^n$ is the a priori knowledge about the state of the atmosphere, representing usually a climatological mean of the retrieved quantities. The matrix $\mathbf{S}_\mathbf{a} \in \mathbb{R}^{n\times n}$ is a covariance matrix for the a priori state $\boldsymbol{x}_\mathbf{a}$. Please note that $\mathbf{S}_\mathbf{a}$ does not need to be invertible in the strict sense, even though the inverse matrix $\mathbf{S}_\mathbf{a}^{-1} \in \mathbb{R}^{n\times n}$, the precision matrix, is used often in the following formulas. In fact, the precision matrix is quite often directly derived from smoothness constraints and its singularity requires the use of a Moore-Penrose pseudo-inverse to derive $\mathbf{S}_\mathbf{a}$, if desired. The vector $\boldsymbol{y}$ represents the measurements and $\mathbf{S}_\epsilon \in \mathbb{R}^{m\times m}$ represents the covariance matrix of the measurement error. The matrix $\mathbf{S}_\epsilon$ is assumed to be diagonal (or at least block-diagonal or block-Toeplitz), which means that the inverse matrix $\mathbf{S}_\epsilon^{-1}$ has the same sparse structure and can be efficiently calculated.

To approximate the ill-posed original problem with a well-posed new one, Equation (2.3) is modified by adding a second term to the minimisation problem defining the regularisation constraint. Furthermore, adding a weighting matrix $\mathbf{S}_\epsilon^{-1}$ that adjusts the influence of measurements according to their error (i.e. pre-whitening) results in the cost function $J : \mathbb{R}^n \mapsto \mathbb{R}$ with

$$J(\boldsymbol{x}) = (\boldsymbol{F}(\boldsymbol{x})-\boldsymbol{y})^\mathrm{T}\mathbf{S}_\epsilon^{-1}(\boldsymbol{F}(\boldsymbol{x})-\boldsymbol{y}) + (\boldsymbol{x}-\boldsymbol{x}_\mathbf{a})^\mathrm{T}\mathbf{S}_\mathbf{a}^{-1}(\boldsymbol{x}-\boldsymbol{x}_\mathbf{a}). \tag{2.8}$$

If both covariance matrices $\mathbf{S}_\mathbf{a}$ and $\mathbf{S}_\epsilon$ are set up “realistically”, the minimum of J defines a statistically optimal weighted average between the a priori information and the information contained in the measurements. But also by using ad hoc approximations for the covariance matrices, physically meaningful solutions can be derived.

In the field of atmospheric remote sensing, the cost function J is usually minimised using Newton-type methods, which are presented in detail in Sect. 2.3.2. Newton-type methods are based on the idea of finding the minimum of J by finding a root of $\boldsymbol{J}'$, as this is a necessary condition for a minimum of J. Expanding $\boldsymbol{J}'$ around the current location into a first order Taylor approximation and solving for the point where $\boldsymbol{J}'(\boldsymbol{x}) = 0$ gives a simple Newton iteration for finding a root of $\boldsymbol{J}'$:

$$\boldsymbol{x}_{i+1} = \boldsymbol{x}_i - \mathbf{J}''(\boldsymbol{x}_i)^{-1}\boldsymbol{J}'(\boldsymbol{x}_i). \tag{2.9}$$

Approximating the Hessian matrix $\mathbf{J}''(\boldsymbol{x}_i)$ by dropping all terms involving the second order derivative of $\boldsymbol{F}$ results in the well-known Gauss-Newton iteration scheme (e.g. Nocedal and Wright, 2006, p. 254ff.):

$$x_{i+1} = x_i - \underbrace{\left(\mathbf{S}_\mathbf{a}^{-1} + \mathbf{F}'(x_i)^\mathrm{T}\mathbf{S}_\epsilon^{-1}\mathbf{F}'(x_i)\right)^{-1}}_{\approx\frac{1}{2}J''(x_i)^{-1}} \cdot \underbrace{\left(\mathbf{S}_\mathbf{a}^{-1}(x_i - x_\mathbf{a}) + \mathbf{F}'(x_i)^\mathrm{T}\mathbf{S}_\epsilon^{-1}\left(F\left(x_i\right) - y\right)\right)}_{=\frac{1}{2}J'(x_i)}. \quad (2.10)$$

The factor of $\frac{1}{2}$ in both derivatives of J can be dropped as one searches for a root of J'. The second order derivative of F is prohibitively costly to calculate and often negligible, as the problem at hand is only “slightly” non-linear. However, for strongly non-linear problems, this approximation worsens the convergence speed. Eq. (2.10) requires in each iteration the solution of a linear equation system with n unknowns. For tomographic problems, the size of these linear equation systems requires special attention and, finally, iterative solvers as explained in Sect. 2.3.3. If m is smaller than n, a different formulation of the problem is more efficient as it only requires the solution of a smaller linear equation system. The following formula is equivalent to Eq. (2.10), but uses $\mathbf{S}_\mathbf{a}$ and $\mathbf{S}_\epsilon$ instead of their inverses and requires the solution of a linear equation system with m unknowns (Rodgers, 2000, p.97):

$$x_{i+1} = x_\mathbf{a} + \mathbf{S}_\mathbf{a}\mathbf{F}'(x_i)^\mathrm{T}\left(\mathbf{F}'(x_i)\mathbf{S}_\mathbf{a}\mathbf{F}'(x_i)^\mathrm{T} + \mathbf{S}_\epsilon\right)^{-1} \cdot \left(y - F(x_i) + \mathbf{F}'(x_i)(x_i - x_\mathbf{a})\right). \quad (2.11)$$

A different, perhaps more intuitive, approach for deriving the Gauss-Newton iteration scheme is to reformulate the problem by using a first order Taylor approximation of the forward model F around the last location x_i:

$$\begin{aligned} J(x_{i+1}) &= (F(x_{i+1}) - y)^\mathrm{T}\mathbf{S}_\epsilon^{-1}(F(x_{i+1}) - y) + (x_{i+1} - x_\mathbf{a})^\mathrm{T}\mathbf{S}_\mathbf{a}^{-1}(x_{i+1} - x_\mathbf{a}) \\ &\approx \left\| \begin{pmatrix} \mathbf{S}_\epsilon^{-\frac{1}{2}}\mathbf{F}'(x_i) \\ \mathbf{S}_\mathbf{a}^{-\frac{1}{2}} \end{pmatrix} x_{i+1} - \begin{pmatrix} \mathbf{S}_\epsilon^{-\frac{1}{2}}(y - F(x_i) + \mathbf{F}'(x_i)x_i) \\ \mathbf{S}_\mathbf{a}^{-\frac{1}{2}}x_\mathbf{a} \end{pmatrix} \right\|_2^2 \end{aligned} \quad (2.12)$$

Finding the x_{i+1}, for which J is minimal, is a typical linear minimisation problem in x_{i+1} and can be treated as such to find the next location. Using the normal equation, the resulting formula is identical to Eq. (2.10). But Eq. (2.12) offers also a numerically more stable way of generating the next location by employing the more stable QR-decomposition. It is also the basis of the LSQR algorithm, which is prevalent in seismological remote sensing (e.g. Nolet, 1985).

In the following, the details of this approach are presented: how to construct $\mathbf{S_a^{-1}}$ in Sect. 2.3.1, what minimisers to employ in Sect. 2.3.2 and how to best solve the linear equation systems posed by Newton-type methods in Sect. 2.3.3.

2.3.1. Regularisation

The regularisation constraint selects one solution among possibly many and dampens the influence of measurement errors on the retrieval result. The regularisation matrix $\mathbf{S_a^{-1}}$ in combination with the vector $\boldsymbol{x}_\mathbf{a}$ represents the a priori knowledge about the true state of the atmosphere available before evaluating the measurements. If accurate means and an associated covariance matrix are available and employed, the approach is called optimal estimation and delivers a statistically optimal result of combining a priori information with the measurements. Obviously, if they were available, this approach should be taken in most cases.

Unfortunately, accurate covariances are difficult to obtain in practise. To derive accurate climatologies needed to construct the required covariances, consistent in situ measurements of a wide range of trace gases on a global scale over a long time and altitude range would be required. Using global satellite measurements might bias the results due to systematic retrieval errors. Also, climatologies are necessarily derived from past data and, by design, cannot reflect recent developments in composition of the atmosphere (for instance, the constant increase in CO_2), biasing retrieval results against reproducing such changes.

The climatology of Remedios et al. (2007) is currently the most comprehensive climatology with respect to number of contained trace gas species used in the evaluation of infrared limb-sounding. It contains means and variances, but no covariances. Calculating covariances of 1-D profiles would be achievable for some species, but is currently not widely used. Calculating covariances for two- or even three-dimensional atmospheric representations is currently not possible due to a lack of a sufficient amount of spatially resolved data, unless one were willing to base the calculation on data generated by global models.

In effect and practice, the matrix $\mathbf{S_a^{-1}}$ can be considered a freely definable tuning parameter. The statistical interpretation of the matrices and the results remain valid as long as $\mathbf{S_a}$ fulfils the formal requirements of a covariance matrix, which is being symmetric and positive semi-definite. However, the approach should be called optimal estimation only, if $\mathbf{S_a}$ models the variances and covariances to the best available knowledge. According to this strict definition, this thesis does not employ optimal estimation.

For tomographic retrievals, it will prove crucial to work with sparse matrices (see Sect. 2.3.3), which are matrices consisting mostly of zeros. Consequently, two ways to construct a sparse precision matrix $\mathbf{S_a}^{-1}$ are given in the following.

Autoregressive model

Several methods for defining a matrix $\mathbf{S_a}$ with set variances exist in literature (e.g. Tarantola, 2004, p. 111ff). A standard approach for 1-D covariance matrices is the first order autoregressive model, which assumes that neighbouring layers are correlated (e.g. Steck and von Clarmann, 2001). Extending this approach to higher dimensions while retaining the unique and desirable characteristic of a cheap analytical inverse gives:

$$(\mathbf{S_a})_{i,j} = \sigma_i \sigma_j e^{-\frac{|z_i - z_j|}{c_z}} e^{-\frac{|x_i - x_j|}{c_x}} e^{-\frac{|y_i - y_j|}{c_y}} e^{-\frac{|t_i - t_j|}{c_t}} . \tag{2.13}$$

Thereby z_i, x_i, y_i, and t_i represent the altitude, longitude, latitude, and time coordinates of data point i. The terms c_z, c_x, c_y and c_t are correlation lengths, which usually need to be chosen in an ad-hoc manner. If the data points i and j belong to different retrieval target types, the term should be set to zero.

This regularisation can be analytically inverted as demonstrated in appendix A.5 and delivers a sparse precision matrix $\mathbf{S_a}^{-1}$. However, the strength of this regularisation approach diminishes as more dimensions are included. The regularisation constraint becomes zero as soon as the state vector follows the a priori shape along one dimension, regardless of the state of affairs along the other dimensions. It is however quite practical for retrievals that either do not require strong regularisation in the first place as they are relatively well-posed or require regularisation along only one spatial dimension. This scheme is successfully applied in Chap. 3 on a tomographic 2-D setup. Its main advantage is the ability to directly define the variances in the covariance matrix.

Tikhonov regularisation

Another option for defining the regularisation matrix $\mathbf{S_a}^{-1}$ is to employ Tikhonov regularisation (Tikhonov and Arsenin, 1977), which directly assembles $\mathbf{S_a}^{-1}$. Obviously, this approach allows for an easy setup of $\mathbf{S_a}^{-1}$, but does not give control over $\mathbf{S_a}$, which implies that the variances of $\mathbf{S_a}$ cannot be directly set. Compared to statistical approaches, Tikhonov regularisation allows a more direct influence on the regularisation, for example by imposing only smoothness along specified dimensions on the solution, whereas statistical regularisation always biases the solution towards the a priori vector $\boldsymbol{x}_\mathbf{a}$. If the regularisation strength given by the autoregressive approach defined above proves insufficient, it is advantageous to use Tikhonov regularisation instead (see Chap. 4).

The simplest choice for the Tikhonov regularisation matrix is an identity matrix. In combination with an a priori vector $\boldsymbol{x}_\mathbf{a}$, this selects the solution $\boldsymbol{x}$ with the smallest norm $||\boldsymbol{x}-\boldsymbol{x}_\mathbf{a}||_2$ from all possible solutions. Already Twomey (1977) introduced the use of differential operators as regularisation matrix, which select, for example, the solution with the smallest norm of its first order derivative. Also higher order derivatives may be constrained. Here, a weighted combination of the two approaches is used that is more flexible than either alone.

Four matrices $\mathbf{L_0}$, $\mathbf{L_1^x}$, $\mathbf{L_1^y}$, and $\mathbf{L_1^z} \in \mathbb{R}^{n\times n}$ corresponding to regularisation of the absolute value and the first order derivative in the three dimensions are defined. Then $\mathbf{S_a^{-1}}$ is set to

$$\mathbf{S_a^{-1}} = (\alpha_0)^2 \mathbf{L_0}^\mathrm{T}\mathbf{L_0} + (\alpha_1^x)^2 \mathbf{L_1^x}^\mathrm{T}\mathbf{L_1^x} + (\alpha_1^y)^2 \mathbf{L_1^y}^\mathrm{T}\mathbf{L_1^y} + (\alpha_1^z)^2 \mathbf{L_1^z}^\mathrm{T}\mathbf{L_1^z} \tag{2.14}$$

with the tuning parameters α_0, α_1^x, α_1^y, and $\alpha_1^z \in \mathbb{R}$. It is straightforward to extend this approach to include time as a fourth dimension.

The matrix $\mathbf{L_0}$ is a diagonal matrix. Two sensible choices for this matrix are the identity matrix or the reciprocal value of the corresponding standard deviations. The $\mathbf{L_1}$ matrices are simple Tikhonov regularisation matrices of first order, adjusted for the non-uniform grid size (see appendix A.4 for a detailed discussion). For a 1-D single target retrieval with uniform grid size h, the $\mathbf{L_1}$ matrix would be defined as

$$\mathbf{L_1} = \frac{1}{h}\begin{pmatrix} -1 & 1 & 0 & \dots & 0 \\ 0 & -1 & 1 & \ddots & \vdots \\ \vdots & \ddots & \ddots & \ddots & 0 \\ 0 & \dots & 0 & -1 & 1 \\ 0 & \dots & 0 & 0 & 0 \end{pmatrix}. \tag{2.15}$$

This $\mathbf{L_1}$ matrix maps the state vector $\boldsymbol{x}$ onto (a numerical approximation of) its first order derivative with respect to altitude. Thus the value of the constraint becomes the larger the rougher $\boldsymbol{x}$ is. This enforces a rather smooth solution, which is usually expected due to the inherently smooth nature of the atmosphere due to diffusion.

The matrix $\mathbf{S}_\mathbf{a}^{-1}$ becomes singular if α_0 is set to zero, so the Hessian of the cost function J may also become singular, implying that the Gauss-Newton iteration defined in Eq. (2.10) poses a non-invertible linear equation system. Using a Levenberg-Marquardt iteration scheme instead ensures convergence (see Sect. 2.3.2; with proper parameter choice, the scheme presented in appendix A.8 should be applicable, too).

Together, the matrices penalise deviations of the retrieved profile from the a priori profile and of the three partial derivatives of the retrieved profile $\boldsymbol{x}$ in the direction of the three spatial dimensions from the corresponding partial derivative of the a priori profile $\boldsymbol{x}_\mathbf{a}$.

2.3.2. Minimisers

The minimisation of the cost function J defined in Eq. (2.8) is the numerically most complex part of the retrieval process. Large-scale problems require a tailored linear algebra and an optimised implementation to become solvable. This section briefly presents the most suitable minimisation algorithms for tomographic problems, focusing on those used for the retrievals in the following chapters of this thesis.

Steepest descent-type methods

The previously presented iteration formulas require both the gradient $\boldsymbol{J}'$ and the Hessian $\mathbf{J}''$ of the cost function J (or approximations thereof). This usually requires the full evaluation of the Jacobian matrix of $\boldsymbol{F}$, which can be quite costly to evaluate (see Sect. 2.2.5). Steepest descent-type methods require only the gradient $\boldsymbol{J}'$ of J:

$$\boldsymbol{x}_{i+i} = \boldsymbol{x}_i - \lambda_i \boldsymbol{J}'(\boldsymbol{x}_i). \tag{2.16}$$

The λ_i parameter needs to be defined in each iteration, for example by using line search methods (Nocedal and Wright, 2006, p. 21ff). More sophisticated variants of this method employ the gradient $\boldsymbol{J}'$ to construct an approximation of the Hessian $\mathbf{J}''$ (e.g. Nocedal, 1980). Such algorithms are widely used in data assimilation systems, where a very good initial guess for the following day is given by projection from the last day and requirements on convergence speed can therefore be relaxed (e.g. Elbern and Schmidt, 1999).

Employing algorithmic differentiation, the gradient $\boldsymbol{J}'$ of J can be calculated with computational cost in the order of a single evaluation of J. However, the convergence speed of such methods is usually much slower than that of Newton-type methods. For the types of problem discussed in this work, Lotz (2010) finds that steepest descent-type methods are not competitive with Newton-type methods.

Gauss-Newton

The Gauss-Newton iteration was already presented in Eqs. (2.10) and (2.11). It is a Newton-type method using the first order derivative of the forward model.

In general, Gauss-Newton does not ensure a reduction of the cost function in each iteration and therefore also not the convergence to a minimum. To be of practical use, it is coupled with a line-search algorithm (Nocedal and Wright, 2006, p. 254ff.). A line-search algorithm takes a search direction (in this case the correction step supplied by the Gauss-Newton method) and tries to find a value of J that results in a reduction of the current value of the cost function along the straight line defined by that vector. As the Newton direction is a descent direction, this guarantees that the cost function is reduced in each iteration until a minimum is reached. A very simple line-search algorithm tries first the value pointed to by the correction step. If this value does not result in a reduction of the cost function, the correction step is successively reduced in size until a reduction of the cost function is achieved. This naturally requires an evaluation of the cost function J in each step, thereby increasing the overall execution time. Therefore, JURASSIC2 implements a slightly more complicated, but also more efficient algorithm to determine the next step-length (see Press et al., 2007, p.478ff).

Levenberg-Marquardt

The Levenberg-Marquardt algorithm is the workhorse of non-linear minimisation. It is a modification of the Gauss-Newton method that adds a positive definite matrix to the approximation of the Hessian, which ensures that the linear equation system is not rank-deficient and reasonably well conditioned:

$$\begin{aligned}\boldsymbol{x}_{i+1} = \boldsymbol{x}_i - \left(\mathbf{S}_\mathbf{a}^{-1} + \mathbf{F}'(\boldsymbol{x}_i)^\mathrm{T}\mathbf{S}_\epsilon^{-1}\mathbf{F}'(\boldsymbol{x}_i) + \lambda_i \mathbf{I}_\mathbf{n}\right)^{-1} \cdot \\ \left(\mathbf{S}_\mathbf{a}^{-1}(\boldsymbol{x}_i - \boldsymbol{x}_\mathrm{a}) + \mathbf{F}'(\boldsymbol{x}_i)^\mathrm{T}\mathbf{S}_\epsilon^{-1}\left(\boldsymbol{F}(\boldsymbol{x}_i) - \boldsymbol{y}\right)\right) \qquad (2.17)\end{aligned}$$

This algorithm has been used by Carlotti et al. (2006) for tomographic evaluation, albeit without the use of iterative solvers for the linear equation systems as described below. Unfortunately, the Levenberg-Marquardt algorithm cannot be applied on Eq. (2.11), which necessitates the use of Gauss-Newton for that formulation of the problem.

In effect, the Levenberg-Marquardt algorithm applies a Tikhonov regularisation to the inversion of the Hessian. JURASSIC2 implements a simple heuristic for the choice of the parameter λ_i following Marquardt (1963): An initial value for λ_0 needs to be set heuristically. If the cost function J was decreased in value by the iteration step, λ_{i+1} is set to $\lambda_i/10$. If the value of the cost function did not decrease, the current λ_i is successively multiplied by 10 until the cost function can be reduced. Compared to more recent methods for choice of λ_i (e.g. Nocedal and Wright, 2006, p. 260ff), this is a very simple heuristic, but it is sufficient for the examined problems.

If the vector $\boldsymbol{x}$ contains elements of varying size, the term $\lambda_i\mathbf{I_n}$ should be replaced by a scaling matrix. If optimal estimation is used for regularisation, the matrix $\mathbf{S_a^{-1}}$ can be directly used for that purpose, implying that $\lambda_i\mathbf{S_a^{-1}}$ can be used instead of $\lambda_i\mathbf{I_n}$.

The convergence and the behaviour of the algorithm can be analysed and proven in different ways (e.g. Nocedal and Wright, 2006, p. 260ff). The basic idea behind the modification is to have a weighted mean between a Newton step ($\lambda_i \mapsto 0$) and a steepest descent step ($\lambda_i \mapsto \infty$). The steepest descent method is known to always converge to a minimum, albeit very slowly, whereas the Newton method converges quickly, but only in the vicinity of the minimum. Far away from the minimum, the Levenberg-Marquardt scheme behaves similar to a steepest descent method while its convergence speed improves when $\boldsymbol{x}_i$ gets closer to a minimum.

In spite of seemingly modifying the cost function by an additional regularisation term, the Levenberg-Marquardt method still converges to a minimum of J, if one allows the parameter λ_i to decrease sufficiently.

Newton-Kacmarcz

The linear equation systems posed by the Gauss-Newton and Levenberg-Marquardt algorithms become problematic to handle due to the sheer size of the tomographic problems. One approach to make these sub-problems easier is to replace a single, large equation system by a number of smaller ones. If the set of measurements can be split into groups, which are not correlated with one another, the measurement covariance matrix $\mathbf{S}_\epsilon$ is diagonal or block-diagonal and each such group of measurements can be treated separately.

The Newton-Kacmarcz algorithm (Burger and Kaltenbacher, 2006), which is also called algebraic reconstruction technique (ART) or sequential updating (Rodgers, 2000, p. 97f)[1], splits each iteration of the Gauss-Newton algorithm into a sequence of updates to the atmospheric state. Effectively, it modifies Eq. (2.11) by using the Kaczmarz (1937) algorithm for solving the linear equation system. This method was successfully used by Steck et al. (2005) for 2-D tomographic evaluation of MIPAS data.

The measurements are split into q, $1 < q \leq m$, groups of measurements $\boldsymbol{y}^j$, $1 \leq j \leq q$, so that no measurement of one group is correlated with any measurement of any other group. This implies that $\mathbf{S}_\epsilon$ can be split without loss of information into q matrices $\mathbf{S}_\epsilon^j$ and also $\boldsymbol{F}$ is split into q sub-functions $\boldsymbol{F}^j$. Each single iteration step of Eq. (2.11) is sub-divided into q steps. The vector $\boldsymbol{x}_{i+1}^0$ is initialised with $\boldsymbol{x}_\mathbf{a}$ and $\mathbf{S}^0$ with $\mathbf{S}_\mathbf{a}$. The first linearisation point $\boldsymbol{x}_0$ may be initialised with $\boldsymbol{x}_\mathbf{a}$ or any other initial guess. A single "inner" iteration is then defined by:

$$\begin{aligned}\boldsymbol{x}_{i+1}^j &= \boldsymbol{x}_{i+1}^{j-1} + \mathbf{S}^{j-1}\mathbf{F}_j'(\boldsymbol{x}_i)^\mathrm{T}\left(\mathbf{F}_j'(\boldsymbol{x}_i)\mathbf{S}^j\mathbf{F}'{}_j(\boldsymbol{x}_i)^\mathrm{T} + \mathbf{S}_\epsilon^j\right)^{-1} \qquad (2.18)\\ &\quad\cdot\left(\boldsymbol{y}_j - \boldsymbol{F}_j(\boldsymbol{x}_i) - \mathbf{F}_j'(\boldsymbol{x}_i)(\boldsymbol{x}_i - \boldsymbol{x}_{i+1}^{j-1})\right)\\ \mathbf{S}^j &= \mathbf{S}^{j-1} - \mathbf{S}^{j-1}\mathbf{F}_j'(\boldsymbol{x}_i)^\mathrm{T}\left(\mathbf{F}_j'(\boldsymbol{x}_i)\mathbf{S}^{j-1}\mathbf{F}_j'(\boldsymbol{x}_i)^\mathrm{T} + \mathbf{S}_\epsilon^j\right)^{-1} \qquad (2.19)\\ &\quad\cdot\mathbf{F}_j'(\boldsymbol{x}_i)^\mathrm{T}\mathbf{S}^{j-1}.\end{aligned}$$

The new "outer" location $\boldsymbol{x}_{i+1}$ is then defined by $\boldsymbol{x}_{i+1}^q$. The linear equation systems that need to be solved for this method are much smaller, ideally being reduced to a single line requiring only a single division to be solved. However, as $\mathbf{S}^j$ are dense matrices that need to be stored and updated, the memory consumption of this method is substantial. Also, while solving each individual equation system may be inexpensive, the combined constructions of the equation systems are not. While the setup is distributed on q different matrices, the construction effort is essentially identical with that of Eq. (2.11) (i.e. requiring mn^2 multiplications for constructing the q matrices). In Sect. 2.3.3, it is demonstrated that the construction of the equation system determines the order of the overall cost.

---

[1] Both the original printing and the 2008 revision of (Rodgers, 2000) contain errors in this section. Please refer to the erratas for a correct description.

This approach reduces the computational effort only slightly, even not taking into account the additional effort for the maintenance of $\mathbf{S}^j$. As this method requires the use of the covariance matrices, it cannot easily take advantage of the sparsity of the corresponding precision matrices. Summarising, it is only a marginal improvement over a pure Gauss-Newton approach and not very well suited for 3-D tomography.

LSQR

The LSQR algorithm[2] is an iterative method introduced by Paige and Saunders (1982). It can be used as alternative method for the minimisation of the cost function J, which is then mathematically equivalent to Eq. (2.10). However, it is based on Eq. (2.12) and therefore requires the matrices $\mathbf{S}_{\mathbf{a}}^{-1/2}$ and $\mathbf{S}_{\epsilon}^{-1/2}$. The LSQR algorithm is supposed to be more stable for ill-conditioned problems (Nolet, 1985). According to Geppert (2010), it is equivalent in stability and computationally slightly more costly than using Levenberg-Marquardt combined with an iterative solver (see Sect. 2.3.3) for the types of problem discussed in this thesis. It remains an open topic, whether more ill-conditioned problems profit from this algorithm, for example retrievals from nadir measurements or retrievals forgoing any regularisation constraints (as might be possible for 2-D retrievals from PREMIER infrared limb-sounder data).

2.3.3. Solving linear sub-problems

Finding the solution of large-scale linear equation systems is crucial for all presented Newton-type minimisers. Two fundamentally different methods are available for finding such a solution. On the one hand, one may use decompositions or direct solvers, which deliver an “exact” solution (to machine accuracy). On the other hand, one may use iterative solvers, which deliver an approximate solution. This section proceeds to present the most relevant solvers implemented in JURASSIC2 and demonstrates that only iterative solvers are feasible for large-scale tomographic problems.

Direct solver

A direct solver calculates an exact solution of a linear equation system by means of decomposition. In this context, a decomposition expresses the linear equation

---

[2] Please note that LSQR is no acronym, but indeed the name of the algorithm.

system matrix as the product of two matrices, whereby each of the two new matrices is either orthogonal or triangular. The transformed system allows to calculate a solution of the original equation system in a straightforward way.

For example, take the QR-decomposition, where **Q** is an orthogonal matrix and **R** is an upper-triangular matrix. Given a linear equation system

$$\mathbf{A}\boldsymbol{x} = \boldsymbol{y}, \tag{2.20}$$

the QR-decomposition allows replacing **A** with the matrix product **QR**. Following a multiplication with the inverse $\mathbf{Q}^{\mathrm{T}}$ of **Q**, the system presents itself as

$$\mathbf{R}\boldsymbol{x} = \mathbf{Q}^{\mathrm{T}}\boldsymbol{y}. \tag{2.21}$$

As **R** is a triangular matrix, Eq. (2.21) can be easily solved for $\boldsymbol{x}$.

For relatively small problems, i.e. 1-D problems, an exact solution for the linear equation system can be calculated using such methods. This requires first completely calculating the equation system matrix, which usually involves two matrix-matrix products, which together require $2m^2n$ (or $2mn^2$ for Eq. (2.11)) multiplications, followed second by a decomposition.

As the given linear equation systems are usually symmetric positive definite, a Cholesky decomposition into two triangular matrices is the most efficient decomposition, using $n^3/6$ (or $m^3/6$ for Eq. (2.11)) multiplications (Deuflhard and Hohmann, 1993, p. 18). The simulations of Chap. 3 are mostly performed using Eq. (2.11) and a Cholesky decomposition. For slightly larger systems however, the Cholesky decomposition becomes unstable. A QR decomposition could be used instead, which however costs $4n^3/3$ (or $4m^3/3$ for Eq. (2.11)) operations (Deuflhard and Hohmann, 1993, p. 81) and quickly becomes the determining factor for execution time. Once the decomposition is given, solving a single linear equation system with it becomes a computationally negligible matter.

Figure 2.6 compares the required number of multiplications for the various methods and three example problems (corresponding roughly to single-target 1-D, 2-D, and 3-D problems). It is evident that just preparing the matrix to be decomposed is a very costly task and usually more costly than the decomposition itself. However, it is still more efficient to choose the iteration formula according to the respective sizes of n and m.

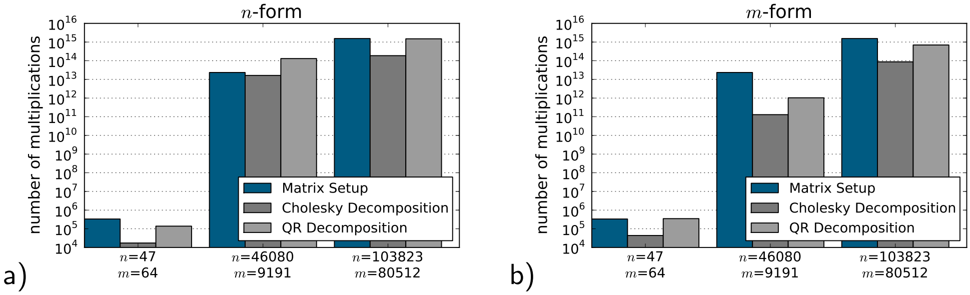

Figure 2.6: The computational effort for creating and decomposing the linear equation system matrix. Panel **(a)** depicts the number of multiplications for setting up the system matrix for Eq. (2.10) and solving the system using decompositions. Panel **(b)** shows the same numbers for Eq. (2.11). Please note the logarithmic scale.

Iterative solver

An iterative solver calculates an approximate solution of a linear equation system by means of an iterative formula. The conjugate gradient scheme is the standard iterative method to solve a symmetric positive definite equation system (e.g. Nocedal and Wright, 2006, p. 101f). It is a widely used iterative method, which requires at most n iterations to exactly solve an $n \times n$ equation system using arbitrary precision; using floating point numbers, more iterations may be required for a precise solution. However, in most cases an approximate solution generated in much less iterations is sufficient.

The conjugate gradient scheme is very attractive for large-scale problems as it requires only the ability to multiply the equation system matrix with a vector in contrast to decompositions, which require the full matrix to be accessible. An informal description of the conjugate gradient algorithm is given for convenience in appendix A.7 and demonstrates that only the matrix-vector product is required. This removes the need to assemble the equation system matrix via costly matrix-matrix products. The iteration formula in Eq. (2.10) has the additional advantage that all involved matrices are sparse matrices, which are very inexpensive to multiply with vectors, further reducing computational cost. Therefore, implementing the matrices using dedicated data structures significantly reduces both memory consumption and computation time.

The linear equation system in each Gauss-Newton step is defined by the matrix $\mathbf{M} \in \mathbb{R}^{n \times n}$:

$$\mathbf{M} = \left(\mathbf{S}_{\mathbf{a}}^{-1} + \mathbf{F}'(\boldsymbol{x}_i)^{\mathrm{T}} \mathbf{S}_{\epsilon}^{-1} \mathbf{F}'(\boldsymbol{x}_i) \right) . \qquad (2.22)$$

The matrix $\mathbf{S}_\epsilon^{-1}$ is positive semi-definite and thereby $\mathbf{F}'(\boldsymbol{x}_i)^\mathrm{T}\mathbf{S}_\epsilon^{-1}\mathbf{F}'(\boldsymbol{x}_i)$ is also positive semi-definite. So, if $\mathbf{S}_\mathbf{a}^{-1}$ is of full rank, the matrix $\mathbf{M}$ is symmetric positive definite, enabling the use of the iterative conjugate gradient scheme. Otherwise, using Levenberg-Marquardt instead of pure Gauss-Newton solves this problem, as the added regularisation term brings $\mathbf{M}$ to full rank. This adds another matrix to $\mathbf{M}$, which can be treated just as $\mathbf{S}_\mathbf{a}^{-1}$ in the following.

The matrix $\mathbf{M}$ is generally dense, even though it is composed of the product of sparse matrices. The product $\mathbf{F}'(\boldsymbol{x}_i)^\mathrm{T}\mathbf{S}_\epsilon^{-1}\mathbf{F}'(\boldsymbol{x}_i)$ is rather costly to evaluate and generates a dense matrix, with a large memory foot print. Gladly, the conjugate gradient algorithm does not require the matrix $\mathbf{M}$, but only the result of products of $\mathbf{M}$ with given vectors. This product can be cheaply provided by four matrix-vector products: first, the given vector is multiplied with $\mathbf{F}'(\boldsymbol{x}_i)$, then the result of this product is multiplied with $\mathbf{S}_\epsilon^{-1}$, and so on. So the matrix-vector product between the linear equation system matrix and an arbitrary vector can be provided without calculating the system:

$$\mathbf{M}\boldsymbol{x} = \mathbf{S}_\mathbf{a}^{-1} \cdot \boldsymbol{x} + \mathbf{F}'(\boldsymbol{x}_i)^\mathrm{T} \cdot \left(\mathbf{S}_\epsilon^{-1} \cdot \left(\mathbf{F}'(\boldsymbol{x}_i) \cdot \boldsymbol{x}\right)\right). \tag{2.23}$$

In this way, the conjugate gradient algorithm avoids the costly matrix-matrix products and requires nearly no memory beyond that required for the storage of the (sparse) original matrices. Further, executing the product $\mathbf{M}\boldsymbol{x}$ as a series of sparse matrix-vector products is actually more efficient than the product between the dense matrix $\mathbf{M}$ and $\boldsymbol{x}$.

An alternate way of calculating $\mathbf{M}\boldsymbol{x}$ is the application of algorithmic differentiation. This offers a way to calculate the product between the Hessian of a function (remember that $\mathbf{M}$ corresponds to the Hessian $\mathbf{J}''$ plus an optional term for the Levenberg-Marquardt algorithm) and a vector without the creation of the Hessian itself (Lotz, 2010).

Being an iterative method, the conjugate gradient scheme requires a certain number of iterations to approximate the solution to a desired degree. The conjugate gradient method converges only slowly for 3-D tomographic setups, especially for multi-target setups involving targets of different magnitudes. Its convergence speed directly depends on the condition number of $\mathbf{M}$, which is the quotient of the largest and smallest eigenvalue. Typically, one tries to improve upon the convergence speed by transforming the original problem to a better conditioned one. Instead of the equation system $\mathbf{M}\boldsymbol{x} = \boldsymbol{b}$, the equivalent equation system $\mathbf{C}^\mathrm{T}\mathbf{M}\mathbf{C}\hat{\boldsymbol{x}} = \mathbf{C}^\mathrm{T}\boldsymbol{b}$ with $\boldsymbol{x} = \mathbf{C}\hat{\boldsymbol{x}}$ is solved, whereby $\mathbf{C}$ is an invertible matrix. This technique is called preconditioning (e.g. Saad, 2003). Thereby, the conjugate gradient scheme actually requires the matrix-vector product of $\mathbf{C}^{\mathrm{T}}\mathbf{C}$ with arbitrary vectors instead of the matrix $\mathbf{C}$ itself. The best choice for $\mathbf{C}$ would obviously be $\mathbf{M}^{-1/2}$, which would require only a single iteration in the conjugate gradient scheme. However, calculating a root of $\mathbf{M}$ is impractical, so more inexpensive transformations are employed.

Most preconditioners require full knowledge of the matrix $\mathbf{M}$. A simple exception from this rule is the Jacobi preconditioning. The Jacobi preconditioner consists of just the inverse of the diagonal of $\mathbf{M}$: $\mathbf{C} = \mathrm{diag}(\mathbf{M})^{-1/2}$. This diagonal matrix can be calculated using about $2mn$ multiplications, if $\mathbf{S}_{\epsilon}^{-1}$ is a diagonal matrix. If the non-diagonal elements of $\mathbf{S}_{\epsilon}^{-1}$ are not zero and cannot be neglected, this preconditioning requires an additional multiplication of the Jacobian matrix with $\mathbf{S}_{\epsilon}^{-1}$, which sums up to $m^2n + mn$ multiplications neglecting the sparsity of the involved matrices. This preconditioner has the additional advantage that it automatically scales the problem according to the sensitivity of the cost function with respect to perturbations of different elements of $\boldsymbol{x}$ (Nocedal and Wright, 2006, p. 95f).

The conjugate gradient scheme generally employs a convergence criterion to determine if the current iteration provides a sufficient approximation to the (exact) solution. Typical choices are the reduction of the norm of the residuum, for instance $||\mathbf{M}\boldsymbol{x} - \boldsymbol{b}||_2$, below a certain threshold or a relative reduction thereof, for instance $||\mathbf{M}\boldsymbol{x} - \boldsymbol{b}||_2 / ||\boldsymbol{b}||_2$. For the simulations presented in this work, the relative reduction of the residuum is used. The Gauss-Newton scheme converges faster, if for the first iterations only a small reduction of the residuum is required and the convergence criterion is tightened as the Gauss-Newton scheme converges upon the solution. In addition to the outer Gauss-Newton iteration converging faster, this also decreases the number of inner iterations used in the conjugate gradient scheme (see appendix A.8).

Execution time

Using direct solvers is prohibitively expensive for tomographic problems. For a square linear equation system with n unknowns, the Cholesky decomposition requires in the order of n^3 multiplications. The conjugate gradient scheme uses n^2 multiplications per iteration (for the matrix-vector product). Using arbitrary precision arithmetics, it converges in at most n iterations, which sums about to also about n^3 overall multiplications. The advantage of the conjugate gradient method is based on the smart implementation of the involved matrix-vector products as well as requiring usually much less than n iterations. Also the im-

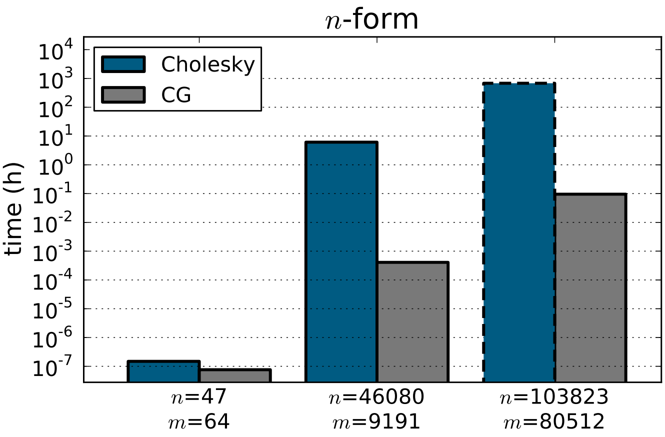

Figure 2.7: The required wall-clock time to solve a linear equation system for different problem sizes including the time for setting up the system matrix for the Cholesky decomposition. The bars indicate the time to solve a single equation system as required for one iteration step of Eq. (2.10). Please note that the dashed bar has been estimated, as it could not be measured due to the decomposition becoming numerically unstable.

plementation of the involved linear algebra plays a big role in what algorithm is faster in the end, as dense matrix-vector products can be extremely optimised taking the hardware architecture into account (e.g. Whaley et al., 2001). In the end, one has to compare the execution time of examples using available implementations for each algorithm.

Figure 2.7 compares the execution time for the Cholesky decomposition and the conjugate gradient method. The conjugate gradient method is configured to terminate after the norm of the residuum has been reduced by a factor of 10 000, which is sufficient for an iteration step in the Gauss-Newton scheme. The three problems are typical for single target 1-D, 2-D, and 3-D retrievals. The conjugate gradient method delivers the solution significantly faster (minutes instead of days for the largest examined problems), even in the 1-D case, where the matrices are not as sparse as for the larger problems. Further, the employed Cholesky decomposition implementation even becomes numerically unstable for large-scale problems.

The conjugate gradient scheme is much more efficient for the presented tomographic problems and can also handle small-scale problems efficiently.

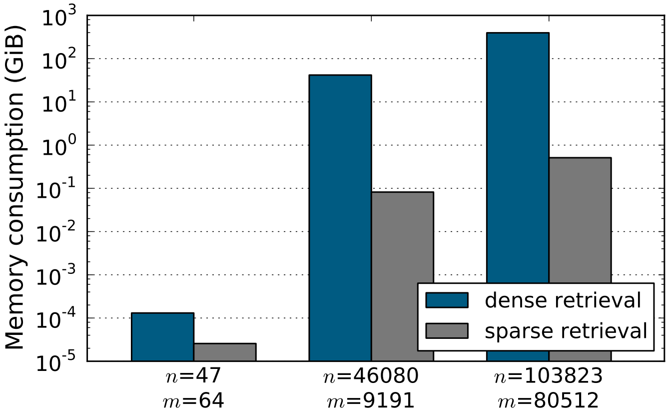

Figure 2.8: The memory consumption for different retrieval setups and dense or sparse inversion schemes. The memory for dense retrievals includes all necessary temporary matrices for deriving diagnostic information (see Sect. 2.4).

Memory efficient calculation

The memory consumption of the employed algorithm is one of the limiting factors determining the treatable problem size. The matrices involved in the retrieval are usually of the sizes $n \times n$, $n \times m$ and $m \times m$. As n and m are usually of comparable size, one can roughly generalise that the memory requirements increase with the second power of the number of unknowns n. Using a naive implementation and a computer with 256 GiB of main memory, this poses an absolute upper limit for the problem size at around 200 000 unknowns, as a single $n \times n$ matrix in double precision would consume the full memory. In practice, more than a single matrix needs to be stored, reducing the maximum problem size even further. While one can use other storage options like the hard drive to compensate, the typical increase in runtime makes this option very undesirable.

The best way to proceed is to exploit the sparsity of the involved matrices. A sparse representation of a matrix stores only the non-zero entries together with administrative information where those non-zero entries are located. Typically such a representation requires storage for one floating point number and one to two indices per non-zero entry. Figure 2.8 depicts the memory savings gained by using sparse representations for three example setups. The middle 2-D setup can still be retrieved using a dense scheme on common hardware, however increasing the problem size towards 3-D problems on the right, this option becomes infeasible.

Using sparse matrices, computable problem sizes are drastically increased while at the same the involved computation is significantly reduced. For 2-D and 3-D problems the memory consumption is reduced by more than two orders of magnitude. Memory-wise, using sparse representations is just as or even more efficient even for small 1-D problems, which enables the use of a single retrieval implementation for all types of retrievals.

2.4. Diagnostics

The result of any retrieval is meaningless without diagnostic information about the quality of the reconstruction. The minimisers described above only reduce the cost function and thereby provide a solution of the inverse problem. How well this result approximates the true state of the atmosphere is however a different matter. Rodgers (2000) introduced a set of linear diagnostics that can be used to characterise the retrieval result. The diagnostics of tomographic retrievals are however still problematic as the problem size prevents the calculation of diagnostic quantities for all retrieved data points. In this section, first, the most important diagnostic quantities are described, and second, their calculation for large-scale retrievals is discussed.

The retrieval diagnostics in this work follow largely Rodgers (2000) and are therefore only briefly discussed. Calculating the diagnostics involves the calculation of the gain matrix $\mathbf{G} \in \mathbb{R}^{n\times m}$ that maps differences of measurements onto differences in the retrieval result and the averaging kernel matrix $\mathbf{A} \in \mathbb{R}^{n\times n}$ that describes the influence of the true atmospheric state on the retrieval result. With $\boldsymbol{x}_\mathbf{f} \in \mathbb{R}^n$ being the retrieval result, the gain matrix $\mathbf{G}$ is defined as

$$\mathbf{G} = \left(\mathbf{S}_\mathbf{a}^{-1} + \mathbf{F}'(\boldsymbol{x}_\mathbf{f})^\mathrm{T}\mathbf{S}_\epsilon^{-1}\mathbf{F}'(\boldsymbol{x}_\mathbf{f})\right)^{-1} \mathbf{F}'(\boldsymbol{x}_\mathbf{f})^\mathrm{T}\mathbf{S}_\epsilon^{-1}, \tag{2.24}$$

and the averaging kernel matrix $\mathbf{A}$ (also called resolution matrix in the field of seismology) is defined as

$$\mathbf{A} = \mathbf{G}\mathbf{F}'(\boldsymbol{x}_\mathbf{f}) = \left(\mathbf{S}_\mathbf{a}^{-1} + \mathbf{F}'(\boldsymbol{x}_\mathbf{f})^\mathrm{T}\mathbf{S}_\epsilon^{-1}\mathbf{F}'(\boldsymbol{x}_\mathbf{f})\right)^{-1} \mathbf{F}'(\boldsymbol{x}_\mathbf{f})^\mathrm{T}\mathbf{S}_\epsilon^{-1}\mathbf{F}'(\boldsymbol{x}_\mathbf{f}). \tag{2.25}$$

The gain matrix $\mathbf{G}$ can be interpreted as (regularised) pseudo-inverse of the Jacobian matrix $\mathbf{F}'(\boldsymbol{x}_\mathbf{f})$. The averaging kernel matrix $\mathbf{A}$ being the product of $\mathbf{G}$ with $\mathbf{F}'(\boldsymbol{x}_\mathbf{f})$ should ideally be equal to the identity matrix, but generally isn't due to the employed regularisation and rank deficiency of the Jacobian matrix. Instead, the deviation of $\mathbf{A}$ from the identity matrix gives insight into the smoothing introduced by the regularisation and shows which part of the retrieved atmosphere is reconstructed from measurements and which is taken from a priori information.

Both gain matrix and averaging kernel matrix are fundamental for analysing and understanding the retrieval result as is presented below.

2.4.1. Measurement contribution and resolution

When employing regularisation, it is important to quantify how much the retrieval result is influenced by it. With $\boldsymbol{x}_\mathbf{t} \in \mathbb{R}^n$ being the true (usually unknown) state of the atmosphere, the retrieval result can be expressed by the linear expression

$$\boldsymbol{x}_\mathbf{f} = \mathbf{A}\boldsymbol{x}_\mathbf{t} + (\mathbf{I_n} - \mathbf{A})\boldsymbol{x}_\mathbf{a} + \mathbf{G}\epsilon, \tag{2.26}$$

which gives the basis for the (linearised) diagnostics.

Equation (2.26) gives a good insight into the necessary trade-offs influencing the inversion. On the one hand, $\mathbf{A}$ shall be very close to the identity matrix so that the true state enters the solution unbiased. On the other hand, the error term $\mathbf{G}\epsilon$ needs to be kept small, meaning that $\mathbf{G}$ should not have large eigenvalues, which would amplify noise and usually cause the solution to oscillate heavily. A third consideration must be given to the middle term, which describes the influence of the a priori vector $\boldsymbol{x}_\mathbf{a}$. Where possible, this middle term shall be kept minimal. One way of achieving this is to ensure that the rows of $\mathbf{A}$ sum up to one (which is usually feasible by adjusting the regularisation matrix) and choosing a constant a priori vector, which together force $(\mathbf{I_n} - \mathbf{A})\boldsymbol{x}_\mathbf{a}$ to zero. However, in atmosphere physics one frequently only ensures that the rows of $\mathbf{A}$ sum up to one while choosing climatological values as a priori vector, which almost always have a distinct structure and are not constant.

The sum over an averaging kernel matrix row is called the measurement contribution and is regardless of choice of $\boldsymbol{x}_\mathbf{a}$ a good indicator for whether a point of the solution is determined by measurement information (if it is close to “1”) or by a priori information (if it is close to “0”). Please note that a measurement contribution close to “1” is only a necessary condition for an unbiased solution but in itself not sufficient.

Resolution is a second important diagnostic measure, which can also be deduced from the rows of the averaging kernel matrix. Resolution quantifies the amount of smoothing introduced by the retrieval process. There are many ways to characterise the resolution, as Rodgers (2000) discusses in detail for 1-D retrievals or von Clarmann et al. (2009) for 2-D. The simplest figure is the information content, which can be estimated by taking the inverse of the diagonal entries of the averaging kernel matrix **A**. It indicates how much information is contained within a grid element. For example, if the information content would be 0.5, then two elements would share one piece of information and one could, for example, reduce the grid resolution by a factor of two without losing too much information.

For tomographic retrievals, the information content does not describe along which dimensions the information is smoothened in space. Knowing that a certain number of grid points share one piece of information gives no indication about the location of those grid boxes. Thereby, the information content does not allow quantifying for instance if and how much the vertical resolution is better than the horizontal one (as is typical for limb-sounders). This work therefore uses a different measure: the full width at half maximum (FWHM) of the averaging kernel matrix row. For 1-D retrievals, this is simply a matter of identifying the maximum entry of a given row and then identifying (by linear interpolation) the coordinates where the half maximum is reached in both directions. For problems of higher dimension, the row needs first to be reshaped into the 2-D, 3-D or even 4-D volume it describes. Then, for each dimension, an axis is placed along said dimension through the point of the volume belonging to element i (when analysing the ith row). Said axis is then analysed using the FWHM method and delivers a measure for the resolution along said axis. This method works well, if the multi-dimensional shape of the averaging kernel matrix row is roughly ellipsoid with the main axes of the ellipsoid coinciding with the spatial axes, which usually is the case for well resolved data points.

Figure 2.9 shows this process for a 3-D retrieval setup. The resolution of one data point of a 3-D retrieval along the latitude axis shall be computed. To that purpose, those elements of the row are selected and plotted in panel (b) that have the same longitude and altitude values as the retrieved data point. The shape of this averaging kernel matrix row is roughly ellipsoidal and the projection has a distinct maximum. This maximum is shown as solid line, whereas the half-maximum of the row is drawn as dashed line. The elements of the averaging kernel matrix row are linearly interpolated (dotted line) to find the exact position, where the half-maximum line is crossed. The distance between the right and the left crossing is then used as a measure for the resolution along the latitude direction, in this case 53 km.

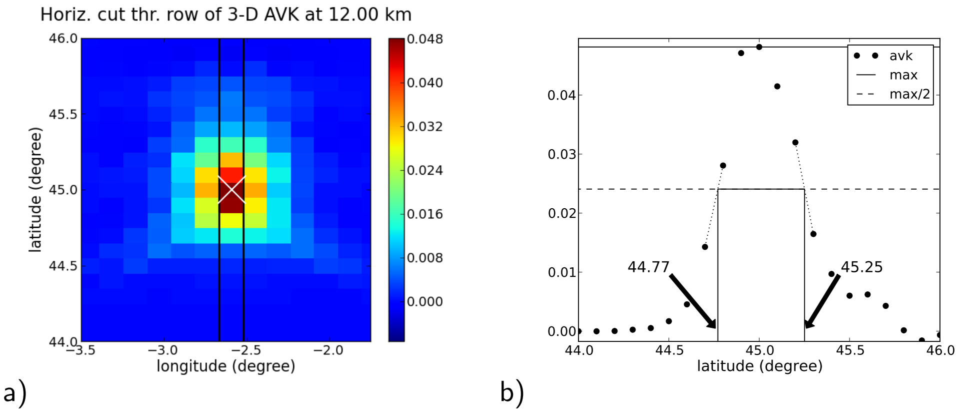

Figure 2.9: The calculation of resolution along different axes. Panel **(a)** depicts part of a 3-D averaging kernel matrix row, where its elements are mapped into a 3-D volume according to the position of the data element of the true atmospheric state that they map onto the retrieved value. Panel **(b)** shows the framed portion of (a) in greater detail.

By combining measurement contribution and resolution, it is possible to determine, which part of the retrieval result is unbiased by a priori information and to quantify the extent of smoothening introduced by the regularisation.

2.4.2. Retrieval noise

The effect of noise on the retrieval can be estimated based on the effect of perturbations of the measurements on the retrieval result.

The method of optimal estimation does not only provide an optimal estimate $\boldsymbol{x}_\mathrm{f}$ but also a corresponding covariance matrix of the estimate. However, as the multi-dimensional a priori covariance matrices for the atmospheric state employed in this work are not derived from a climatology, but chosen ad-hoc, the covariance matrix of the retrieval result $\boldsymbol{x}_\mathrm{f}$ should not be interpreted statistically. Instead, the retrieval noise is used for diagnostic purposes. The effect of measurement noise on the retrieval result can be described as

$$\mathbf{S}_\mathrm{noise} = \mathbf{G}\mathbf{S}_\epsilon\mathbf{G}^\mathrm{T}. \tag{2.27}$$

This allows for the quantification of the effect of retrieval noise on the result. In a similar way the effect of other, also systematic, errors on the retrieval result can be quantified, if an estimate of their covariance matrix is available.

2.4.3. Calculation of diagnostics using conjugate gradients

Calculating the full gain and averaging kernel matrices for large-scale problems is impractical due to the involved matrix inversion and thereby poses a problem for the calculation of diagnostic quantities. As previously discussed, inverting a matrix using a decomposition requires computation time proportional to the third power of n. Using the conjugate gradient algorithm to the same purpose is no help in this case, as it is very efficient for solving a single equation system, but not for a full matrix inversion, which corresponds to computing the solution of n linear equation systems.

While it is therefore not feasible to fully calculate $\mathbf{G}$ and $\mathbf{A}$, it is possible to derive diagnostics for a single entry of $\boldsymbol{x}_\mathbf{f}$ without any matrix inversion as first demonstrated by Nolet (1985). This section applies this approach onto Rodgers' more advanced diagnostics. Calculating the diagnostics of a single point requires only the corresponding row of $\mathbf{G}$ to estimate the noise error (which is generally estimated using the corresponding diagonal element of $\mathbf{S}_\mathrm{noise}$) and the corresponding row of $\mathbf{A}$ to derive measurement contribution and resolution.

To derive a single row of $\mathbf{A}$ and $\mathbf{G}$, only a single row of

$$\mathbf{M}^{-1} = \left(\mathbf{S}_\mathbf{a}^{-1} + \mathbf{F}'(\boldsymbol{x}_\mathbf{f})^\mathrm{T}\mathbf{S}_\epsilon^{-1}\mathbf{F}'(\boldsymbol{x}_\mathbf{f})\right)^{-1}$$

is needed, as this row vector can then be multiplied using vector-matrix multiplications from the left to the right with $\mathbf{F}'(\boldsymbol{x}_\mathbf{f})^\mathrm{T}\mathbf{S}_\epsilon^{-1}$ and $\mathbf{F}'(\boldsymbol{x}_\mathbf{f})^\mathrm{T}\mathbf{S}_\epsilon^{-1}\mathbf{F}'(\boldsymbol{x}_\mathbf{f})$ to derive the rows of $\mathbf{G}$ and $\mathbf{A}$, respectively. With $\mathrm{row}_i(\cdot)$ indicating the i-th row of the supplied matrix, a row of $\mathbf{G}$ can be expressed as

$$\mathrm{row}_i(\mathbf{G}) = \mathrm{row}_i(\mathbf{M}^{-1})\mathbf{F}'(\boldsymbol{x}_\mathbf{f})^\mathrm{T}\mathbf{S}_\epsilon^{-1}, \tag{2.28}$$

$$\mathrm{row}_i(\mathbf{A}) = \mathrm{row}_i(\mathbf{M}^{-1})\mathbf{F}'(\boldsymbol{x}_\mathbf{f})^\mathrm{T}\mathbf{S}_\epsilon^{-1}\mathbf{F}'(\boldsymbol{x}_\mathbf{f}). \tag{2.29}$$

As $\mathbf{M}$ is symmetric, so is $\mathbf{M}^{-1}$. This simplifies the problem, as columns of $\mathbf{M}^{-1}$ can be easily computed using the same iterative linear equation system solver described in Sect. 2.3.3, by using the proper unit vector for the right-hand-side of the linear equation system.

Using this method, it is possible to retrieve diagnostic information for individual points of $\boldsymbol{x}$ without keeping the full matrices $\mathbf{G}$ or $\mathbf{A}$ in memory or even fully generating them. For large-scale retrievals, it is usually too costly to determine the diagnostics for all points of the retrieval as this requires far more computation time than the retrieval itself. But at least for the retrievals presented later on, the diagnostic quantities vary only slowly from point to point, so that one can use Monte-Carlo techniques to randomly sample a subset of $\boldsymbol{x}$ to quickly get a good impression of the overall quality and characteristics of the retrieval and to determine the areas that deserve a closer look.

2.5. Chapter summary

This chapter presented an overview of the mathematics needed to deal with inverse problems in the field of atmospheric remote sensing. Large-scale problems require a different, more efficient treatment than conventional retrievals. Both computation time and memory requirements do not increase proportional with the number of unknowns, but with a higher power. Technically, the retrieval is carried through by the minimisation of a cost function involving a regularisation matrix. Keeping all involved matrices as sparse as possible is important to conserve memory, so two ways of constructing a sparse regularisation precision matrix were given. After presenting a number of different minimisation algorithms typically employed for similar problems, an algorithm consisting of a Gauss-Newton minimiser combined with a conjugate gradient scheme for solving linear equation systems was identified as best available choice. In combination with an implementation exploiting the sparsity of the involved matrices, large 3-D tomographic problems can be solved. Finally, it was shown how diagnostic information can be derived for large-scale retrievals, even though one usually might not be able to derive this information for all elements of the solution.

Can one hear the shape of a drum?

(Marc Kac)

3. Mesoscale gravity wave observations by the PREMIER infrared limb-sounder

This chapter applies the methodology described in the previous chapter onto two-dimensional (2-D) tomographic evaluation of simulated measurements for a proposed satellite experiment called PREMIER (Process Exploration through Measurements of Infrared and millimetre-wave Emitted Radiation; Riese et al., 2005; ESA, 2008; Ungermann et al., 2010a). PREMIER is one of three candidates for ESA's 7th Earth Explorer mission that are currently undergoing feasibility studies. The main mission objective of PREMIER is to quantify processes controlling atmospheric composition in the mid/upper troposphere and lower stratosphere, a region of particular importance for climate change. To achieve this objective, PREMIER will employ the first satellite Fourier transform infrared limb-imager with two 2-D detector arrays combined with a millimetre-wave limb-sounder. It will be able to observe small-scale structures in atmospheric temperatures and trace gas fields with unprecedented 3-D sampling.

The main intent of this chapter is to deduce estimates for how the 3-D sampling of the instrument translates into achievable resolution of the retrieval. A special focus is placed onto which kinds of gravity waves can be resolved by the instrument, since gravity wave detection is one of the main scientific goals of the PREMIER mission.

3.1. Gravity wave observations by the PREMIER infrared limb-sounder

During the PREMIER mission, the infrared limb-sounder (IRLS) can be operated in two different modes. The one discussed in this chapter, the "dynamics mode", is designed for unprecedented 3-D spatial sampling and is thereby optimised to resolve small and mesoscale atmospheric temperature and trace gas structures. This chapter is based upon the technical specification of the PREMIER IRLS as detailed in the assessment report (ESA, 2008). These requirements are currently being re-evaluated and will likely be subject to minor adjustments. The envisioned measurement sampling for the PREMIER IRLS is 0.5 km in the vertical direction, 25 km across track (in a 320 km swath), and 50 km in the along track direction. The across track sampling directly corresponds to the achievable across track resolution because the measurements are nearly independent in this direction. To fully exploit the benefits of the dense sampling in the vertical and along track direction in terms of resolution, a tomographic retrieval scheme is employed. By using a very fast and efficient forward model (see Sect. 2.2), smallest spatial scales may be explored that were not accessed by previous studies (e.g. Carlotti et al., 2006; Steck et al., 2005). In particular, this chapter demonstrates the capability of the PREMIER IRLS to provide unique global information on mesoscale gravity waves (GWs).

Global observations of GWs are a major objective of the PREMIER mission (ESA, 2008). GWs represent an important coupling mechanism for the middle atmosphere (Fritts and Alexander, 2003). They contribute about 50 percent to the driving of the quasi-biennial oscillation (Dunkerton, 1997), are the major forcing mechanism of the summer branch of the Brewer-Dobson circulation (Alexander and Rosenlof, 2003), and contribute 30 to 50 percent to the predicted increase of the Brewer-Dobson circulation due to climate change (McLandress and Shepherd, 2009). GWs are also the main driver of mesospheric winds and cause the cold summer mesopause (McLandress, 1998). Currently, uncertainties in the global representation of GWs and their effects on the circulation represent a major limitation for the predictive capabilities of chemistry climate models.

The great potential of GW observations from space has been demonstrated in several studies (e.g. Fetzer and Gille, 1994; Eckermann and Preusse, 1999; Preusse et al., 2002). However, the spatial resolution of previous global observations was insufficient for the determination of direction-resolved momentum flux (Ern et al., 2004) and so far only absolute values of momentum flux have been deduced from CRISTA (Ern et al., 2004, 2006) and HIRDLS (High Resolution Dynamics Limb Sounder) (Alexander et al., 2008; Wright et al., 2009). In addition, there is a case study of momentum flux from an exceptional long-vertical wavelength mountain wave event over South Georgia Island using AIRS data (Alexander et al., 2009). The combination of high-resolution 3-D temperature measurements and good altitude coverage offered by the PREMIER IRLS will allow for simultaneous determination of GW temperature amplitudes and associated horizontal and vertical wavelength (wave-vector). Preusse et al. (2009) showed that global 3-D observations by limb-imagers such as PREMIER IRLS provide the best perspective to obtain global information of GW momentum flux.

For the interpretation of the results, it is crucial to determine accurately the GW observational filter (Alexander, 1998) of the limb-imaging technique employed by the PREMIER IRLS. The GW observational filter describes the reproduction of GW amplitudes by the retrieval scheme as function of vertical and horizontal wavelength. A precise characterisation of the GW observational filter is also essential for comparisons with other measurement techniques (Preusse et al., 2000; Hertzog et al., 2008) as well as for comparisons with GW resolving models or results obtained from GW parametrisation schemes (Ern et al., 2004, 2005).

3.2. The PREMIER infrared limb-sounder

The PREMIER IRLS essentially combines a Fourier transform infrared spectrometer with two 2-D detector arrays measuring in the spectral regions from 770 to 980 cm^{-1} (band A) and from 1070 to 1650 cm^{-1} (band B), respectively. Each 2-D detector array will consist of about 100 × 100 pixels, providing about 10 000 simultaneous limb-views within the altitude range from ≈3 to 55 km and with a swath width of 320 km. To increase the signal-to-noise ratio, individual array pixels will be co-added to obtain sampling patterns of specific scientific measurement modes. More details can be found in Tab. 3.1.

The radiance of a single measurement typically originates mainly from an air volume with about 500 km extent along the line-of-sight (LOS). The vertical extent is mainly determined by the special viewing geometry of the limb observation and the vertical field-of-view (FOV), which has about 750 m full-width at half-max (FWHM) at the tangent point.

One main advantage of the proposed instrument concept is its great flexibility: the trade-off between spatial and spectral resolution can be adapted to the scientific needs. While currently only two modes are specified, the hardware poses few restrictions if a certain scientific question should require a different trade-off between spatial and spectral sampling. This chapter concentrates on the IRLS “dynamics mode”. It is designed to measure a subset of atmospheric vari-

PREMIER IRLS instrument specification			
Parameter	Unit	Dynamics M.	Chemistry M.
Vert. coverage	km	48 (≈5–53)	
Horiz. coverage (across tr.)	km	240(T)–320(G)	
Vert. sampling	km	≤ 0.5	≤ 2
Horiz. sampling (across tr.)	km	25	80
Horiz. sampling (along tr.)	km	48–50	90–100
Spectral resolution	cm^{-1}	1.25	0.2
Spectral coverage - Band A	cm^{-1}	770–980	
Spectral coverage - Band A	cm^{-1}	1070–1650	
NESR - Band A	$\mathrm{W/(m^2\,sr\,cm^{-1})}$	$\leq 2.2{\cdot}10^{-5}$(T)	$\leq 3.2{\cdot}10^{-5}$(T)
NESR - Band B	$\mathrm{W/(m^2\,sr\,cm^{-1})}$	$\leq 1.4{\cdot}10^{-5}$(T)	$\leq 1.9{\cdot}10^{-5}$(T)

Table 3.1: The principal technical characteristics of the PREMIER IRLS instrument. (T) and (G) denote threshold and goal values, respectively. The goal values for the NESR (noise equivalent spectral radiance) are wavelength dependent. For the spectral samples used in this study the goal value NESR lies at $10^{-5}\,\mathrm{W/(m^2\,sr\,cm^{-1})}$ (ESA, 2008).

ables with very high spatial sampling but moderate spectral sampling. Spectral sampling requirements are relaxed to $1.25\,\mathrm{cm}^{-1}$ from its maximum envisioned sampling of $0.2\,\mathrm{cm}^{-1}$ that is employed in the other major operating mode, the “chemistry mode”. As an example, simulated spectra for the IRLS dynamics mode for cloud-free, mid-latitude atmospheric conditions and 30 km tangent altitude are shown in Fig. 3.1. Even at this reduced spectral resolution, infrared emission features of important atmospheric constituents (e.g. CO_2, H_2O, O_3, HNO_3, F11, CH_4, or N_2O) are clearly visible.

The vertical coverage of the IRLS dynamics mode observations is 48 km with a lower boundary that increases from 3 km at the poles to 7 km at the equator to account for the latitudinal variation of the tropopause height. The vertical measurement sampling is 500 m. Limb images will be measured rearward with respect to the flight direction of the satellite. Dense sampling along track is achieved by a high measurement speed, which requires only about 7.5 s per image in the dynamics mode, corresponding to ≈50 km along track distance. In fact, this represents already an average of multiple measured spectra that reduces both noise and required downlink capacity. The 2-D detector array will allow for 13 parallel measurement tracks. The across track sampling is 25 km and the swath width is 320 km. The three-dimensional measurement grid of the PREMIER IRLS dynamics mode is illustrated in Fig. 3.2. The green spheres represent the tangent points of all measurements of a single image. Each blue

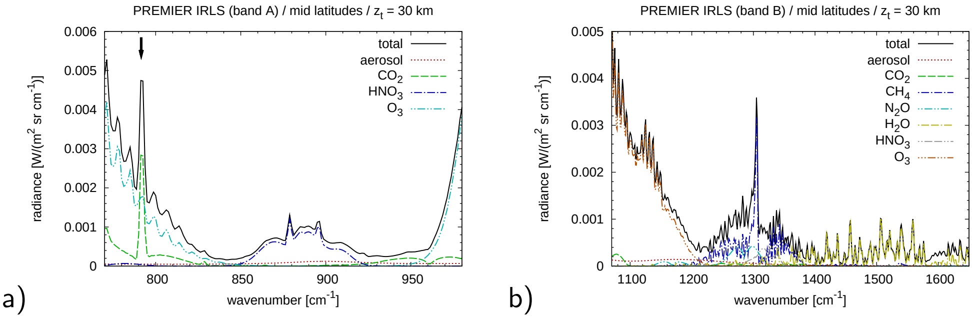

Figure 3.1: Simulated radiance spectra for the PREMIER IRLS band A and B operating in dynamics mode. Calculations are based on mid-latitude atmospheric conditions (Remedios et al., 2007) and 30 km tangent altitude. The black curve indicates total radiance. The other curves indicate radiance for single emitter atmospheres (see legend). The noise level of the observations will be about 10^{-5} W/(m^2 sr cm^{-1}). The black arrow indicates the CO_2 Q-branch analysed in the retrievals. (Figure courtesy of Dr. Lars Hoffmann, Forschungszentrum Jülich).

orb represents a single measurement profile of preceding and following images, providing a visual clue for the horizontal measurement density. Please note that tangent points of a single image are not placed exactly vertically above one another as higher tangent points are located closer to the satellite; in fact, consecutive images are spaced so closely that the topmost tangent points of one image are placed vertically above the lowermost tangent points of the preceding image.

In this chapter, the achievable resolution of the dynamics mode shall be determined with a focus on resolving GWs. The across track resolution directly corresponds to the across track sampling because the LOSs of the different measurement tracks overlap only negligibly. Thus, it suffices to examine a single track and to determine its resolution in vertical and along track direction. Further, it is examined how well monochromatic GWs can be reproduced by PREMIER IRLS measurements and tomographic retrieval techniques in accordance with one of the major scientific mission objectives.

3.3. Simulation setup

In this chapter, it is examined how well tomographic temperature retrievals using simulated PREMIER IRLS dynamics mode measurements are able to reproduce GW parameters like amplitude, horizontal and vertical wavelength, as well

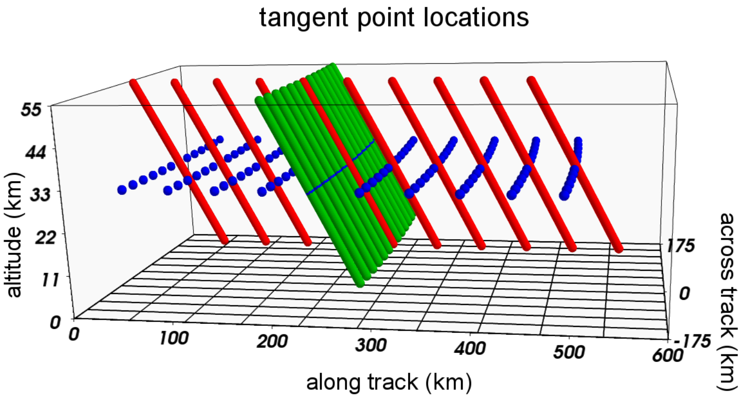

Figure 3.2: Illustration of the PREMIER IRLS dynamics mode measurement grid. Symbols indicate the locations of tangent points of individual measurements. The green coloured spheres represent the measurements of a single image of PREMIER IRLS. Each blue orb represents a full profile and thereby the horizontal component of the measurement grid of ten consecutive images. In the simulations, only measurements of the central track are used, of which ten consecutive vertical measurement profiles are shown coloured in red. As the tangent points of a single profile are spaced at vertical intervals of 500 m, the orbs representing it are merged into a vertical line. For the outermost measurement tracks, the tangent-points lie generally not within the idealised 2-D measurement track, but are displaced from it by up to 2.2 km in the across track direction.

as phase shifts. To this end, linear and non-linear retrieval end-to-end tests are carried out. First, radiance observations are simulated, as the PREMIER IRLS would provide for a given monochromatic GW field. Second, these simulated observations are used as input data for tomographic temperature retrievals. Finally, retrieved temperatures are compared with the original field. No noise or other instrument effects are added to the simulated measurements in order to not obscure the principal capabilities of the approach; however, error estimates for retrieval noise are provided. Please note that this setup is highly simplified compared to what an inversion scheme for actual PREMIER IRLS measurements would look like. In practice, additional values like pressure, contaminant trace gases, etc. would need to be retrieved in addition to temperature.

The set of simulated measurements is designed according to the PREMIER specification as described in Sect. 3.2. For the analysis of the GW observational filter, only limb profiles of the central track of the 2-D array are employed (depicted as red orbs in Fig. 3.2). In total 101 consecutive profiles along track with 91 altitude steps each are used per simulation. The tangent point altitudes of

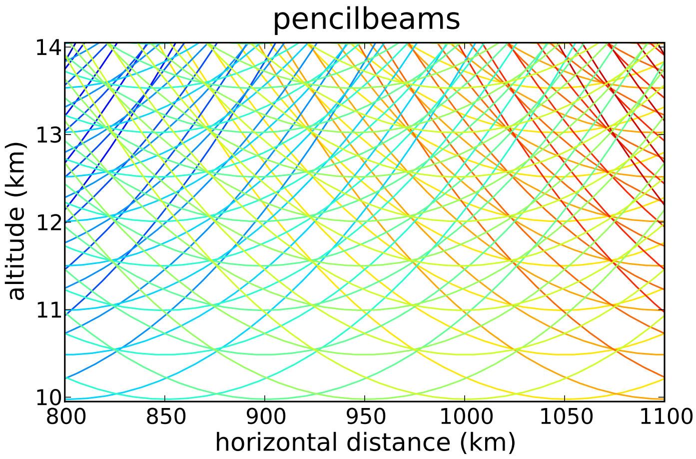

Figure 3.3: LOS of the central measurement track in the PREMIER IRLS dynamics mode. LOS belonging to the same image are assigned the same colour. Note that the plot shows only a minor subset of the full simulated atmospheric slice of 6 000 km times 80 km.

one such profile range from 10 to 55 km spaced at intervals of ≈500 m. This is a simplification of the vertical range of the PREMIER IRLS, which covers 48 km but varies in height between the equator and the poles. Figure 3.3 demonstrates how the LOSs of these dense measurements overlap one another in the along track direction. The same air volume is viewed from multiple angles, which suggests a tomographic retrieval approach.

It is assumed that a single measurement will have a vertical FOV of ≈750 m at the location of the tangent point. This is simulated by convolving the results of the finely spaced pencilbeam calculations with a sensitivity function describing the FOV of the instrument. The sensitivity function is assumed to be a Gaussian with a FWHM of 750 m. A pencilbeam sampling twice as dense as the original measurement spacing was found to be sufficiently accurate, which means that the tangent points of the pencilbeams are vertically spaced at intervals of ≈250 m. Including pencilbeams added above and below the uppermost and lowermost measurement, this sums up to 193 pencilbeams for a single vertical measurement profile of the PREMIER IRLS consisting of 91 measurements.

To accurately represent a wide spectrum of GWs with different horizontal and vertical wavelength, a cross-section of the atmosphere 6 000 km long and 82 km high is defined. This accommodates the full LOS of 91 consecutive vertical measurement profiles of the central track constituting the measurement grid. For the initial calculation of simulated satellite measurements, this cross-section is finely gridded with a horizontal atmosphere grid spacing of only 5 km and a vertical atmosphere grid spacing of 50 m. This shall keep the representation error minimal that is introduced by representing a continuous wave structure by sampling it on a discrete rectilinear grid with linear interpolation. For the retrieval of the baseline setup, a coarser grid is used: the vertical sampling of the atmospheric retrieval grid corresponds to the measurement grid, which is 500 m between 10 km and 55 km height and 2 km outside this range. The horizontal retrieval grid spacing is set to 12.5 km (four times finer than the measurement grid) to avoid representation errors (see Sect. 3.5.2).

For tracks other than the central one, the tangent points of consecutive vertical measurement profiles do not span a plane that is orthogonal to the surface. Therefore the effect of the angle of 2.6° between the LOS of the outermost tracks and the along track direction was examined using both a 3-D atmosphere and a 2-D plane-parallel approximation and the error of the approximation was found to be in the order of the instrument noise. In effect, the results presented below for the central track are assumed to be representative for all tracks of the PREMIER IRLS.

For the temperature retrieval studies presented in this chapter, the radiance emissions of the CO_2 Q-branch at 12.6 µm are analysed, which were successfully used by Riese et al. (1999) to retrieve stratospheric and mesospheric temperature distributions from satellite observations. Only a single spectral grid point is used in the simulations. Retrieving temperature from radiance measurements at individual spectral grid points of the PREMIER IRLS is technically feasible due to the rather low noise equivalent spectral radiance of the proposed instrument. However, it is likely that the final instrument will have a broader spectral range than currently envisioned making several other CO_2 emission bands accessible, enabling even more accurate retrievals.

The temperature weighting functions presented here are computed by means of numerical perturbation (see Sect. 2.2.5). Figure 3.4 shows several weighting functions for the selected radiance channel at 12.6 µm ($\approx 792\,\mathrm{cm}^{-1}$). From 10 to 55 km altitude, the maximum sensitivity decreases from $4.49 \cdot 10^{-6}$ to $2.42 \cdot 10^{-7}\,(\mathrm{W}/(\mathrm{m}^2\,\mathrm{sr}\,\mathrm{cm}^{-1}))/\mathrm{K}$, the horizontal shift of the maximum towards the instrument decreases from 140 to 40 km, the horizontal FWHM along the LOS decreases from 575 to 475 km and the vertical FWHM is nearly constant at 0.95 km. The horizontal FWHM within the tangent plane is about 200 km.

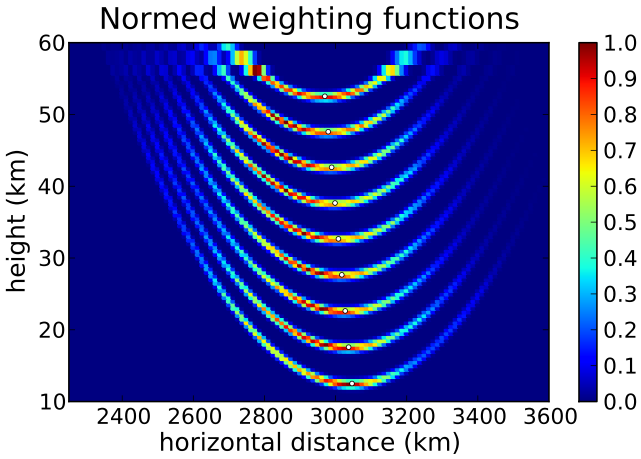

Figure 3.4: The temperature weighting functions for the PREMIER IRLS at 12.6 µm for mid-latitude atmospheric conditions. Weighting functions are scaled to one and superimposed by taking the maximum sensitivity at each atmospheric grid point. The plot shows weighting functions for 12.5, 17.5, . . . , 52.5 km tangent point altitude. The maximum value of the topmost weighting function is $2.42 \cdot 10^{-7}\,(\mathrm{W}/(\mathrm{m}^2\,\mathrm{sr}\,\mathrm{cm}^{-1}))/\mathrm{K}$ increasing to $4.49 \cdot 10^{-6}\,(\mathrm{W}/(\mathrm{m}^2\,\mathrm{sr}\,\mathrm{cm}^{-1}))/\mathrm{K}$ for the lowermost weighting function. The tangent points itself are marked using white circles. Note that the measurement grid of the instrument is ten times finer in the vertical than presented in this figure. The instrument is located on the left.

A typical cloudless mid-latitude atmospheric profile from Remedios et al. (2007) is used as background for the input atmosphere and as the a priori retrieval state. In practice, measurements contaminated by clouds will likely need to be filtered out, affecting the local retrieval result with a reduced resolution and higher a priori influence. The input atmosphere contains temperature, pressure, aerosol, CO_2, ozone and several other trace gases relevant for the 12.6 µm channel. Onto the temperature of this background and a priori atmosphere, waves with varying horizontal and vertical wavelength with a constant amplitude of 5 K are modulated to form the input atmospheres for the simulations; the latter atmospheres are generally referred to as “true” atmospheric state. Ideally, the retrieval would perfectly reproduce the true state.

For minimising the cost function, initially a Gauss-Newton scheme employing the m-form was used (see Sect. 2.3.2 and Eq. (2.11)). Later calculations were performed using the memory-conserving Levenberg-Marquardt algorithm in the n-form with sparse matrices (see Sect. 2.3.3 and Eq. (2.17)), employing the conjugate gradient scheme for solving the posed linear problems. Both methods were found to be adequate for the task, but the drastically reduced memory footprint made the latter method more attractive.

The true atmospheric state $\boldsymbol{x}_\mathrm{t} \in \mathbb{R}^n$ consists of the background atmosphere with the superimposed GW structure. It was chosen as initial guess (or starting point) to reduce simulation time. As this choice may sidestep potential convergence issues typically arising in non-linear inversions, it was confirmed for selected non-linear retrievals that they also converge to the same solution from other starting points. For example, using a polar atmosphere, which is quite different from the mid-latitude background, as starting point approximately doubles the number of required iteration steps, but converges to the same result. The covariance matrix $\mathbf{S}_\epsilon$ is assumed to be diagonal and takes into account noise ($10^{-5}\,\mathrm{W}/(\mathrm{m}^2\,\mathrm{sr}\,\mathrm{cm}^{-1})$) as well as the quasi-statistical part of the forward model errors (which is estimated to be 0.3% of radiance (Hoffmann, 2006)).

For regularisation of the PREMIER IRLS setup, the autoregressive model is employed (see Sect. 2.3.1). The correlation lengths are used as tuning parameters for the regularisation. The vertical correlation length c_v is set to 0.5 km and the horizontal correlation length c_h is set to 200 km. The effect of varying the correlation lengths on the resolution and noise of the retrieval result is examined in Sect. 3.5.3. The standard deviations σ_i are taken from the reference atmosphere of Remedios et al. (2007) and vary between 10 K and 14 K depending on altitude.

Only temperature values at grid points between 10 km and 65 km are retrieved, the other values are fixed to the a priori atmosphere. Thereby an additional 10 km are retrieved compared to the uppermost tangent point height of 55 km to compensate for eventual oscillations caused by the abrupt change from fixed a priori information to the retrieved profile. As the vertical retrieval grid becomes sparser above 55 km, this corresponds to 91 grid points with a 0.5 km spacing and 5 grid points above with a 2 km spacing per profile.

3.4. Analysis of baseline setup

This section presents an exemplary setup used to derive the GW observational filter and provides general diagnostics that give insight into the achievable resolution of the PREMIER IRLS.

Figure 3.4 exemplarily shows an end-to-end test. The unperturbed atmosphere common to all tests is depicted in panel (a). In this and most other

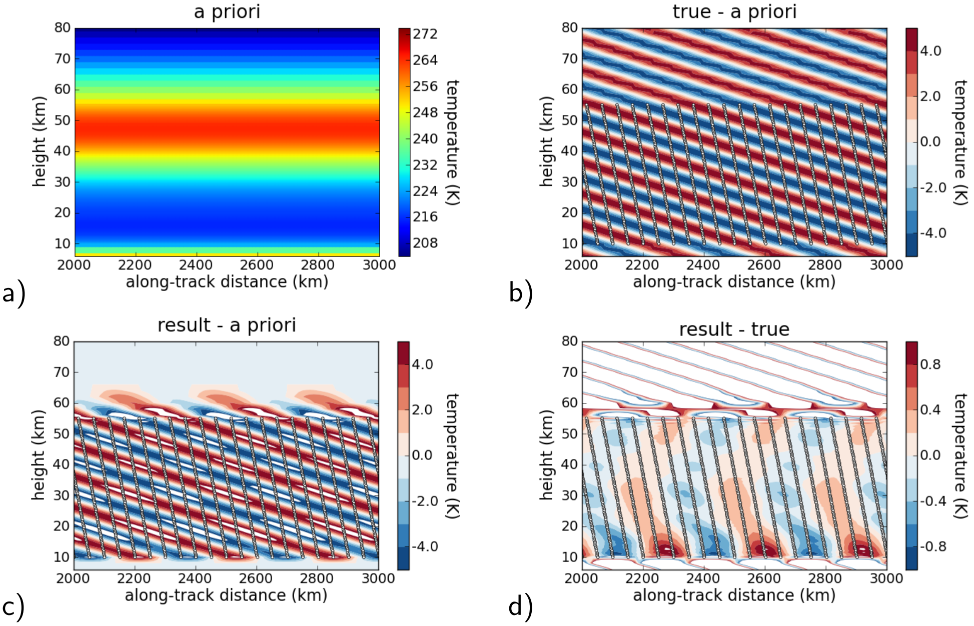

Figure 3.5: Retrieval end-to-end test used to generate the GW observational filter. The instrument flies from right to left and measures radiance coming from the right. A wave perturbation with 10 km vertical wavelength and 320 km horizontal wavelength tilted towards the instrument is super-imposed onto the a priori atmosphere depicted in panel **(a)**. The difference between the disturbed atmosphere and the a priori is shown in panel **(b)**. The difference between the retrieval result and the a priori, which is the retrieved wave perturbation, is depicted in panel **(c)** and the difference between the result of the retrieval and the true state is depicted in panel **(d)**. The tangent points of the satellite measurements are shown as white circles. For better representation of the investigated structure only kilometres 2 000 to 3 000 of the simulated 6 000 km are shown.

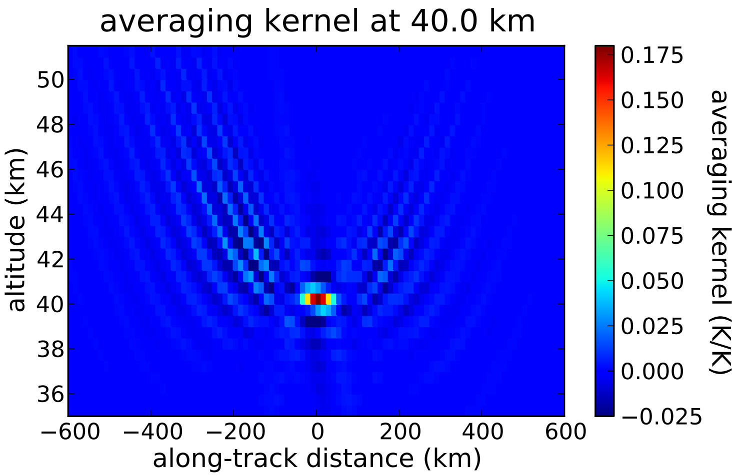

Figure 3.6: The averaging kernel matrix row of a single atmospheric state vector element located in the middle of the atmosphere at 40 km height. Each coloured box represents the influence of the atmospheric grid point of the true atmosphere on a single element of the retrieval result.

figures, only part of the full horizontal extent is depicted. A temperature perturbation with an amplitude of 5 K, a horizontal wavelength of 320 km, and a vertical wavelength of 10 km is depicted in panel (b). The tangent points of measurements are shown as small white circles. The outcome of the retrieval is shown in panel (c). One can clearly see that the wave structure is qualitatively well reproduced between 10 and 55 km height, which is the area covered by tangent points. In the area between 55 km and 65 km, the wave structure degrades into the unperturbed a priori atmosphere due to a lack of measurement information. The amplitude of the retrieved wave sometimes slightly surpasses ±5 K, which is shown as white areas in the wave troughs and crests. Panel (d) depicts the difference between the input atmosphere and the result; the error is overall less than 0.5 K between 20 and 50 km height.

One averaging kernel matrix row of the baseline setup with no modulated wave structure is depicted in Fig. 3.6. As each element in the row describes the influence of one point of the true atmosphere on the result, it can be reordered two-dimensionally according to their horizontal and vertical coordinates. The figure is representative for rows belonging to measurements with tangent points located between 15 km and 50 km height. Aside from a strong centred peak, one can see small "ripples" in the vicinity of the peak resembling the shape of the weighting functions (compare with Fig. 3.4). This is a natural consequence

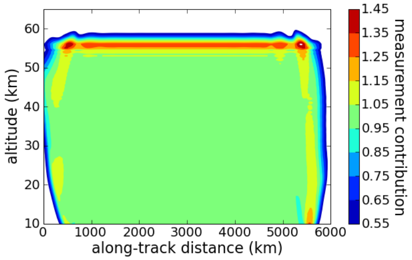

Figure 3.7: The measurement contribution for a baseline retrieval with no modulated wave structure (i.e. the atmosphere of Fig. 3.4(a)). Tangent points of measurements lie between ≈10 km and 55 km vertically and ≈500 km and 5 500 km horizontally.

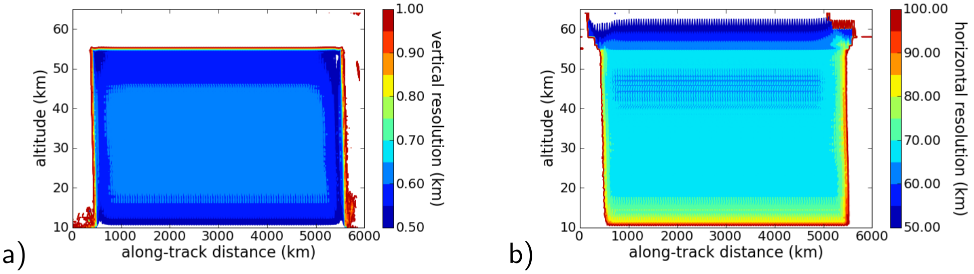

Figure 3.8: The vertical **(a)** and horizontal **(b)** resolution for a baseline retrieval with no modulated wave structure (i.e. the atmosphere of Fig. 3.4(a)).

of the averaging kernel matrix being a linear superposition of the weighting functions. The slight asymmetry is consequently caused by the asymmetry of the weighting functions.

Using the averaging kernel matrix, it is possible to deduce measurement contribution and resolution of the retrieval as described in Sect. 2.4. Typical values are plotted in Fig. 3.7 and Fig. 3.8. The tangent points of measurements lie within the region of 10 to 55 km height and 500 to 5 500 km horizontal distance, which closely corresponds to the region where the measurement contribution in Fig. 3.7 is between 0.95 and 1.05. Outside this region, retrieval results are biased to various extents by a priori information. As one is mainly interested in results with high measurement content and to simplify data processing, only data points with a measurement contribution between 0.95 and 1.05 are evaluated further. In practice one would likely define overlapping volumes and discard the borders.

The averaging kernel matrix can also be used to estimate vertical and horizontal resolution by mapping each row of the averaging kernel matrix associated with an atmospheric sample to the two-dimensional structure it represents, as depicted in Fig. 3.6. In this form, the FWHM in the vertical and horizontal direction can be calculated (see Sect. 2.4.1). For example, Fig. 3.8 shows the estimated horizontal and vertical resolution. Figure 3.6 shows how the averaging kernel matrix generally contains numerous very small elements that describe the influence of atmospheric sample points that are not directly above or beside the atmospheric sample point in question; as these are disregarded when calculating the resolution, this method provides only an approximate measure of resolution.

The vertical resolution in the central area of Fig. 3.8(a) is slightly better than the assumed vertical FOV, which has a FWHM of 750 m; however, without the smoothing by the a priori vertical correlation, a vertical resolution of nearly 500 m is achievable, corresponding to the vertical measurement grid spacing (see Sect. 3.5.3). This demonstrates that the achievable resolution is not necessarily limited by the FOV, but can be improved above this value by the deconvoluting properties of the tomographic retrieval. The horizontal resolution of about 70 km in Fig. 3.8(b) comes close to the horizontal measurement grid spacing of 50 km and is a significant improvement compared to the 475 to 575 km FWHM along the LOS of the individual weighting functions. Combined with the across track sampling and resolution of 25 km, PREMIER IRLS would achieve a horizontal resolution comparable to nadir sounders.

The simulations indicate that spatially over-sampled measurements (with respect to the weighting functions) can be separated and provide high spatial resolution in the vertical and horizontal domain.

The retrieval noise is the most important error for GW analysis as the effect of other, systematic, errors can be more readily handled by detrending (e.g. Ern et al., 2004). It is analysed and compared with GW amplitudes in Sect. 3.5.3.

3.5. Gravity wave observational filter

The GW observational filter defines how a wave perturbation of given horizontal and vertical wavelength is reproduced by a retrieval. The retrieval may modify the amplitude, wavelength, and phase of the wave. As the amplitude is the most important feature of a wave with respect to its energy for a given wavelength, the assessment presented here focuses on how well the amplitude of a given wave is reproduced.

3.5.1. Deduction from end-to-end simulations

To correctly determine the GW observational filter, non-linear end-to-end simulations must be performed for all wavelength of interest. To deduce the amplitude of the wave in the retrieved atmosphere, all atmospheric grid points between 15 and 50 km altitude and between 1 500 and 4 500 km along track are fitted against the modulated wave with amplitude as the only free parameter using a least-square fit. This method does not compensate for eventual shifts in phase of the retrieved wave structure, which generally occur when performing 1-D retrievals (Preusse et al., 2009). The interaction between the LOS and the GW causes perturbations in the measured radiances that lead to phase distortions if one assumes a horizontally homogeneous atmosphere during the retrieval. Any phase shift present in the retrieval result would directly reduce the sensitivity (even to zero for a phase shift of 180°). However, tests including the phase shift in the fit indicated that no phase shift was present for tomographic retrievals. According to Shannon's sampling theorem, it is impossible to perfectly reproduce waves with wavelength δ using a sampling distance that is longer than $\delta/2$; for this reason it was tested only for waves from a vertical wavelength of 1 km upwards and from a horizontal wavelength of 100 km upwards. Detecting GW signatures from actually measured profiles will require a more sophisticated process, as it is generally neither known if a GW is present in the data, nor what wavelength it may have, nor will it generally be monochromatic.

Figure 3.9(a) shows the GW observational filter for the baseline setup described in Sect. 3.3; it corresponds qualitatively with the shape of analytically derived sensitivity of Preusse et al. (2002) for CRISTA, albeit most notably the region of good sensitivity is moved well towards shorter horizontal wavelength. Due to the much denser measurement sampling of the PREMIER IRLS and the tomographic approach, much smaller waves become visible. The finest resolvable horizontal wavelength is about 100 km for a vertical wavelength of around 5 km with the wave being tilted towards the instrument. This is a significant improvement compared to the roughly 250 km horizontal wavelength of previous sensitivity studies involving the CRISTA instrument (Preusse et al., 2002). Please note that the resolvable horizontal wavelength is much smaller than the horizontal FWHM of the weighting function, which is roughly 500 km along the LOS

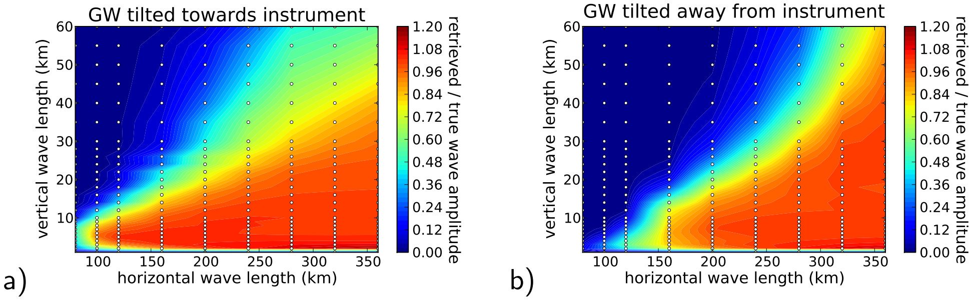

Figure 3.9: The GW observational filter for the PREMIER IRLS. Depicted is the ratio of retrieved wave amplitude to true wave amplitude for the baseline retrieval setup with varying modulated waves. Analysed wavelength combinations are indicated with white circles. Panel **(a)** shows the filter for the baseline setup with waves tilted towards the instrument and panel **(b)** shows the filter for a negative horizontal wave number (i.e. waves tilted away from the instrument).

and 250 km within the altitude range of the tangent point. GWs having a vertical wavelength of 2 km can be retrieved well, but the sensitivity drops quickly for shorter vertical wavelength, as the measurement grid is not fine enough to sufficiently sample them. Around two kilometre vertical wavelength and long horizontal wavelength, the retrieved amplitude becomes slightly larger than 1; this is caused by an insufficient vertical sampling of the atmospheric retrieval grid, similar to the horizontal sampling issue discussed below in Sect. 3.5.2 but less pronounced. For GWs with large vertical wavelength, the sensitivity becomes smaller depending strongly on the horizontal wavelength. But for waves with 300 km horizontal wavelength and longer, a sensitivity of at least 0.5 is given for all examined GWs having a vertical wavelength longer than 2 km. Sensitivity rises to 1 for all GWs with horizontal wavelength longer than ≈500 km (not shown).

Varying the phase of the modulated wave had no significant influence on the GW observational filter derived by the 2-D retrieval and is therefore not depicted. Small differences are only present for GWs having a vertical wavelength below 2 km where the visibility strongly depends on the relation between wave peaks and measurement grid. Changing the orientation of the waves from being tilted towards the instrument to being tilted away from it has a significant influence on the filter, as is shown in Fig. 3.9(b). The sensitivity to GWs with a horizontal wavelength below 150 km is lost, but this is partially compensated by an increased sensitivity to GWs with a larger vertical wavelength and an overall smaller transition region, in which waves become distorted. As the atmosphere

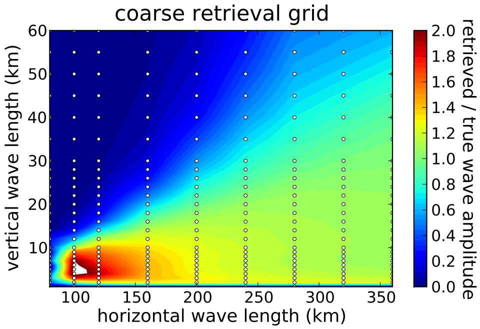

Figure 3.10: The GW observational filter derived with a horizontal retrieval grid spacing of 50 km instead of the usually employed 12.5 km. Please note the different colour scale compared to Fig. 3.9.

is not completely transparent, the sensitivity of the LOS to temperature changes is not only a function of height, but also of the horizontally travelled distance, which can be clearly seen in Fig. 3.4. As the sensitivity to GWs largely depends on the relation between LOS and wave trough and crest (Preusse et al., 2002) this is to be expected and needs to be taken into account when GW parameters are deduced from retrieved temperatures. The slope of the tangent point locations slightly influences the GW observational filter, but is not the cause for the observed asymmetry.

3.5.2. Sensitivity to retrieval grid

The horizontal spacing of the retrieval grid has a significant influence on the retrieval results as shown in Fig. 3.10. Before settling on a horizontal retrieval grid spacing of 12.5 km, several other horizontal grid spacings were tested ranging from 6.75 km to 400 km: the larger the horizontal spacing of the retrieval grid became, the more pronounced the amplification of wave amplitudes for short GW lengths became. This amplification can be seen in Fig. 3.10, which depicts the filter for a “natural” retrieval grid being identical with the measurement grid. At least for GWs with short wavelength, the measurement grid is apparently not the best choice for the retrieval grid.

The amplification of retrieved waves is most likely caused by the bi-linear interpolation of the temperature between the grid points. The fine structure of wave perturbations with short wavelength cannot be sufficiently represented by linear interpolation, which the retrieval compensates for by raising the wave amplitudes. Therefore, either a different atmospheric representation more suited to represent wave structures is needed or the retrieval grid needs to be refined to sufficiently capture the variations of the atmospheric state. Here, the second approach is employed. If the retrieval grid becomes finer than the measurement grid, the problem becomes underdetermined and needs to be regularised appropriately. Simulations have shown that resolution, measurement content and retrieval noise are not noticeably impacted by the refinement of the atmospheric grid.

For the examined waves, the artificial amplitude magnification is greatly diminished with a horizontal grid spacing of 25 km and negligible at 12.5 km. The horizontal retrieval grid spacing of 12.5 km was chosen to obtain exactness of the results at the cost of increased computational complexity.

As mentioned in Sect. 3.5.1, a similar effect occurs for waves of small vertical wavelength, which increases the retrieved amplitude by a factor of up to 1.2 for waves with about 2 km vertical wavelength. As the effect is much less pronounced and therefore easier to correct, the vertical retrieval grid has not been refined for this study.

3.5.3. Trade-off between retrieval noise and resolution

The vertical and horizontal correlation length of the a priori covariance plays the most important role in the auto-regressive regularisation applied here. Different values were examined before the values of 0.5 km and 200 km were chosen to provide a satisfactory trade-off between resolution and retrieval noise. In the Bayesian scheme applied in this chapter, the strength of the regularisation does not depend on the actual measurements. As the noise error indicates, the effect of noise on the retrieval result is sufficiently small so that the forward model can be assumed to be nearly linear so that the Jacobian matrix varies only negligibly. This means that the averaging kernel matrix stays nearly identical if noise is added to the measurements and in turn the results of this section are also representative for actual measurements affected by noise even though they were derived using unperturbed measurements.

Figure 3.11 shows the effect of vertical correlation length on vertical resolution and retrieval noise. One can clearly see the trade-off between vertical resolution and retrieval noise. To decrease the retrieval noise to ≈0.5 K for most of the vertical range, while still retaining a good vertical resolution, a correlation length of 0.5 km has finally been chosen. The choice of vertical correlation parameter also influences the GW observational filter. As expected, a large

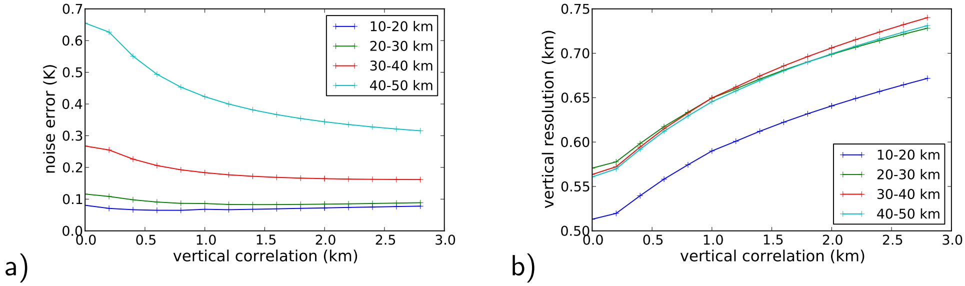

Figure 3.11: The effect of vertical correlation length on vertical resolution and noise error. The average resolution and retrieval noise for the four major height ranges are depicted.

correlation length slightly reduces the region where sensitivity is very close to one. Further, increasing the vertical correlation length beyond 2 km leads to unwanted oscillations in the averaging kernel matrix, which confirms the choice of a much smaller value.

The retrieval noise is not influenced significantly by the horizontal correlation factors that were examined (12.5 to 400 km). The main effect of the horizontal correlation is to stabilise the underdetermined retrievals. Reducing the horizontal correlation length from 200 km to 100 km improves the horizontal resolution from 75 km to ≈70 km, but the non-linear retrievals do not converge for some wave structures with very small vertical and horizontal wavelength. Reducing the horizontal correlation further, the horizontal resolution derived from the averaging kernel matrix goes as low as 50 km for a horizontal correlation length of 12.5 km, coming close to the horizontal measurement grid at the cost of ever increasing convergence issues. To avoid any convergence problems, the correlation length is set to 200 km. The GW observational filter behaves as expected when varying the horizontal correlation length, as GWs become increasingly dampened for larger correlation lengths. However, this barely affects the region of the GW observational filter close to one but influences mostly the transition region.

GWs can be detected if their amplitude exceeds retrieval noise. Therefore, it is important that the retrieval noise is smaller than the amplitude of GWs that shall be observed. According to Shannon's sampling theorem, with a vertical measurement grid of 500 m one cannot resolve waves with a vertical wavelength shorter than 1 km. Practically, a slightly larger vertical wavelength than 1 km is required, meaning that one can expect to consistently resolve waves from about 2 km vertical wavelength upward, which is confirmed by the GW observational filter. The maximal amplitude of actual GWs of that vertical wavelength can be determined according to the temperature amplitude saturation limit (e.g. Preusse et al., 2008). This limit $\hat{T}_{\max}$ due to static instability is proportional to the vertical wavelength:

$$\hat{T}_{\max}=\frac{\lambda_z}{2\pi}\frac{\overline{T}}{g}N^2. \tag{3.1}$$

Using a buoyancy frequency of $N=0.02\,\mathrm{s}^{-1}$ and a background temperature $\overline{T}$ of 250 K, this gives a saturation amplitude of greater than 3.2 K for waves with vertical wavelength greater than or equal to 2 km at about 40 km height. Comparing this value to the 0.5 K of retrieval noise for that height range shows that such GWs are easily detectable also in the presence of noise. As the temperature amplitude saturation limit increases with vertical wavelength, any wave with vertical wavelength longer than 2 km is therefore also detectable with the given noise level.

3.5.4. Comparison of 2-D and 1-D retrievals

A 2-D retrieval reproduces wave structures with better sensitivity and less distortions than 1-D retrievals (that assume a horizontally stratified atmosphere). As each individual 1-D retrieval cannot take the horizontal variation of the GW into account, it compensates for the effect it has on the measured radiances with a phase shift of the retrieved 1-D vertical wave structure. For example, Fig. 3.12 shows side-by-side the retrieval results for a wave of 320 km horizontal wavelength and 30 km vertical wavelength. Panel (a) was generated by a series of 1-D retrievals, each using a single vertical measurement profile of the simulated measurements as input. The resulting temperature profiles were assembled to a 2-D structure by adding each retrieved temperature profile at the mean horizontal location of the tangent points of the involved measurements. Comparing the retrieved wave structure with the true wave structure (which is depicted as the black contour plot in the figure), the phase of the wave structure of the 1-D retrieval is obviously shifted by nearly 180°; the amplitude does not surpass 2.5 K and is thereby much smaller than the expected 5 K. In addition, the amplitude is also strongly height-dependent. The vertical wavelength is also slightly reduced. On the other hand, the 2-D retrieval shows a more pronounced wave structure and fits very well to the true wave (again shown as black contour plot) in the region between 30 km and 55 km. Figure 3.9 shows that the 2-D retrieval has an amplitude dampening factor of 0.9.

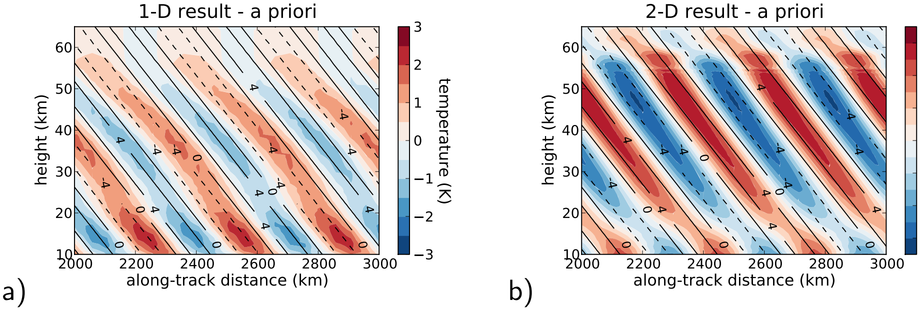

Figure 3.12: The retrieval result for a series of conventional 1-D retrievals in panel **(a)** and a 2-D retrieval in panel **(b)**. The GW has a wavelength of 30 km in the vertical and 320 km in the horizontal. Please note the different colour mappings. The climatological background profile was subtracted from the result. A contour plot of the true modulated wave structure has been included as black lines to visualise the phase shift of the 1-D retrieval.

The GW observational filter deduced by using 1-D retrievals is shown in Fig. 3.13(a). Obviously, fewer wave patterns can be reliably retrieved. Especially waves with large vertical wavelength are affected. In contrast to Fig. 3.9, also the phase of the wave needs to be fitted, otherwise the sensitivity would be even worse. The phase shift is depicted in Fig. 3.13(b). White colour indicates that the wave could not be retrieved well enough to reliably determine the phase shift. The phase shift changes continuously according to the horizontal and vertical wavelength as predicted by Preusse et al. (2002) and correlates with the dampening of the wave. This comparison shows that tomographic retrievals are clearly superior to 1-D schemes for the purpose of GW detection.

3.5.5. Deducing the gravity wave observational filter from the averaging kernel matrix

A more efficient way to derive the GW observational filter is to analyse just the averaging kernel matrix of a retrieval for a climatological atmosphere of the region of interest.

Assuming the non-linearity of the forward model to be negligible and thereby the Jacobian matrix to be constant across the space spanned by the a priori atmosphere and all wave perturbations, the averaging kernel matrix **A** will be identical for all wave structures including the unperturbed atmosphere. Neglect-

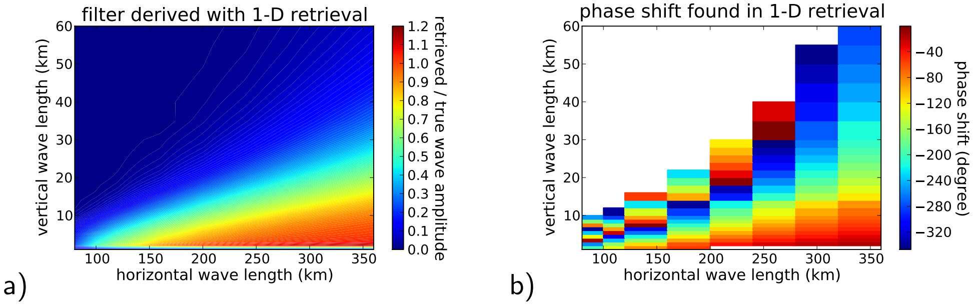

Figure 3.13: The GW observational filter derived by a series of a 1-D retrievals. Panel **(a)** depicts the GW observational filter and panel **(b)** shows the phase shift of the wave as determined by the non-linear least square fit for those retrievals, where a wave with an amplitude greater 1 K was found.

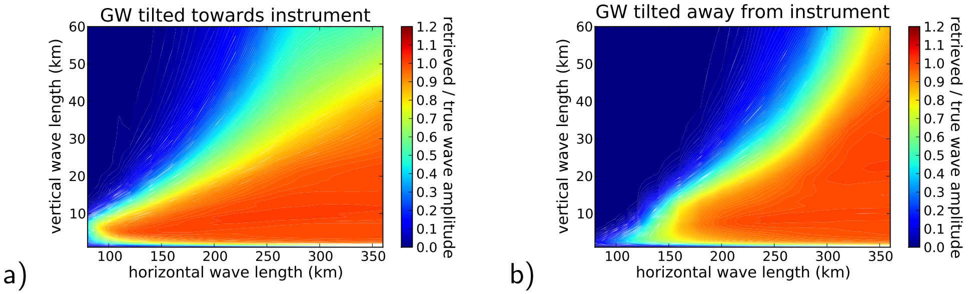

Figure 3.14: The GW observational filter as deduced from the averaging kernel matrix. Each rectangle represents the mapping of a wave onto itself. Panel **(a)** shows the diagonal elements for waves tilted towards the instrument (see also Fig. 3.9(a)), panel **(b)** shows the diagonal elements for waves tilted away from the instrument (see also Fig. 3.9(b)).

ing measurement errors, it follows that

$$\boldsymbol{x}_{\mathrm{f}} - \boldsymbol{x}_{\mathrm{a}} = (\mathbf{A}(\boldsymbol{x}_{\mathrm{a}} + \boldsymbol{x}_{\delta}) + (\mathbf{I} - \mathbf{A})\boldsymbol{x}_{\mathrm{a}}) - \boldsymbol{x}_{\mathrm{a}} = \mathbf{A}\boldsymbol{x}_{\delta}, \tag{3.2}$$

with $\boldsymbol{x}_{\delta}$ being the modulated wave structure. This shows that the averaging kernel matrix directly maps the true wave perturbations $\boldsymbol{x}_{\delta}$ onto the retrieved wave structure.

Figure 3.14 shows the GW observational filter derived in this manner. Just as for the non-linear end-to-end simulations, only that part of the $\boldsymbol{x}_{\mathrm{f}} - \boldsymbol{x}_{\mathrm{a}}$ vector is used to derive the sensitivity that has a good measurement contribution and lies well within the region covered by tangent points of measurements. The perturbations of up to 5 K are small enough so that the assumption about linearity of the forward model sufficiently holds and the filter derived in this manner replicates closely the structure of the filter derived from non-linear end-to-end tests.

This method is therefore an efficient way to quickly preview the effect of changes in the setup before proceeding to the much more computationally intensive non-linear end-to-end simulations. The latter are still required, as the linear approximation cannot be used to examine, for example, the convergence properties of the non-linear retrieval for different atmospheric states.

3.5.6. Gravity wave observational filter for denser measurement grids

For instrument design, it is of interest, which measurement grid enables the detection of GWs with the largest range of horizontal and vertical wavelength. In this section, the method presented in Sect. 3.5.5 is used to quickly evaluate the influence of different horizontal measurement grids onto the GW observational filter. For simplicity's sake, it is assumed that the change in measurement density can be achieved without a corresponding change of measurement noise. The horizontal retrieval grid is kept identical for each of the following retrieval experiments, as potential non-linear effects cannot occur in this linearised experiment.

Due to Shannon's sampling theorem, it is expected that the shortest visible horizontal wavelength corresponds to twice the horizontal sampling distance. Increasing the horizontal measurement sampling density will therefore likely increase the visibility of waves with shorter horizontal wavelength. However, it is not obvious how this interacts with the vertical wavelength. In Fig. 3.15, analytical GW observational filters are derived from the averaging kernel matrix for different horizontal measurement grids and GWs tilted towards the instrument. Panel (c) depicts the PREMIER IRLS measurement grid with a horizontal grid spacing of 50 km for reference. The lower right panel shows the effect of increasing the horizontal measurement grid spacing to 100 km. Effectively GWs with a horizontal wavelength between 100 km and 200 km become unobservable, which are visible with the PREMIER IRLS measurement grid. While the GW observational filter does not change much for large vertical wavelength, several GWs with short vertical wavelength and a horizontal wavelength between 200 km and 250 km also vanish from the retrieval results. The effect of refining the horizontal measurement grid to sample every 25 km is depicted in

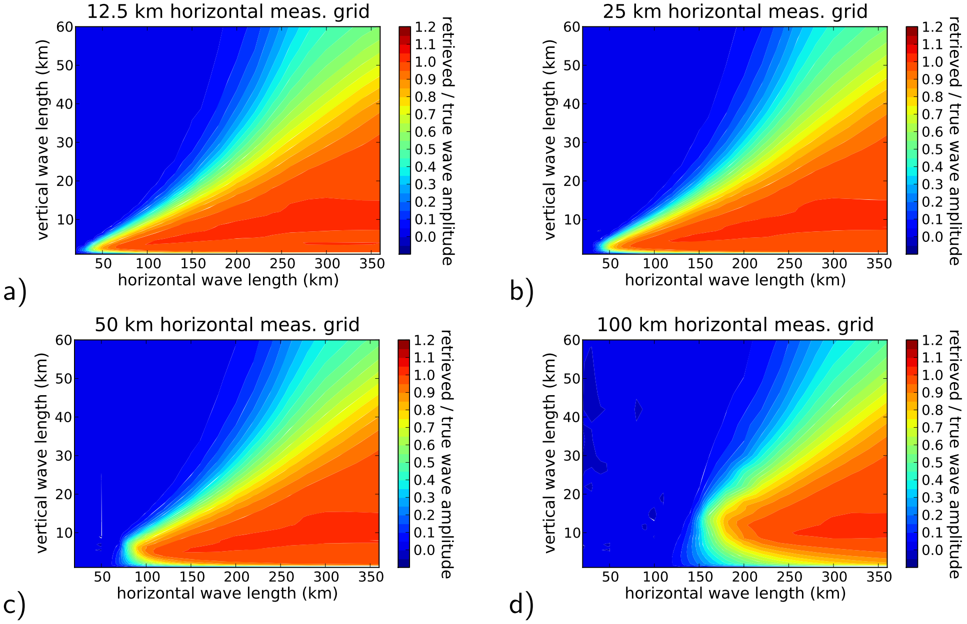

Figure 3.15: The GW observational filters for different horizontal measurement grids. These were deduced from the averaging kernel matrix for GWs tilted towards the instrument only. Panel **(a)** depicts the filter for an instrument with a horizontal measurement grid of 12.5 km. The filter for an instrument with a horizontal measurement grid of 25 km is shown in panel **(b)**. In panel **(c)** the filter for proposed PREMIER IRLS instrument is shown. Panel **(d)** depicts the filter for an instrument with a horizontal measurement grid of 100 km.

panel (b). As expected, now GWs with horizontal wavelength down to 50 km can be retrieved, albeit only if their vertical wavelength lies between 1 km and 6 km (or slightly larger for larger horizontal wavelength). But also waves with 100 km horizontal wavelength and very short vertical wavelength of 1 km to 4 km are subject to a decreased dampening. Refining the measurement grid further down to sampling every 12.5 km, shown in panel (a), does not improve the GW observation filter significantly, due to the restrictions imposed by the vertical wavelength and the vertical measurement grid density. Please note that refining the horizontal measurement grid also improves slightly the visibility of GWs with large vertical wavelength as becomes most obvious when directly comparing that range between panels (a) and (d).

Improving the PREMIER IRLS horizontal measurement grid to sample every 25 km offers additional insight into GWs with horizontal wavelength between

50 km and 100 km and vertical wavelength between 1 km and 6 km. Numerical simulations by Piani et al. (2000) and Lane et al. (2001) indicate that convective forcing in the tropics generates GWs in this range, which could in turn account for up to 30 percent of the forcing required for downward propagation of the westerly phase of the quasi-biennial oscillation, and up to 15 percent of the required forcing in the easterly phase of the quasi-biennial oscillation. Observing waves with such wavelength is thus of great value. Refining the measurement grid further seems to bring only diminishing returns, while making it coarser than the specified density would sacrifice many otherwise visible GWs.

3.6. Chapter summary

Various non-linear end-to-end simulations were performed using simulated measurements of the PREMIER IRLS with different input atmospheres consisting of a cloudless climatological background atmosphere with modulated wave perturbations. In this way, the gravity wave (GW) observational filter was determined that shows the amplitude ratio between a given wave perturbation and its reproduction by the tomographic retrieval setup. It was shown that the PREMIER IRLS using the dense measurement grid of the dynamics mode combined with tomographic retrievals can resolve much finer GW structures than previously possible without any phase distortion. GWs with a horizontal wavelength down to 100 km may be resolved with their amplitude depending on their vertical wavelength.

Different retrieval grids were examined and it was found that using a coarse retrieval grid corresponding to the measurement grid introduces an amplification of GWs with short horizontal wavelength. It is therefore advantageous to use a retrieval grid that is sufficiently fine for the purpose of representing examined and existing atmospheric structures. Otherwise, retrieval results may be distorted by artefacts.

By tweaking the correlation length of the a priori covariance matrix, it is possible to reduce the retrieval noise at the cost of a reduced resolution. Convergence issues arise when the horizontal correlation length is reduced to or below 100 km. Various horizontal and vertical correlation lengths were examined and a horizontal correlation length of 200 km and a vertical correlation length of 0.5 km were finally chosen. With these figures, the expected retrieval noise is well below the temperature amplitude saturation limit of resolvable GWs, which implies that it should not hinder the detection of GWs. The resulting horizontal resolution is ≈70 km, much better than the horizontal correlation length might suggest. If one is willing to manually deal with eventual convergence issues, even a horizontal resolution of only ≈50 km might be achievable.

A linear approximation of the GW observational filter derived from the averaging kernel matrix is a helpful tool when examining different setups. One can generate the averaging kernel matrix for a climatological atmosphere and use this matrix to inexpensively calculate an approximation of the GW observational filter for a wide range of GWs. The GW observational filter derived in this manner resembles closely the GW observational filter derived by more accurate end-to-end simulations.

The GW observational filter derived by conventional 1-D retrievals has a severely reduced sensitivity compared to the GW observational filter derived by the tomographic retrieval technique. Comparing the results for selected wave perturbations, the result of the tomographic retrieval was much closer to the true state than the result of the 1-D retrievals. Further, the tomographic retrieval is apparently not subject to the phase shift that affects 1-D retrievals.

The PREMIER IRLS should provide 3-D temperature measurements with sufficient altitude coverage and resolution in the stratosphere to allow for simultaneous determination of GW temperature amplitudes and the associated horizontal and vertical wavelength. Therefore, the dynamics mode of the PREMIER IRLS satellite instrument will be well suited for examining the dynamic structure of the upper troposphere and stratosphere. The presented tomographic retrieval scheme resolves the dense 3-D measurements of the PREMIER IRLS dynamics mode with a comparable 3-D resolution and is thereby well suited for the retrieval of temperature data for the analysis of GWs. The across track resolution of PREMIER IRLS corresponds to the across track measurement sampling of 25 km. Further, it is possible to retrieve temperature data with a vertical resolution of 750 m; depending on the retrieval setup even a vertical resolution of 500 m seems achievable, surpassing the full-width at half-max of the vertical field-of-view (750 m). In addition, the dense measurement grid with a horizontal grid spacing of 50 km can be nearly fully exploited with an achievable horizontal along track resolution of ≈70 km. Such a 3-D resolution is unprecedented for limb-sounders and approaches the horizontal resolution of nadir sounders.

> I see a certain order in the universe and
> math is a way of making it visible.
>
> *(May Sarton)*

4. A 3-D tomographic retrieval setup for the air-borne limb-imager GLORIA

In this chapter, the methodology developed in Chap. 2 is applied onto the new air-borne GLORIA (Gimballed Limb Observer for Radiance Imaging of the Atmosphere; Friedl-Vallon et al., 2006; Ungermann et al., 2010b). By employing a two-dimensional (2-D) detector, it can take an unprecedented amount of spatially resolved spectral samples. GLORIA is unique in being able to pan the detector, which allows for viewing the same volume of air from multiple angles. The combination of these two properties shall allow, for the first time, to perform tomographic three-dimensional (3-D) retrievals. The instrument is presented briefly in Sect. 4.1. The achievable retrieval quality of such a 3-D retrieval setup for different flight tracks of the air-borne carrier is examined in Sect. 4.1 to 4.4. The effect of the temporal variability of the atmosphere on the 3-D retrieval is examined in Sect. 4.5.

The new limb-imaging technique allows the detection of meso-scale structures in atmospheric temperature as well as in the chemical composition of the upper troposphere/lower stratosphere (UTLS). While the focus of Chap. 3 was on meso-scale temperature structures generated by gravity waves, the investigations of the capabilities of GLORIA focus on structures in atmospheric composition and variability of the UTLS caused by trace gas exchange between troposphere and stratosphere. Changes and variability of composition in the UTLS are, in turn, major drivers of surface climate change (e.g. Forster and Shine, 1997).

In the past, most progress in our understanding of UTLS processes has been made by detailed in-situ air-borne measurements (e.g. Hoor et al., 2004; Schiller et al., 2009) or limb-sounding satellite instruments (e.g. Hegglin et al., 2009).

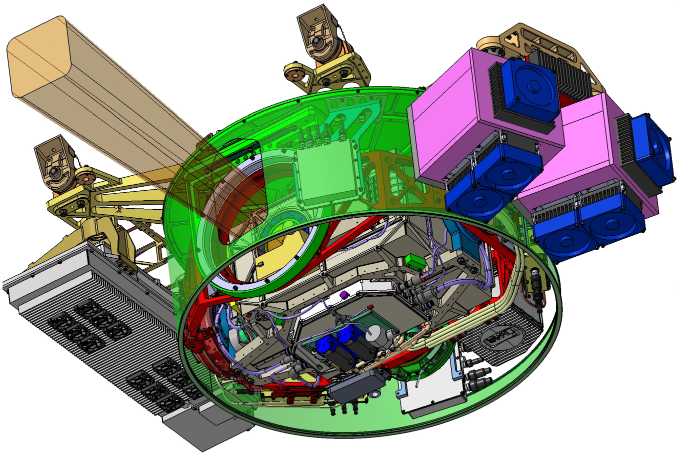

Figure 4.1: The design of the GLORIA instrument. The yellow beam indicates the viewing beam of the instrument. The outermost, vertical axis of the cardanic frame is given by the green cylinder, which also closes the belly pod to the air stream (Figure courtesy of ZAT, Forschungszentrum Jülich).

However, in-situ air-borne observations and current limb-observations by satellites are rather limited in terms of coverage or spatial resolution. Birner et al. (2006) state that a high vertical resolution in the UTLS is crucial, for example to properly represent the only 1 km thick tropopause inversion layer, which is essential for mixing between stratospheric and tropospheric air. Nadir sounders in general, but also current satellite-borne limb-sounders, do not have the necessary vertical resolution, implying that assimilating their retrieved profiles into global models is actually detrimental for accurately simulating this critical inversion layer.

Current air-borne limb-emission sensors such as MIPAS-STR (e.g. Höpfner et al., 2001; Keim et al., 2008) and CRISTA-NF (e.g. Spang et al., 2008; Hoffmann et al., 2009) on-board the high-flying Russian aircraft Geophysica provide adequate spatial sampling in two dimensions (vertical and along the flight track). However, they are limited by a relative broad weighting function (about 200 km) of the observations in the viewing direction (perpendicular to the flight track).

Where such conventional remote sensing instruments cannot resolve the atmosphere well along their line-of-sight (LOS), the new GLORIA limb-sounder (Fig. 4.1) has the capability to derive, for the first time, fine atmospheric structures in three dimensions from air-borne observations. GLORIA is a development of the Research Centre Jülich and the Karlsruhe Institute of Technology. Deriving highly resolved 3-D temperature and trace gas concentration fields from GLORIA observations (e.g. for transport studies) poses a tomographic problem that requires special attention to handle the computational complexity. Further, GLORIA serves as an air-borne precursor for the proposed satellite-borne PREMIER IRLS instrument discussed in the previous chapter.

Due to the different observation geometries between forward- or backward-looking satellite-borne instruments on the one hand and side-ways looking air-borne instruments on the other hand, the posed 3-D tomographic problem is quite different from state-of-the art 2-D tomographic retrievals (e.g. Carlotti et al., 2006; Livesey et al., 2006) as presented in the preceding chapter. It is therefore not a simple extension of 2-D retrievals and its characteristics are quite different.

To properly plan the first flights of the GLORIA instrument, it is important to know how to properly use it to examine the UTLS. On the one hand, quite a few parameters need to be defined beforehand, including the measurement mode, a proper flight path of the carrier, and the employed panning strategy. On the other hand, advection plays also a major role for the 3-D retrieval quality, as tomographic measurement periods take too long (hours) to neglect the effect of horizontal transport. The following sections examine these questions in detail, give insight into the achievable 3-D resolution of such retrievals, and provide thereby crucial information for flight planning.

4.1. The GLORIA infrared limb-imager

The GLORIA instrument essentially combines a Fourier transform infrared spectrometer with a two-dimensional detector array measuring in the spectral region from $770\,\mathrm{cm}^{-1}$ to $1\,400\,\mathrm{cm}^{-1}$ (see Tab. 4.1 for GLORIA instrument characteristics). The 2-D detector array will consist of about 256×256 pixels, of which 128×128 pixels will be used to provide more than 16 000 simultaneous limb-views with elevation angles ranging from -3.27° (corresponding to a tangent altitude of roughly 4 km at an observer altitude of 15 km) to slightly upwards and with a horizontal field-of-view (FOV) of 4.07°. To increase the signal-to-noise ratio, individual array pixels will be co-added to obtain sampling patterns of specific scientific measurement modes.

GLORIA instrument specification (15 km observer altitude)			
Parameter	Unit	Dynamics M.	Chemistry M.
lower limit of FOV	degree	−3.27	
upper limit of FOV	degree	0.8	
vertical FOV	degree	4.07	
horizontal FOV	degree	4.07	
panning	degree	45–135	90
vertical sampling	km	0.14	0.56
horizontal sampling	km	2.2	17.9
spectral coverage	cm^{-1}	770–1400	770–1400
spectral resolution	cm^{-1}	1.25	0.1
NESR	$\text{nW}/(\text{cm}^2\,\text{sr}\,\text{cm}^{-1})$	3.5	2
acquisition time	s	$\approx$3	$\approx$36

Table 4.1: This table shows the principal technical characteristics of the GLORIA instrument for two exemplary measurement modes. The panning angle might be slightly reduced depending on the aircraft, onto which GLORIA will be mounted. Both spectral resolution and NESR are given for apodised spectra.

The GLORIA instrument has the ability to pan the LOS relative to the flight direction. This is realised by using a gimbal mount that also stabilises the LOS during measurements. While conventional air-borne instruments usually point at 90° relative to the flight direction, GLORIA is capable of adjusting its LOS between 45° and 135° (as seen from above the carrier with 0° being the flight direction of the carrier). This allows for viewing the same air volume from multiple angles. Depending on the aircraft, onto which GLORIA will be mounted, the possible range of angles may be slightly reduced due to obstructing parts of the aircraft. In combination with adapted flight paths of the carrier, this shall enable the retrieval of three-dimensionally resolved air volumes.

Another advantage of the instrument concept is that it allows for the adaption of the trade-off between spatial and spectral resolution according to the scientific needs. Currently only the “dynamics mode” and “chemistry mode” (see Tab. 4.1) are specified, but further modes can be implemented without changing the hardware, if the need for a different trade-off between spatial and spectral sampling should arise from a scientific question. As this chapter explores the capabilities of GLORIA for tomographic retrievals, the focus is on the measurement mode that offers the highest temporal and spatial sampling, which is the dynamics mode of Tab. 4.1. As an example for the spectral resolution of the dynamics mode, simulated spectra for mid-latitude atmospheric conditions and

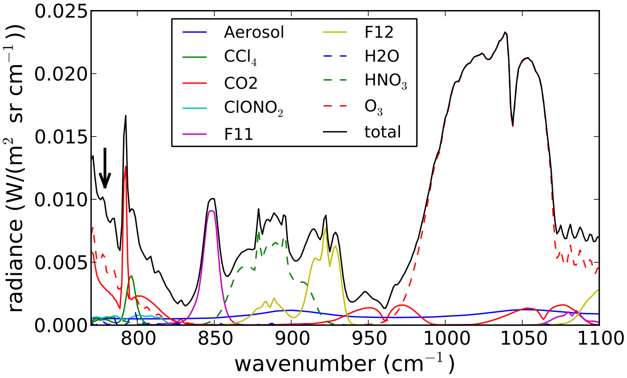

Figure 4.2: Simulated limb radiance spectra for the GLORIA instrument operating in dynamics mode. Calculations are based on mid-latitude atmospheric conditions (Remedios et al., 2007) and 12 km tangent altitude. The black curve indicates total radiance. The other curves indicate radiance for single emitter atmospheres (see legend). The black arrow indicates the O_3-peak used for the retrievals.

12 km tangent altitude are shown in Fig. 4.2. Even at this relatively coarse spectral resolution, infrared emission features of important atmospheric constituents are clearly visible. For example CO_2, F11, F12, CCl_4, O_3, and HNO_3 exhibit distinct peaks in Fig. 4.2 and were also successfully retrieved by Weigel et al. (2010) using the CRISTA-NF instrument and channels with a spectral resolution comparable to what the dynamics mode of GLORIA offers.

The simulations presented below assume that GLORIA will be mounted within the belly-pod of the High Altitude and Long Range Research Aircraft (HALO). This plane is based on the business jet Gulfstream G550 with modifications that allow the mounting of a wide variety of scientific equipment. The maximum speed of HALO is 940 km/h and the maximum cruise altitude is 15.5 km (DLR, 2010). As the plane cannot constantly operate at its peak speed or altitude, an average speed of only 850 km/h and a peak altitude of 15 km is assumed in the following for simplicity's sake.

4.2. Simulation setup

One intent of the simulations presented in the following is to demonstrate the feasibility of tomographic retrievals. The general idea is to reconstruct a 3-D at-

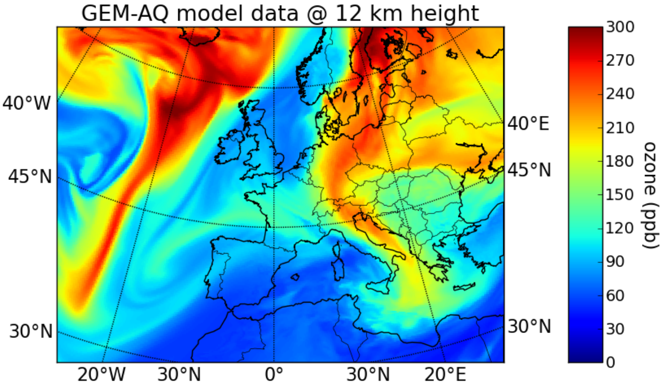

Figure 4.3: Simulation of ozone distribution by the GEM-AQ model. Depicted is ozone (ppb) for 3 July 2006 12:00 UTC at 200 hPa (12 km) with a resolution of ≈15×15 km^2.

mosphere from simulated GLORIA measurements. To keep the inversion rather simple, only a single target shall be reconstructed. Ozone was chosen as an example for a tracer that can be used to examine the UTLS air exchange and which therefore fits to one scientific focus of GLORIA. To that end, a three-dimensional GEM-AQ (Global Environmental Multi-scale model, Air Quality; Kaminski et al., 2008) data set is employed as test atmosphere, which is used to generate simulated measurements of GLORIA. The GEM-AQ model simulation of the synoptic situation during the European heat wave of July 2006 exhibits an interesting horizontal structure in O_3 close to a tropopause fold (Struzewska and Kaminski, 2008) and thus was selected as test data set. Figure 4.3 shows part of this structure, an ozone filament over the north west of France at 200 hPa with a horizontal extension of about 250 km × 2 000 km. This filament is a remnant of upper stratospheric air mixed into the lower-most stratosphere. Ozone values inside this filament are about 50 % increased in comparison to the ambient air.

The horizontal sampling of the GEM-AQ data set is about 15 km while the vertical sampling in the UTLS region is about 1 km. A volume from 8.64° E to 8.64° W and from 40° N to 52° N is used for the simulations. This region is sampled with a horizontal grid size of ≈11 km to generate the simulated measurements. For the inversion, the atmosphere is sampled with this fine grid only from 2.88° E to 2.88° W and from 44° N to 48° N, whereas the outer region is covered by only three samples on each side to reduce the number of unknowns. The vertical sampling is 1 km from 1 km to 6 km altitude, 0.25 km from 6 km to

Parameter	Value
α_0	0.1
α_1^x	$0.8\,\mathrm{km/ppb}$
α_1^y	$0.8\,\mathrm{km/ppb}$
α_1^z	$4 \cdot 10^{-4}\,\mathrm{km/ppb}$

Table 4.2: Regularisation strength for the 3-D retrieval experiments.

16 km, 1 km from 16 km to 20 km, and 2 km from 20 km to 60 km. The retrieval shall derive ozone in the vertical region from 4 km to 20 km over the full horizontal extent from the simulated measurements. The inversion is simplified by assuming perfect knowledge of the top-column above 20 km and all constituents except ozone in the retrieved area. In this idealised study, the properties of the tomographic retrieval method shall be examined and therefore other sources of uncertainty are neglected.

Temperature, pressure, CCl_4, CO_2, $ClONO_2$, H_2O, HNO_3, and O_3 are used in the simulations as these contribute most of the radiation of the employed channel. As not all these trace gases are contained in the GEM-AQ model data, CCl_4, CO_2, $ClONO_2$, and HNO_3 are taken from mid-latitude profiles of Remedios et al. (2007). For this study, clear-sky conditions are assumed.

For the 3-D retrievals, Tikhonov regularisation is employed as described in Sect. 2.3.1. Initial simulations employing the autoregressive approach for regularisation exhibited artefacts that necessitated a stronger regularisation approach. Ozone mid-latitude values and standard deviations of Remedios et al. (2007) are used for the a priori vector $\boldsymbol{x}_\mathbf{a}$ and regularisation matrix $\mathbf{L_0}$. As initial guess $\boldsymbol{x}_\mathbf{0}$, mean ozone values for polar conditions are taken from the same source. The regularisation strength has been set to the values given in Tab. 4.2. A parameter study of the regularisation parameters showed that these relative weights deliver the visually most pleasing results and that the overall strength is L-curve optimal (see Sect. 4.3.3). The resulting linear equation system matrices $\mathbf{M}$ have a condition number of ≈450 000, which allows for a satisfying convergence speed of the conjugate gradient scheme.

The results presented in the following use simulated measurements, which are each averaged over two rows of the GLORIA detector. This combines 256 detector pixels and thereby deviates from the envisioned co-adding of the dynamics mode. Assuming 15 km flight altitude, this corresponds to a vertical measurement sampling distance of ≈210 m at 12 km tangent height, ≈280 m at 10 km tangent height, and ≈330 m at 8 km tangent height. The averaging over two rows instead of over a single one has been employed largely because the GEM-AQ atmosphere model data do not offer such fine vertical details in the region of interest and because the reduction of vertical sampling significantly decreases simulation times. In the presence of clouds, affected detector pixels will be removed from the measurement. A single image with the described 64 individual measurements will be generated by GLORIA every ≈3 seconds. For the description of the employed panning, see Sect. 4.3.4. The measurement noise is modelled by a stochastic additive offset component and a stochastic multiplicative gain component. This assumes that any systematic component can be handled by calibration or during the retrieval itself. According to the specification of GLORIA, the offset component for 256 averaged detector pixels is expected to have a standard deviation of $0.1875 \cdot 10^{-5}\,\mathrm{W/(m^2\,sr\,cm^{-1})}$. For the gain component of 256 averaged detector pixels, a stochastic component with a standard deviation of 0.1 percent is assumed to remain after removing the systematic component of the error. Both simulations with and without added noise are performed according to this specification as presented below. The simulations use only a single channel at $778.5\,\mathrm{cm^{-1}}$, which was previously used by Weigel et al. (2010) to derive ozone from CRISTA-NF measurements. This channel is rather optically thin in the troposphere, close to the CO_2 Q-branch at $12.6\,\mu\mathrm{m}$ usually employed for deriving temperature, and relatively unaffected by water vapour. A realistic setup would naturally need more channels to compensate for instrument effects, aerosol, further trace gases, etc. On the other hand, at least for O_3 it is possible to find and add further effective channels to reduce measurement noise.

The simulated radiances and transmittances for the baseline retrieval presented in Sect. 4.3 are shown in Fig. 4.4. The tangent point altitude for rays pointing upwards lies below and behind the observer, thus the decrease in tangent point altitude at the side of the plots. The transmittance starts with 0.9 and decreases slowly towards 0.1 for the lowest tangent altitude. This implies that the atmosphere is not optically thin and that the weighting functions are therefore highly asymmetric, especially for the lower tangent altitudes.

The vertical FOV of two rows is assumed to have a full width at half maximum (FWHM) of 0.08°, which corresponds roughly to 280 m at 200 km distance. The horizontal FOV is assumed to correspond to a boxcar function. To properly simulate the FOV, multiple pencilbeams are calculated and convolved with a Gaussian weighting function (see also Fig. 2.2).

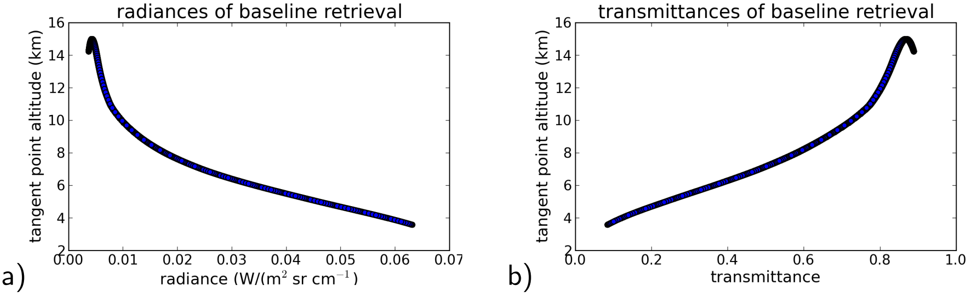

Figure 4.4: Radiances in panel **(a)** and transmittances in panel **(b)** for the baseline setup.

It is now important to define the granularity, with which the FOV weighting function should be sampled by pencilbeams. As the computational effort for a retrieval is directly proportional to the number of employed pencilbeams, one needs to compromise between accuracy and performance. Figure 4.5 depicts the accuracy of $\boldsymbol{F}$ and $\mathbf{F}'$ in relation to a reference run with 448 vertical times 20 horizontal pencilbeams per image. The maximum difference in percent for a simple forward calculation using 10 images and the true atmosphere for a varying number of pencilbeams is depicted in panel (a). Increasing the vertical density of the pencilbeam grid is more important for the accuracy of the model than the horizontal density. This is expected, as the atmosphere changes vertically much faster than horizontally. The largest reduction in error is achieved by switching from 64 vertical pencilbeams to 128 pencilbeams. As the accuracy of the forward model itself is in the order of 1 percent (Hoffmann, 2006), the error involved in using only 128 vertical pencilbeams (0.05 percent) seems acceptable. While the number of horizontal pencilbeams is not very relevant for the absolute value of the radiative transfer, it bears significance for the accuracy of the Jacobian matrix. Panel (b) depicts the standard deviation of the Jacobian matrix in relation to a Jacobian matrix computed using the maximal number of pencilbeams. As the major effect of increasing the horizontal sampling is to "hit" parts of the atmospheric volume, which were otherwise bypassed, the maximum relative error cannot be used for comparison (as it is constantly 100 percent). Weighing accuracy against performance, a value of three was chosen, as increasing the horizontal density further delivers only diminishing returns.

Concluding, a grid with 128 vertical times 3 horizontal pencilbeams is used to simulate the 64 measurements of each image. However, for testing purposes, it is sufficient to use only single pencilbeam per measurement, as the retrieval

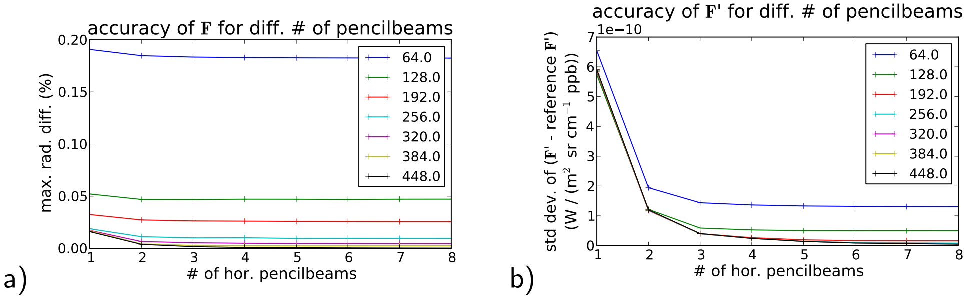

Figure 4.5: The accuracy of $\boldsymbol{F}$ and $\mathbf{F}'$ in relation to the number of pencilbeams used to simulate a single image. Both figures compare in relation to a reference run using a grid of 20 horizontal times 448 vertical pencilbeams. Each coloured line depicts the result for one number of vertical pencilbeams, while the x-axis indicates the number of employed horizontal pencilbeams. Panel **(a)** shows the maximum relative difference between $\boldsymbol{F}$ for the given number of pencilbeams and the reference run. Panel **(b)** indicates the standard deviation of the difference between $\mathbf{F}'$ for the given number of pencilbeams and the reference run. The maximum value of $\mathbf{F}'$ for the reference run is the order of $\approx 4{\cdot}10^{-7}\,\mathrm{W/(m^2\ sr\ cm^{-1} ppb)}$.

result changes only minimally. The diagnostics however exhibit more notable differences, as they are highly dependent on the accuracy of the Jacobian matrix. Please note that even if the grid of pencilbeams employs only a single pencilbeam per measurement (i.e. 64 distinct pencilbeams), each simulated measurement is still generated using the weighted average of multiple pencilbeams.

The presented retrieval for one 3-D volume enclosed by a tomography dedicated flight pattern employs 681 600 pencilbeams to calculate 113 600 simulated radiance measurements distributed on 1 775 images. Each measurement is the weighted average of 72 pencilbeams. It requires ≈21 CPU days, or 2.7 days of real time, on an eight-core machine consuming about 17 GiB of memory total. Thereby more than 95 percent of the computation time is used for calculating the Jacobian matrix by finite differences with tracking (see Sect. 2.2.5), once in the beginning and once for the final step and diagnostics. Additional intermediate updates of the Jacobian matrix are of no benefit for the setup at hand. Using the adjoint method for calculating the Jacobian matrix is expected to reduce the effort for this setup down to less than 1 CPU day, or even less real time when employing some kind of parallelisation. The simplified setup using only 64 pencilbeams per image consumes ≈3 CPU days and 7 GiB of memory. The reduction in computation time is nearly proportional to the reduction of employed pencilbeams. The reduction of memory consumption is largely caused by the sparser Jacobian matrix, which misses many (numerically small to negligible) entries for the simplified setup. In either case, calculating diagnostics is much more expensive than that. The diagnostics for the baseline retrieval presented in the following sections consist of three cutting planes through the 3-D volume with 12 559 data points, which altogether require ≈173 CPU days to calculate. Extrapolating this time, deriving the diagnostic information for the full volume would therefore cost ≈1436 CPU days.

4.3. Tracks following closed curves

In this section, flight tracks closely following the example of computerised tomography in medical science are covered, where a detector performs a full circle around the object of interest. Using the Radon transformation, it can be mathematically proven that the plane, within which the circle lies, can be perfectly reconstructed from the measurements under certain conditions with respect to measurement density and emissions from outside the flight track (Natterer, 2001, p. 9ff). It is therefore expected that this problem is easier to handle than the perhaps more common linear or arbitrary flight tracks dealt with in Sect. 4.4.

4.3.1. Measurement geometry

First, the baseline setup is examined in greater detail. The aircraft is assumed to fly a circle with ≈400 km diameter over the northern parts of France at 15 km altitude. The carrier HALO has a maximum cruising velocity of 0.885 Mach, whereby it will usually fly slower. This study assumes a constant velocity of 850 km/h over ground. Using this speed, flying a full circle needs ≈1.5 h, allowing for 1 775 individual images to be taken at a rate of one image per 3 seconds. The tangent point distribution is depicted in Fig. 4.6. Tangent points are shown as coloured spheres, whereby the colour indicates the time, at which the measurement was taken, starting with blue for the first set of measurements and ending with red for the last. The flight track is shown as white tube. The tangent points form a rotational solid with a distinct waistline and cavities at the top and at the bottom (see Fig. 4.7(b)). The flight altitude and the diameter of the circle determine the shape of the structure. The chosen values generate a tangent point distribution optimally suited for deriving information about the plane at 12 km altitude as the tangent points within that altitude range are evenly distributed without any hole. Such regions with an even distribution of

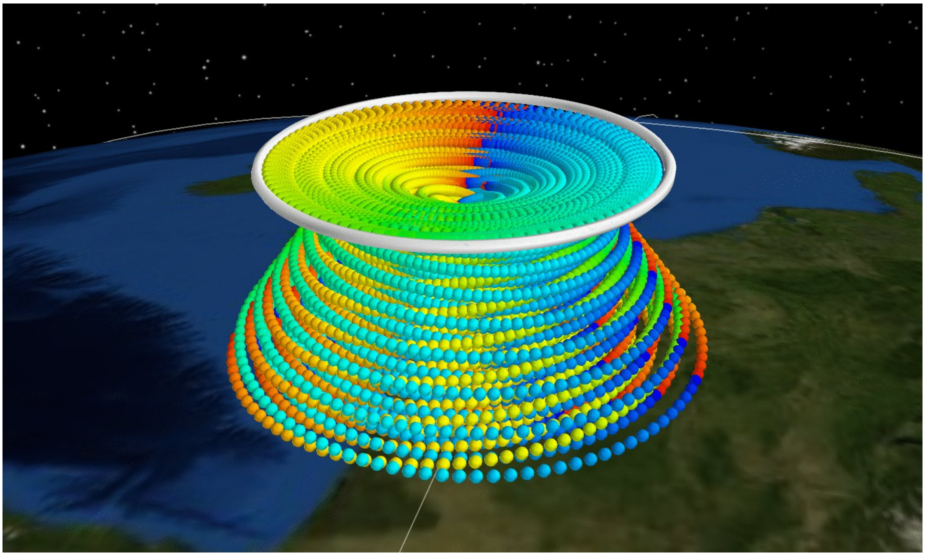

Figure 4.6: The visualisation of a circular flight path. A circular flight path including the location of the tangent points of the measurements as colour-coded spheres (blue being the first measurements, red the last ones) and the flight track as a white tube.

tangent points are expected to deliver the best agreement between the retrieved atmospheric state and the true atmospheric state. Figure 4.7 depicts two cutting planes through the air volume, which is measured by the simulated GLORIA flight. Within the circle described by the flight track, an ozone filament is clearly visible at 12 km height in panel (a), which is the "target" of the retrieval. The tangent points of measurements close to the cutting plane are drawn as small white circles. In the following figures, these circles will be replaced by contour lines indicating the number of tangent points per volume element for better visibility.

4.3.2. Analysis of baseline setup

Figure 4.8 shows the retrieval result for the baseline setup with added instrument noise. Panel (a) shows that the filament is qualitatively well reproduced and panel (b) indicates that the error in the region covered with tangent points is well below ±3 percent. The vertical cutting planes in panels (c) and (d) show good agreement at other heights. The influence of noise on the retrieval result can be seen in comparison with Fig. 4.9, where the same setup is simulated

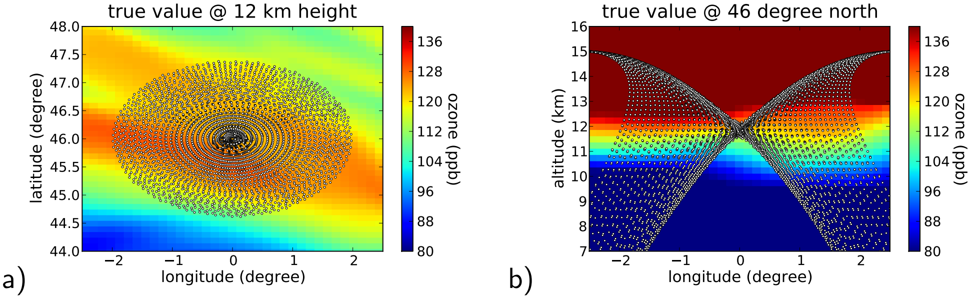

Figure 4.7: Two cutting planes through the full 3-D true atmospheric state. Panel **(a)** shows the ozone filament at 12 km height, while panel **(b)** shows a vertical cutting plane along 46° N. Tangent points close to the cutting planes are shown as small white circles.

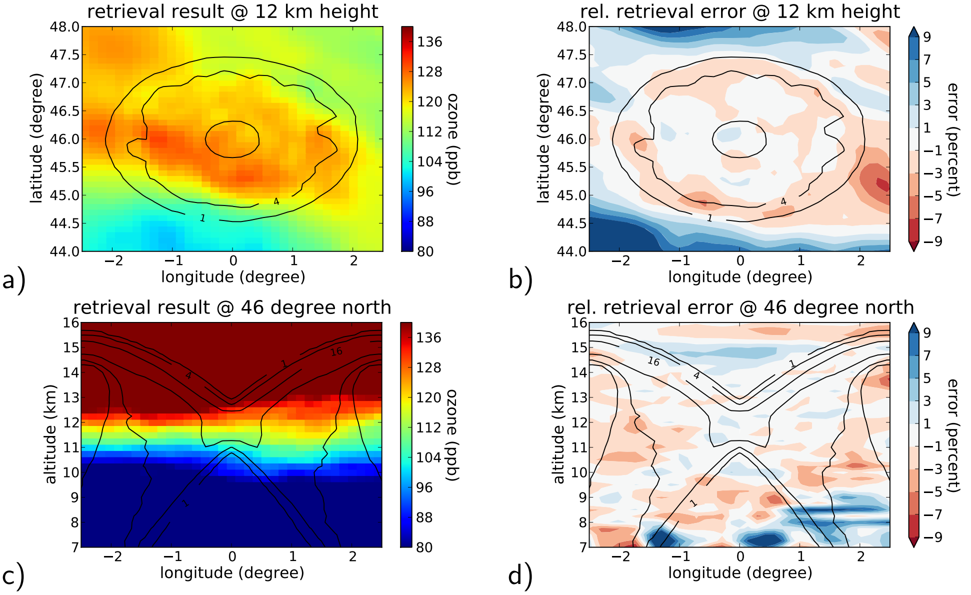

Figure 4.8: The retrieval result of the baseline setup with added instrument noise. Panel **(a)** shows the retrieved ozone values at 12 km height while panel **(b)** depicts the relative error in percent compared to the true values. Panels **(c)** and **(d)** show the same information for a vertical cutting plane at 46° N. The number of tangent points within the depicted volume elements is overlaid as a contour plot with contours at 1, 4, and 16 tangent points.

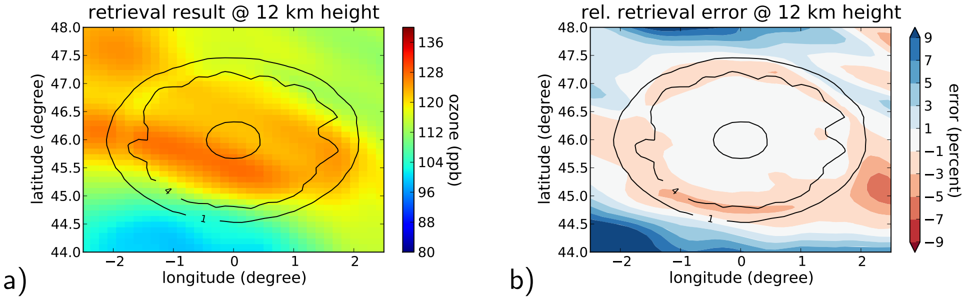

Figure 4.9: The retrieval result of the baseline setup without added instrument noise. Panel **(a)** shows the retrieved ozone values at 12 km height while panel **(b)** depicts the relative error in percent compared to the true values. The number of tangent points within the depicted volume elements is again overlaid as a contour plot.

without added artificial instrument noise. The deviations between the retrieval result and the true value are slightly reduced, but overall relatively unchanged. Most deviations from the true value are not an effect of noise, but of insufficient measurement information, especially in the region outside the flight track.

The given simulation setup has a high measurement contribution close to one within the convex region spanned by the tangent points (not depicted) indicating a negligible bias of the retrieval result towards the a priori vector $\boldsymbol{x}_\mathbf{a}$. The influence of instrument noise at 12 km height is generally less than ≈3 ppb in the region covered by tangent points.

The resolution is determined by calculating the FWHM of the corresponding averaging kernel matrix row in the three spatial dimensions. This is naturally only a meaningful measure, if the volume where the row of the averaging kernel matrix is larger than half its maximum has an approximately ellipsoid shape. This is the case within the region covered by tangent points; outside this region, it usually of an irregular shape, so the resolution cannot be easily expressed with just three numbers. For example, see Fig. 4.10, in which two rows of the 3-D averaging kernel matrix are visualised. The three sides of the cube show cutting planes through the volume spanned by the 3-D averaging kernel matrix row through the data element in question. These allow to quickly gain an insight into the resolution along the three spatial dimensions. The yellow inner contour surface follows the half-maximum of the row, so its extent along the three spatial axes is the measure usually employed by in this work for direction-resolved resolution. The blue outer contour surface follows one tenth of the maximum of the row and gives insight into the volume, from which non-negligible influence

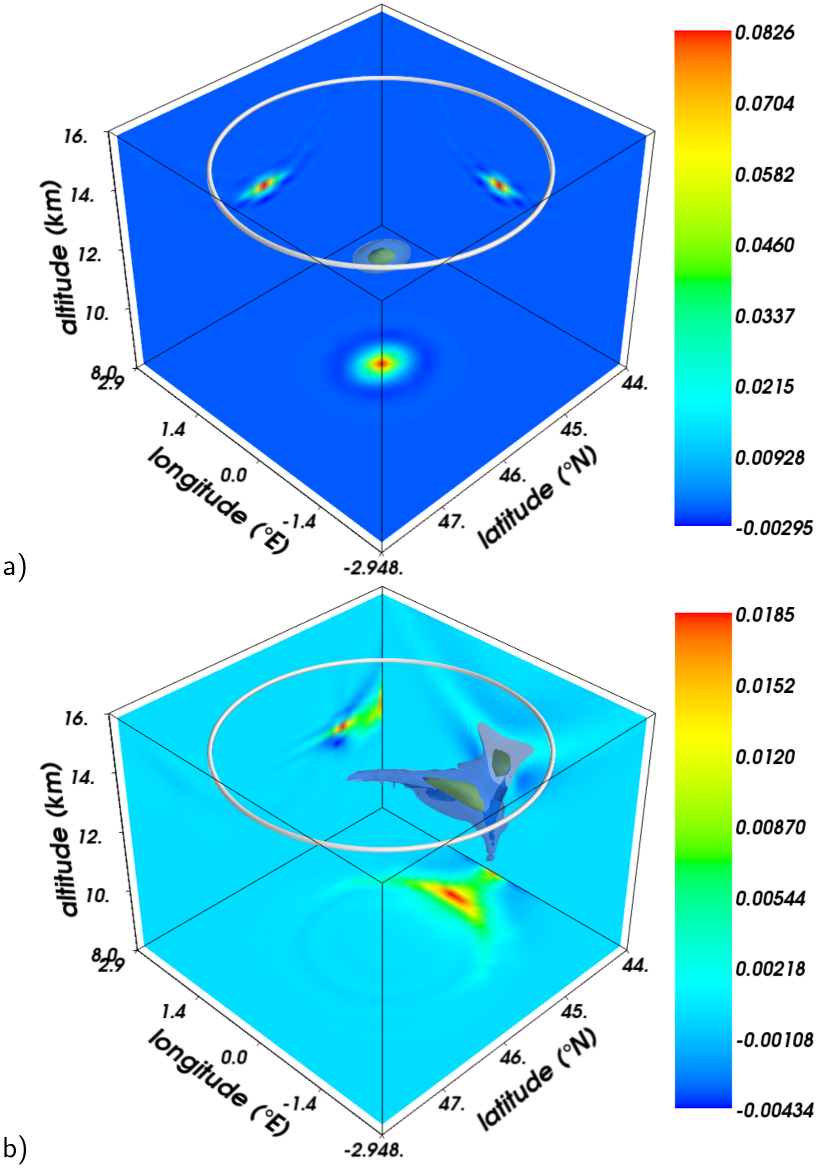

Figure 4.10: 3-D averaging kernel matrix rows for two retrieved ozone values. The inner contour follows the half-maximum of the row. The outer contour follows one tenth of the maximum. The sides of the cube depict cutting planes through the volume described by the 3-D averaging kernel matrix row through the data point. The white tube depicts the flight track. Panel **(a)** shows the row of the 3-D averaging kernel matrix for a pixel in the centre of the volume covered by tangent points (0° E, 46° N, 12 km). Panel **(b)** depicts the row of the 3-D averaging kernel matrix for a pixel slightly outside this region (0° E, 44° N, 12 km).

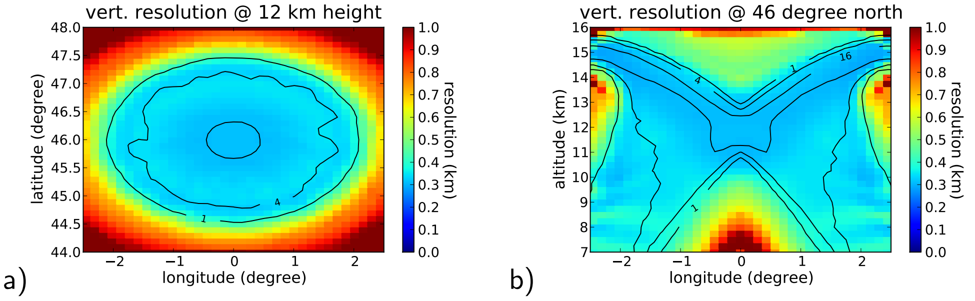

Figure 4.11: The vertical resolution of the baseline setup. Panel **(a)** shows the vertical resolution at 12 km altitude while panel **(b)** depicts the vertical resolution at 46° N. The number of tangent points within the depicted volume elements is overlaid as a contour plot.

is exerted onto the retrieved data element. The shape of the outer contour surface is usually much less well-formed than that of the inner contour surface. In panel (a), the row for the ozone value at 0° E, 46° N, and 12 km height – lying perfectly in the centre – has a well localised ellipsoid shape. In contrast, a point lying well outside the region covered by tangent points at 0° E, 44° N, and 12 km height exhibits two separate maxima in panel (b), one at the location of the point itself, the other around the closest tangent points.

Focusing therefore on the volume covered with tangent points, the vertical resolution is ≈325 m at 12 km height as is shown in Fig. 4.11. Simulations with a finer retrieval height grid of only 125 m and 128 distinct vertical measurements per image (not depicted) indicate that a vertical resolution of ≈200 m seems feasible, which would be a boon for the close examination of vertically thin structures like the tropopause inversion layer (Birner et al., 2006). In panel (b), the achievable vertical resolution in the "tangent point holes" at the bottom and at the top of the analysed volume increases rapidly due to a lack of measurements. This suggests that the radius of the flown circle and the altitude of the aircraft, which together determine the height region with best tangent point coverage, should be chosen according to the height region one is most interested in.

The horizontal resolution in longitudinal direction in Fig. 4.12(a) is between 20 km to 30 km indicating that the retrieval grid is fine enough to not limit the achievable horizontal resolution. The low values at the upper and lower part of Fig. 4.12(a) result from the fact that the shape of the rows of the averaging kernel matrix in this region deteriorates from a roughly ellipsoid shape towards more irregular shapes, which extend roughly in north-south direction. Corre-

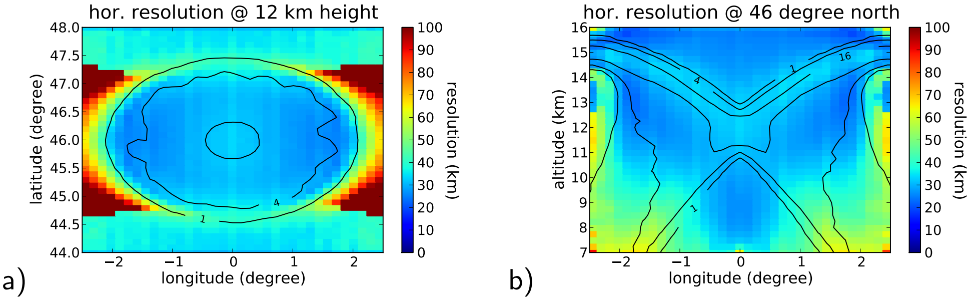

Figure 4.12: The horizontal resolution in longitudinal direction of the baseline setup. Panel **(a)** shows the horizontal resolution at 12 km altitude while panel **(b)** depicts the horizontal resolution at 46° N. The number of tangent points within the volume element is overlaid as a contour plot.

spondingly, the horizontal resolution in latitudinal direction is quite similar to that in longitudinal direction within the region covered by tangent points, but increases rapidly towards the north and south and is deceivingly low towards the east and west. Figure 4.12(b) indicates that the horizontal resolution is best in the middle of the volume, where the air volume is seen from most angles. Towards the borders, especially to the lower left and lower right, the coverage decreases and therewith also the horizontal resolution. By tuning the regularisation parameters (not depicted), it is possible to shift information between vertical resolution, horizontal resolution and measurement noise.

Concluding, the 3-D tomographic retrieval offers a core volume spanning 5 km in the vertical direction and 400 km diameter in the horizontal direction with a resolution better than 500 m in the vertical and 30 km in the horizontal. Although it is certainly beneficial to know beforehand, where an interesting atmospheric structure might appear, the well-resolved volume offered by the tomographic retrieval is large enough to require only a rough idea where a structure of interest might be located.

4.3.3. Choice of regularisation strength

In this section, the exact choice of regularisation parameters is established. An exhaustive study of the regularisation parameters has been performed to find the proper regularisation strength. The free parameters are

- α_0, which determines the strength of zeroth order regularisation, thereby keeping the absolute values of the retrieval result close to the a priori,

- α_1^z, which determines the strength of first order regularisation in vertical direction, thereby keeping the vertical variation of the retrieval result smooth, and
- α_1^x and α_1^y, which determine the strength of first order regularisation in horizontal direction, thereby keeping the horizontal variation of the retrieval result smooth.

For simplicity's sake, α_1^x and α_1^y are kept identical, even though one could argue that meridional and zonal variation in the atmosphere are different. The parameter study revealed that $\alpha_0 = 0$ and $\alpha_1^z = 0\,\mathrm{km/ppb}$ deliver just as good results for the volume covered by tangent points as the finally selected values of $\alpha_0 = 0.1$ and $\alpha_1^z = 4 \cdot 10^{-4}\,\mathrm{km/ppb}$. A positive value for α_0 was mainly chosen to ensure the regularity of $\mathbf{S}_\mathbf{a}^{-1}$. In this mindset, the value of α_0 was chosen as large as possible without noticeably reducing the measurement contribution below one. The value for α_1^z has been selected to be too small to influence the result within the volume covered by tangent points, but is still large enough to exert influence on the volume above.

Figure 4.13 compares the relative error of the baseline setup with the error of retrievals employing different regularisation strengths. Panel (a) shows a vertical cutting plane through the result of the baseline setup for comparison. Next to it, the effect of a decrease in vertical regularisation strength is shown in panel (b). The retrieval error remains nearly unchanged compared to the baseline regularisation shown in panel (a) except for the altitude range above 15 km (the observer altitude). In this high altitude range, the relative error changes from a rather consistent $\approx$+3 % to alternating between -9% and $+9\%$. All upwards pointing observations receive most of their radiation from the observer altitude, as the atmosphere is densest at this point along their LOS. This implies that insufficient measurement information is present above the observer altitude to fully determine the atmospheric state without using a priori information. The smoothing influence of vertical regularisation can partially compensate for this lack of information about higher altitudes. Increasing the vertical regularisation strength to higher values than used in the baseline regularisation does not improve the retrieval result, but eventually worsens it due to over-smoothing below 15 km.

The horizontal regularisation strength was chosen to give a “visually pleasing” retrieval result. For example, in Fig. 4.13, three different horizontal regularisation strengths are compared by means of error plots for the result. On the lower left, in panel (c) a lower horizontal regularisation strength is shown, which is

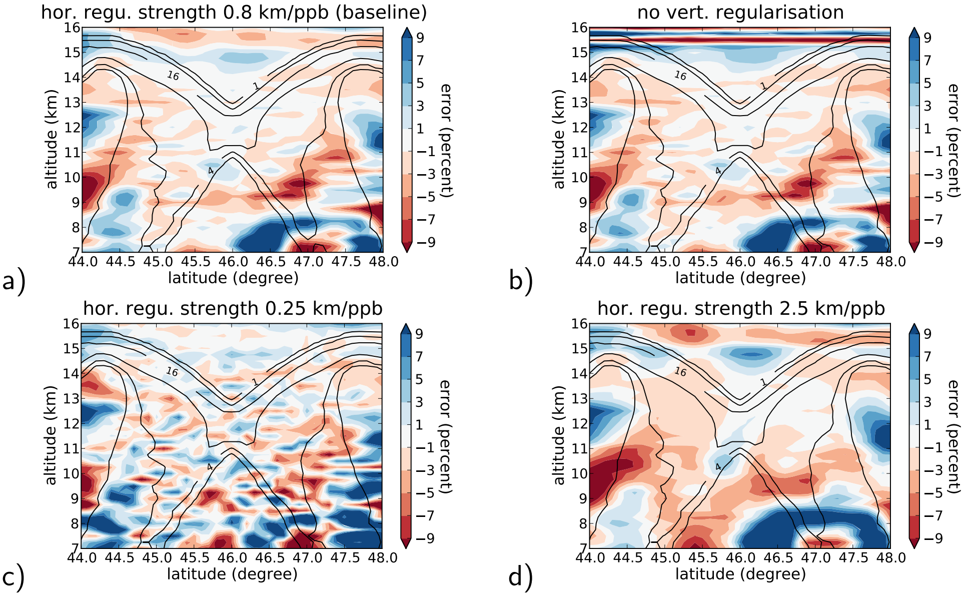

Figure 4.13: The effect of different regularisation strengths. Panel **(a)** shows the baseline setup for comparison with a horizontal regularisation strength of 0.8 km/ppb. Panel **(b)** shows the result of a non-linear retrieval using no vertical regularisation of first order. Panel **(c)** shows the result for a reduced horizontal regularisation strength of 0.25 km/ppb. Panel **(d)** shows an increased horizontal regularisation strength of 2.5 km/ppb. The number of tangent points within the depicted volume elements is overlaid as a contour plot.

arguably very noisy, especially in lower altitudes. Closely spaced regions alternate between positive and negative relative errors. In panel (d) a stronger horizontal regularisation than employed in the baseline setup is depicted. Here, the relative error remains constant over large volumes, which indicates a bias, as the smoothing prevents the retrieval result from following the variations of the true atmospheric state. In panel (a) the baseline strength is shown; regions of constant error are not as small as in panel (c) and also the absolute value of the occurring relative errors is generally smaller. Compared to panel (d), the region of less than ±1% error is quite a bit larger. The distribution between positive and negative errors seems also to be a bit more balanced, implying that the result is subject to a smaller overall bias. Summarising, panel (a) looks more visually pleasing.

However, as the visual inspection is a very subjective measure, the L-curve optimality criterion was employed in addition as an objective method. The L-curve method, which was popularised by Hansen (1992), has the further advantage of not requiring the true state of the atmosphere for determining the regularisation strength and is therefore also suitable for retrievals using real measurements. The L-curve criterion can optimise only a single parameter determining the overall strength of the regularisation. This parameter, $\omega > 0$, needs to be added to the cost function resulting in

$$J(\boldsymbol{x}) = (\boldsymbol{F}(\boldsymbol{x}) - \boldsymbol{y})^{\mathrm{T}} \mathbf{S}_{\epsilon}^{-1} (\boldsymbol{F}(\boldsymbol{x}) - \boldsymbol{y}) + \omega \cdot (\boldsymbol{x} - \boldsymbol{x}_{\mathbf{a}})^{\mathrm{T}} \mathbf{S}_{\mathbf{a}}^{-1} (\boldsymbol{x} - \boldsymbol{x}_{\mathbf{a}}). \tag{4.1}$$

Varying the overall regularisation strength ω delivers different results, as the regularising constraint changes from being negligible ($\omega \to 0$) to being determining ($\omega \to \infty$). Plotting the residual $(\boldsymbol{F}(\boldsymbol{x}) - \boldsymbol{y})^{\mathrm{T}} \mathbf{S}_{\epsilon}^{-1} (\boldsymbol{F}(\boldsymbol{x}) - \boldsymbol{y})$ against the constraint $(\boldsymbol{x} - \boldsymbol{x}_{\mathbf{a}})^{\mathrm{T}} \mathbf{S}_{\mathbf{a}}^{-1} (\boldsymbol{x} - \boldsymbol{x}_{\mathbf{a}})$ for a wide range of ω yields for many inverse problems an empirically observed L-shaped curve. For small ω, the solutions are unstable as they are determined almost entirely by fitting the measurements. This leads in most cases to heavy oscillations in the solution due to the amplification of experimental error. On the other hand, for large ω, the solutions are mainly determined by the constraint, implying that they are over-smoothed or biased towards the a priori vector depending on the nature of the employed regularisation. The corner of the L-curve represents a good balance between fidelity to the measurements and smoothing due to the constraint. The corner may be identified mathematically, for instance by identifying the point with the largest curvature (Hansen and O'Leary, 1993).

Fixing α_0, α_1^x, α_1^y, and α_1^z to the baseline values, the ω was varied over a wide range in a parameter study. Thus, if the baseline regularisation strength is L-curve optimal, the corner of the L-curve is expected around a value of $\omega = 1$. The resulting L-curve is plotted in log-log scale, believed to emphasise the corner, in Fig. 4.14. The corner is indeed close to the point for $\omega = 1$, erring slightly towards emphasising the fit of measurements. The point annotated with "1.00" corresponds to the baseline regularisation strength, while the point annotated with "10.00" uses $10 \cdot \mathbf{S}_{\mathbf{a}}^{-1}$ as regularisation matrix. Several retrievals have been annotated in this way to give an indication for the correlation between overall regularisation strength and fit. The annotated point on the curve with "10.0" corresponds roughly to the retrieval depicted in Fig. 4.13(c), and the one with the value "0.1" corresponds roughly to Fig. 4.13(d) (for generating Fig. 4.13, only the horizontal regularisation strength was adapted, while for generating the L-curve also the other regularisation components were modified). Only changes of the regularisation strength by orders of magnitude have a significant influence.

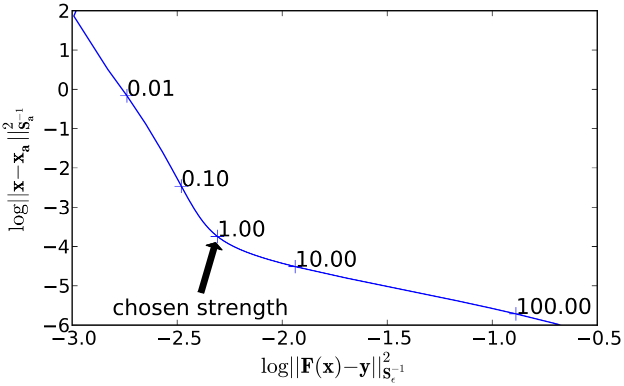

Figure 4.14: The L-curve for the baseline setup. It has been normalised so that a value of “1.00” corresponds to the baseline regularisation strength with matrix $\mathbf{S_a}^{-1}$. A value of “10.00” means that $10 \cdot \mathbf{S_a}^{-1}$ was used instead. Some exemplary retrievals have been annotated to give a feeling for the correlation between overall strength and fit.

The baseline regularisation seems to be adequate for the problem at hand, as both increasing and decreasing its strength increases the relative error of the retrieval result. Further, the chosen strength is also optimal according to the L-curve criterion. This suggests that the L-curve criterion delivers a useful regularisation strength for tomographic retrievals and should therefore be used for determining the regularisation strength for retrievals of actual measurements, where the true state of the atmosphere is unavailable for comparison.

4.3.4. Effect of panning

An innovative new feature of GLORIA is the ability to point the instrument in different horizontal directions without changing the flight direction of the aircraft itself. The effect of this panning on the 3-D tomographic reconstruction is examined by varying the maximum available panning angle in numerical simulations. The intent is to quantify how panning benefits the retrieval result. The baseline setup described in Sect. 4.3.2 uses the full GLORIA panning capability by moving the detector by 4° between taking two images and going back to 45° after an angle of 133° has been reached. Figure 4.15 shows an exemplary retrieval without any panning, fixing the instrument viewing direction to 90° like a conventional instrument would measure. The strength of the regularisation has

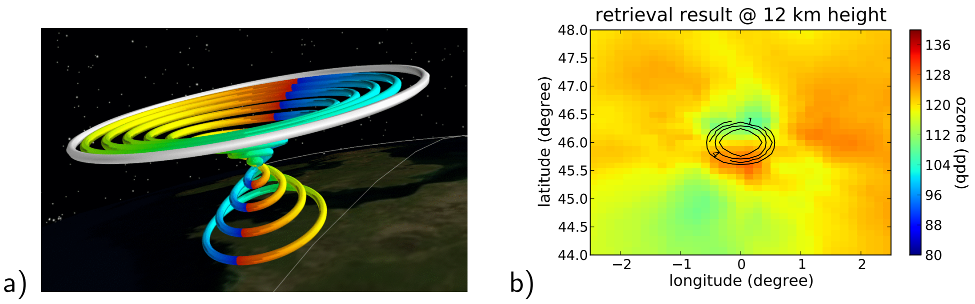

Figure 4.15: A tomographic retrieval without panning. Panel **(a)** shows the location of the tangent points of the measurements as colour-coded spheres (red being the first measurements, blue the last ones) and the flight track as white tube. Panel **(b)** shows the retrieval result at 12 km height. The number of tangent points within the depicted volume elements is overlaid as a contour plot.

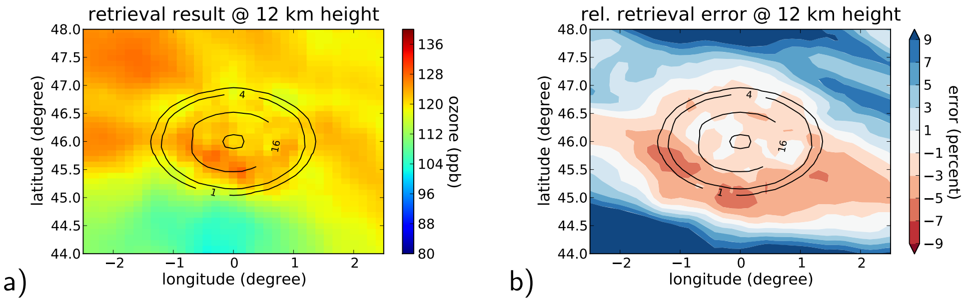

Figure 4.16: The retrieval result **(a)** and relative error **(b)** of a tomographic reconstruction with panning being reduced to a span of 50°. The number of tangent points within the depicted volume elements is overlaid as a contour plot.

not been changed from the baseline setup to retain comparability of the results. The tangent points of measurements in panel (a) do not span a volume but are located on a 2-D surface in space. Consequently, the retrieval does not deliver a good representation of the true atmosphere, which could not be significantly improved by tuning the regularisation (not depicted). Panel (b) depicts the retrieved atmospheric state. It seems difficult to discern the original filament from this data as the relative error exceeds −10 % even close to the tangent points in the middle.

Better results can be achieved with a reduced panning in contrast to no panning at all. Figure 4.16 depicts a retrieval setup, in which the panning is reduced to the range from 65° to 115° relative to the flight direction. Also for this setup, the filament is quite difficult to discern, as the errors are systematically larger than for the setup with full panning capability. The simulations indicate that the results improve the wider the angle gets, with an optimum close to the angle available for GLORIA. Extending the fan further (not depicted), more rays pass through air volumes that are not viewed from multiple angles and are therefore difficult to resolve three-dimensionally. In addition, these rays are missing on the inside of the flight path, reducing the retrieval quality there.

A second consideration must be given to the panning step size. While the simulations do not indicate that the result is overly sensitive to the step size as long as it is below ≈30°, the result improves the more evenly distributed the tangent points of the individual measurements are. Reducing the step size increases the number of tangent point "circles", but reduces the number of points on the "circle". For the dynamics mode, a natural step size of 4° seems optimal for the setup at hand, while for the chemistry mode, which requires longer time to acquire a single measurement, a larger step size might be chosen.

In summary, the ability to pan the instrument is clearly an invaluable asset for tomographic reconstruction.

4.3.5. Choice and effect of flight track

The choice of flight track is of large importance for 3-D tomographic retrievals. Closed or nearly closed paths seem to be able to provide a good reconstruction of the true atmospheric state, similar to computer tomography. The true atmospheric state was only reproduced accurately by numerical simulations in those parts of the volume, where the tangent points of measurements are located. A perfectly circular flight path gives the most regular distribution of tangent points as presented in Sect. 4.2. As such a flight path may not be feasible for practical concerns, it is discussed in the following how approximations to the circular track behave.

Two such approximations are exemplarily presented: a square flight track and an octagonal flight track. Figure 4.17 depicts a simple square track in the same style as Fig. 4.6. The area below the corners of the square is devoid of measurements while there are large extensions below the sides of the square (the latter ones could be avoided by influencing the panning in a more complicated way than employed here). Figure 4.17(b) shows the relative error of the retrieval result for this flight path at 12 km height. The relative error is small where tangent points are located, but the corners – being devoid of tangent points – are already quite erroneous. Calculating horizontal resolution (not depicted)

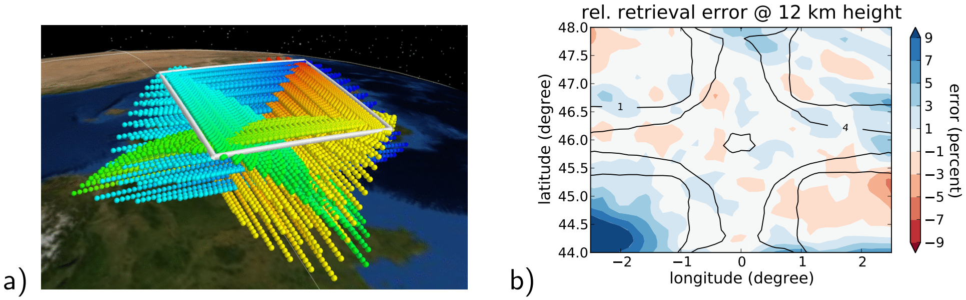

Figure 4.17: Visualisation of a square flight path and relative retrieval error. Panel **(a)** shows the location of the tangent points of the measurements as colour-coded spheres (red being the first measurements, blue the last ones) and the flight track as white tube. Panel **(b)** shows the relative error of the retrieval result at 12 km height. The number of tangent points within the depicted volume elements is overlaid as a contour plot.

indicates that the values in the corners are almost entirely derived by horizontal smoothing. Figure 4.18 shows in comparison an octagonal flight path, which resembles a circular track more closely. Panel (a) depicts again the location of tangent points in space and time and panel (b) shows the relative error of the retrieval result at 12 km altitude. The area covered by tangent points is larger, corresponding to a larger area of good reconstruction. This flight track seems to be a good compromise, as a larger area is covered by tangent points so that the ozone filament is even better reproduced than in Fig. 4.8(a). However the horizontal resolution is generally slightly worse than for the baseline setup.

Both presented approximations to a circular flight track seem usable and could possibly be optimised further, for instance by adjusting the panning. Thus, it is expected that a workable flight track can be found for campaigns given typical restrictions imposed by aerospace regulations and scientific goals.

4.3.6. Comparison with individual 1-D retrievals

The 3-D tomographic retrieval is more robust in the presence of horizontal inhomogeneity than conventional 1-D retrievals. In this section, it is demonstrated that the employed test case is indeed a difficult one for conventional retrievals due to the horizontal inhomogeneity of ozone. Second, a method is developed to quantify the effect of horizontal inhomogeneity on 1-D retrievals based upon the assumption of a horizontally stratified atmosphere.

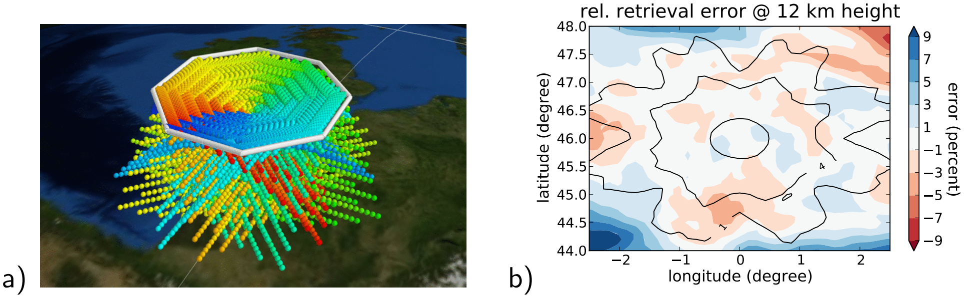

Figure 4.18: Visualisation of an octagonal flight path and relative retrieval error. Panel **(a)** shows the location of the tangent points of the measurements as colour-coded spheres (red being the first measurements, blue the last ones) and the flight track as white tube. Panel **(b)** shows the relative error of the retrieval result at 12 km height. The number of tangent points within the depicted volume elements is overlaid as a contour plot.

To compare the tomographic approach with conventional retrievals, each individual image of the baseline setup was used to perform a single 1-D retrieval. To exclude secondary representation effects, only ozone within the retrieval height range was kept three-dimensionally varying; all other quantities were made horizontally homogeneous. The 1-D retrievals seem to require a stronger vertical regularisation (i.e. $\alpha_1^z = 4{\cdot}10^6$) as the regularising influence of the horizontal smoothing is missing. Figure 4.19 depicts as an example the results of the 1-D retrievals at 12 km height with the true atmosphere as background. Ozone is both severely under- or overestimated depending on the pointing of the GLORIA instrument. Profiles underestimating ozone are generally derived from images pointing northwards and profiles overestimating it are generally pointing southwards. Increasing the strength of the vertical smoothing further, the noisiness of the results decreases at the cost of a worsening vertical resolution. However, the systematic under- and overestimation is unaffected by a stronger or weaker regularisation.

To gain deeper insight into the cause of these systematic errors, a single retrieval that underestimates ozone by ≈20 % was selected for analysis, which is indicated by a broad black circle in Fig. 4.19. Figure 4.20 shows the individual rays of the corresponding image together with the ozone values along the LOSs. To compensate for the strong vertical gradient of ozone, the values have been horizontally normalised to the ozone concentration at the line connecting the tangent point locations and going straight up from the observer location at 15 km. Above 10 km altitude, one can see a strong horizontal structure with

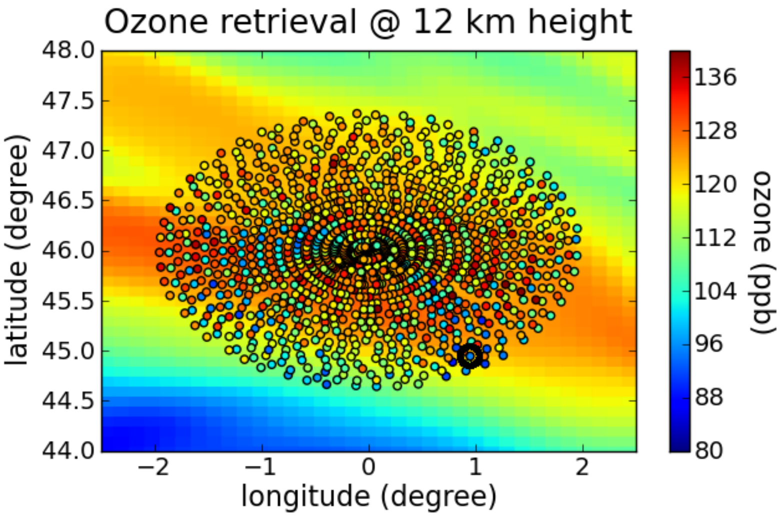

Figure 4.19: The retrieval result for 12 km height of 1-D retrievals. The result of each retrieval is shown as colour-coded circle placed at the horizontal location of the closest tangent point. The data point highlighted by a broad black circle has been selected for closer examination. The background shows the true state of the atmosphere.

ozone concentrations decreasing away from the instrument. Figure 4.21(b) shows the row of the 1-D averaging kernel matrix corresponding to the value at 12 km. The broadness of the function shows the expected vertical averaging, but this is not the reason for the underestimation, as the ozone concentrations at, above, and below 12 km are quite similar. Therefore, the 1-D diagnostics do not give any indication for the severe underestimation of ozone concentration.

The usual 1-D diagnostics cannot capture the effect of 2-D atmospheric structures on the retrieval result as the diagnostics also depend on the notion of a horizontally homogeneous atmosphere. A mapping (that is a linearised retrieval) of the true – in this case – 2-D atmosphere onto the 1-D result is required to gain further insight into the problem. Such a map can be generated by using the 1-D gain matrix shown in Fig. 4.21(a) and a 2-D Jacobian matrix describing the sensitivity of the measurements to a 2-D atmosphere along the LOS. A 2-D Jacobian matrix can be generated by creating a 2-D atmosphere, filling it with the true state of the atmosphere along the LOS, and calculating the derivatives. The 2-D atmosphere employed here uses the same altitude grid as the 1-D representation and a regular horizontal grid with a 5 km horizontal spacing. Now, the 1-D gain matrix can be multiplied with the 2-D Jacobian matrix to create a

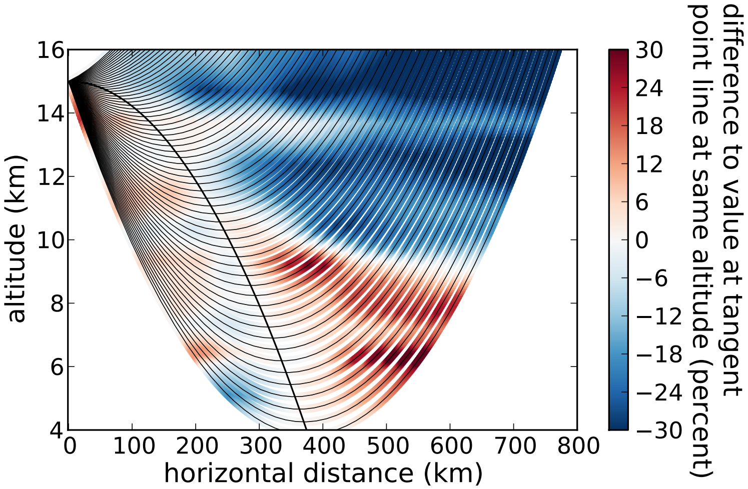

Figure 4.20: The rays of an exemplary 1-D retrieval. The ozone values are depicted relative to the value at the line of tangent points. The tangent points are shown as bold line starting from the instrument to the left and arcing down towards the ground.

new averaging kernel matrix that maps the true 2-D state of the atmosphere to the 1-D retrieval result. This is quite similar to the way that the usual averaging kernel matrix is calculated, the only difference being the exchange of the 1-D Jacobian matrix by the 2-D Jacobian matrix. The resulting matrix is referred to by this thesis as 2-D/1-D averaging kernel matrix and is shown in Fig. 4.22(b). A similar technique was used by von Clarmann et al. (2009) to estimate the horizontal resolution of the MIPAS instrument.

The 2-D/1-D averaging kernel matrix is closely related to the usual 1-D averaging kernel matrix. For instance, the 2-D/1-D averaging kernel matrix can be transformed into the 1-D averaging kernel matrix by summing up and combining all elements of each row belonging to the same altitude. Consequently, the horizontal oscillations above 12 km in Fig. 4.22(b) sum up horizontally to (nearly) zero. If there were a horizontally homogeneous ozone concentration at higher altitudes, these oscillations would not affect the retrieval result, just as the 1-D averaging kernel matrix suggests. However, there is a strong gradient, which is folded with the oscillations visible in the 2-D/1-D averaging kernel matrix and thereby contributes noticeably to the retrieval result at 12 km altitude.

The observed horizontal oscillations in the 2-D/1-D averaging kernel matrix are the consequence of the averaging kernel matrix **A** being a linear combination

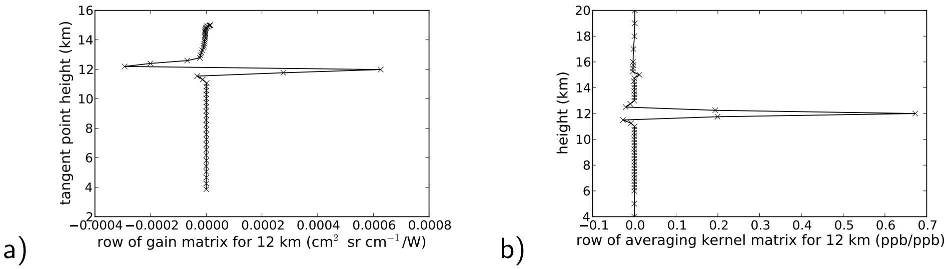

Figure 4.21: The rows of gain and averaging kernel matrices for 12 km altitude. Panel **(a)** shows the row of the gain matrix corresponding to the retrieval result at 12 km. Panel **(b)** shows the row of the 1-D averaging kernel matrix describing the relationship between a “true” 1-D atmosphere and the 1-D retrieval result at 12 km.

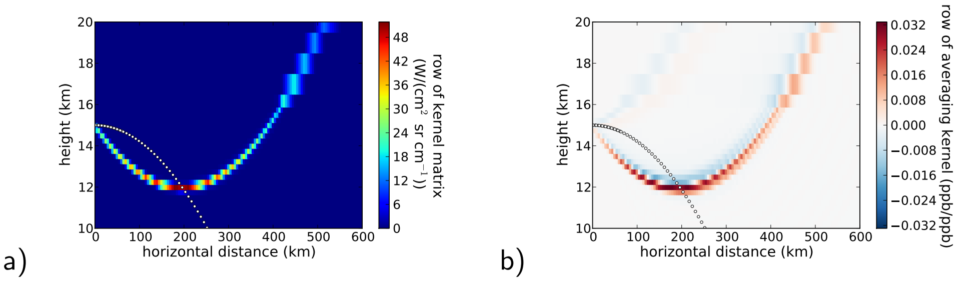

Figure 4.22: The effect of the assumption of horizontal homogeneity on a single 1-D retrieval. Panel **(a)** shows the 2-D weighting function with tangent height closest to 12 km. The 1-D weighting function corresponds to the horizontal sum of this matrix. Panel **(b)** depicts the row associated with 12 km retrieval height of the 2-D/1-D averaging kernel matrix and shows the contributions of higher layers to the retrieval result.

($\mathbf{A} = \mathbf{G}\mathbf{F}'(\hat{\mathbf{x}})$) of the rows of the Jacobian matrix, that is the weighting functions. Figure 4.21(a) shows a row of the gain matrix; it depicts the coefficients used to add up the rows of the Jacobian matrix to generate the row of the averaging kernel matrix for 12 km altitude. It is foremost a weighted average of the measurements with tangent points close to 12 km. Figure 4.22(a) shows one row of the 2-D Jacobian matrix, that is a 2-D weighting function describing the sensitivity of one measurement with tangent point altitude close to 12 km altitude to changes of the 2-D atmosphere. Its maximum sensitivity lies close to the tangent point, but significant contributions are also present at higher altitudes. The negative entries in Fig. 4.21(a) remove these contributions in the 1-D averaging kernel matrix. By ignoring the horizontal dimension, the 1-D weighting functions can be combined to closely approximate the delta function as shown in Fig. 4.21(b). However, if the more accurate 2-D Jacobian matrix is used instead, it becomes obvious that the available measurements do not in fact allow such a good spatial localisation if the atmosphere is not horizontally homogeneous.

It is now clear, what causes the ≈ 20 percent underestimation in the case at hand. The horizontal oscillations of the 2-D/1-D averaging kernel matrix in combination with a steep gradient in the ozone concentration cause this underestimation. The effect is especially pronounced as ozone concentrations increase with height. Therefore small oscillations in the 2-D/1-D averaging kernel far above the retrieved value still contribute meaningfully to the retrieval result. The effect should be less pronounced for trace gas species that remain approximately constant or decrease in concentration with altitude. The same problem has affected the evaluation of MIPAS measurements as demonstrated by Kiefer et al. (2010). Naturally, the oscillations within the 2-D/1-D averaging kernel matrix at higher altitudes contribute only noticeably to the result, if the trace gas concentrations are in fact horizontally inhomogeneous.

In contrast, the 3-D retrieval can evaluate more measurements and thereby use more information in the construction of the averaging kernel matrix. This increases the vector space spanned by the weighting functions and thereby offers better approximations to the desired delta functions.

The described technique can also be used to more reliably compare 3-D model data with retrieved 1-D profiles by folding the model data with the 2-D/1-D averaging kernel matrix instead of the usual 1-D averaging kernel matrix. The method can also be used to quantify the effect of the horizontal inhomogeneity on 1-D retrieval results and thereby, in combination with a chemical weather forecast, help identify problematic atmospheric situations and accordingly optimise flight-paths of air-borne instruments to avoid a bias in the retrieval results.

4.4. Linear flight tracks

In this section, 3-D tomographic retrievals are discussed that use simulated GLORIA measurements made while following a linear flight track. As the GLORIA instrument will generally share the carrier with other instruments subject to different requirements, the flight track may often be quite different from a closed curve. The simplest shape probably always present within a flight track is a straight line. Consequently, this section analyses the potential of a linear flight track in the same atmospheric situation as described in Sect. 4.2.

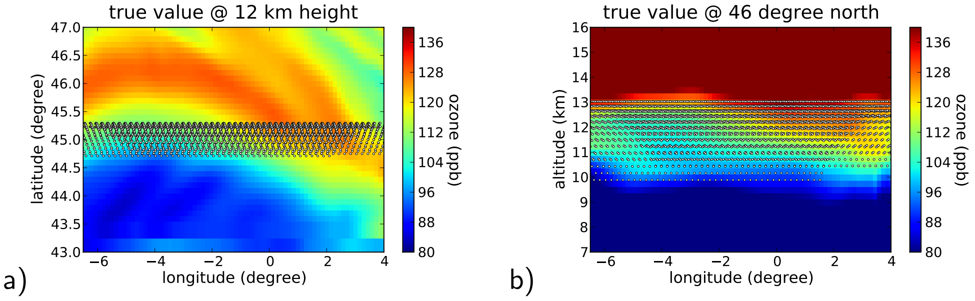

Figure 4.23: The atmospheric situation and measurement geometry of the linear flight track numerical experiment. Panel **(a)** shows the true atmospheric state and the location of the tangent points at 12 km altitude. Panel **(b)** depicts the same for a vertical cutting plane at 46° N. The location of tangent points close to the depicted volume elements is indicated by small white circles.

In this numerical experiment, the plane starts its flight at 6.5° E at 43.5° N and continues from there along the circle of latitude until 4.0° W. This flight track of 840 km length gives ≈600 km of air that can be viewed with the instrument pointing both forward and backward. The flight track has been placed so that the volume covered by tangent points is located at the boundary of the filament. The intent is naturally to reproduce the boundary, which poses a steep gradient in across track direction. Figure 4.23 shows the tangent point coverage.

4.4.1. Analysis of linear flight track

Using the same regularisation and panning as in the baseline setup, a retrieval delivers the result depicted in Fig. 4.24. The relative error is overall much larger than for the circular setup, but stays below 5 percent in the region covered by tangent points. The covered region is qualitatively and quantitatively well reproduced. Values further to the north and south stem largely from smoothing and extrapolation and should be disregarded or at least used with caution.

Figure 4.25 shows the horizontal resolution in longitude and latitude directions as deduced by the usual method. Due to the irregular shape of the rows of the averaging kernel matrix, only the values within the region covered by tangent points are reliable. The achievable resolution in latitudinal direction in panel (a) is in the order of 30 km and is largely determined by the strength of the horizontal regularisation in this direction. The resolution in longitudinal direction in panel (b) is about 50 km, which is much smaller than the 100 to 200 km that are usual for 1-D retrievals. Vertically, this retrieval exhibits a

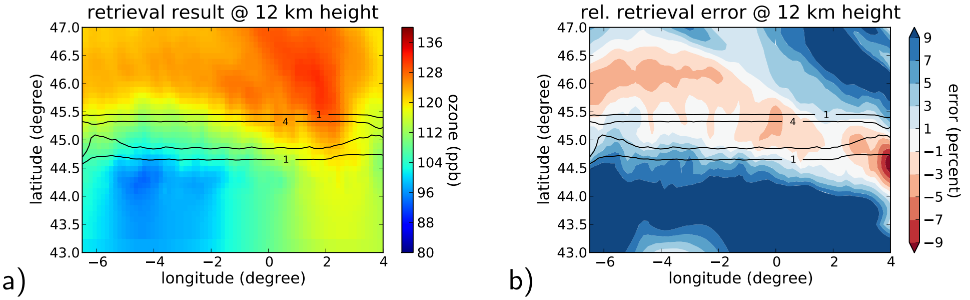

Figure 4.24: The retrieval result for a linear flight track. Panel **(a)** shows how the gradient of the ozone filament is well reproduced, where measurement information is available. The relative retrieval error plot in panel **(b)** asserts this. The number of tangent points within the depicted volume elements is overlaid as a contour plot.

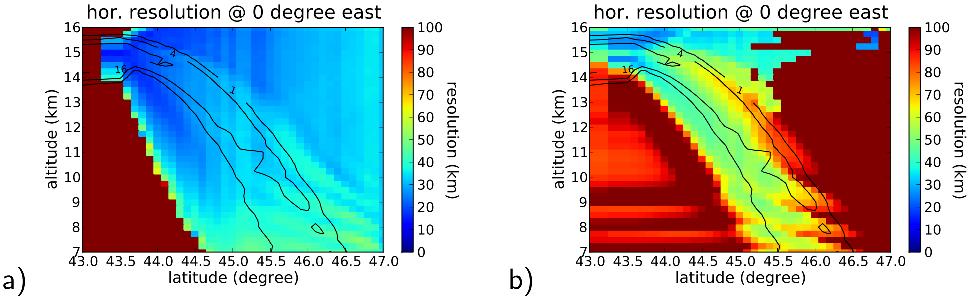

Figure 4.25: The horizontal resolution for a linear flight track. Panel **(a)** gives the horizontal resolution in along track direction (latitudinal), while panel **(b)** gives the horizontal resolution in across track direction (longitudinal). The number of tangent points within the depicted volume elements is overlaid as a contour plot.

resolution of ≈300 m in the volume covered by tangent points, similar to the baseline retrieval.

Reliably determining the resolution is more difficult for this setup as the rows of the averaging kernel are of a more irregular shape than in the baseline setup. Looking at the 3-D averaging kernel matrix gives more insight than the high-level resolution figures. Figure 4.26(a) depicts a row of the averaging kernel matrix belonging to an element in the centre of the region covered by tangent points. The information is well localised with a noticeable smoothing in meridional direction. Figure 4.26(b) depicts the row of the averaging kernel matrix of a data element northwards of the well resolved area. Typically for those elements lying outside the region covered by tangent points, it is strongly influ-

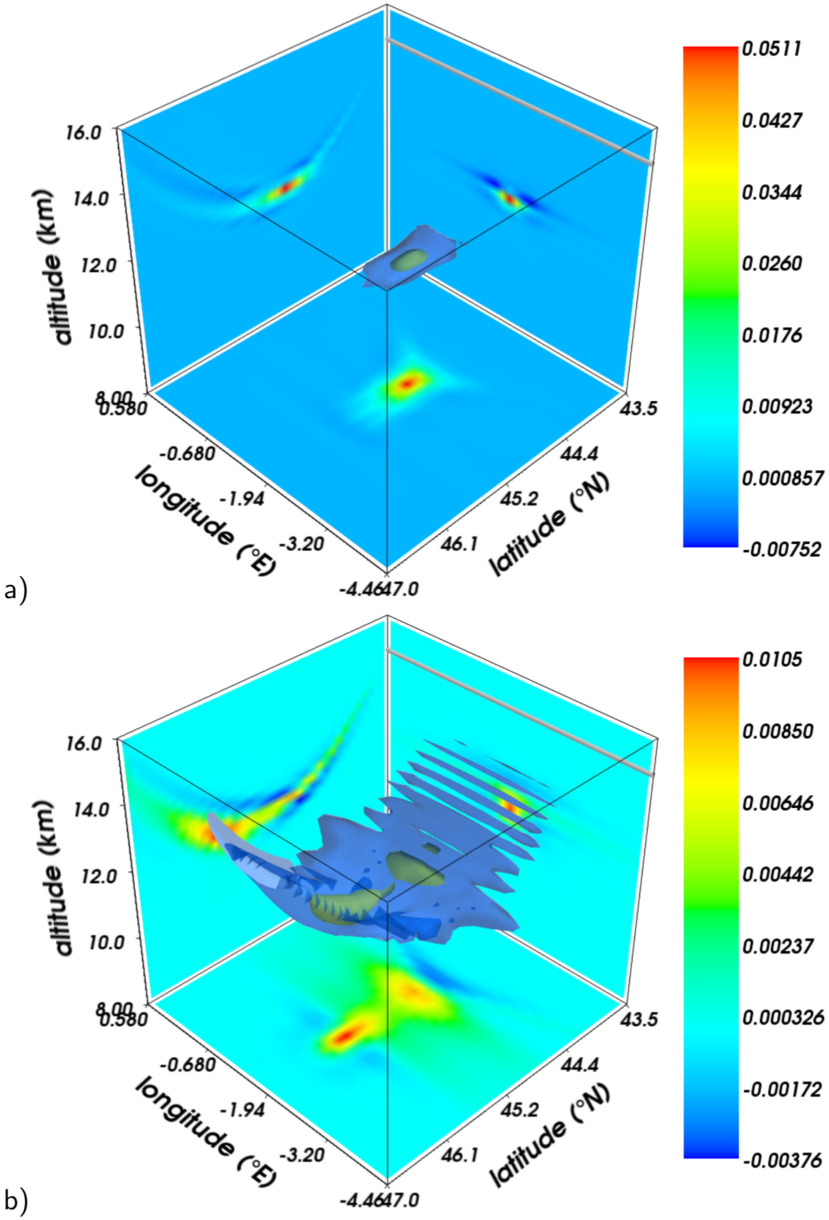

Figure 4.26: 3-D averaging kernel matrix rows for two retrieved ozone values for the linear flight track. Panel **(a)** shows the row of the 3-D averaging kernel matrix for a pixel in the centre of the volume covered by tangent points (2.02° W, 45° N, 12 km altitude). Panel **(b)** depicts the row of the 3-D averaging kernel matrix for a pixel slightly outside this region 110 km towards north (2.02° W, 46° N, 12 km altitude).

enced by both the closest tangent points as also the volume around its location. For all LOSs touching this data element, the tangent point lies between the element and the instrument. As the atmosphere is not fully transparent at this altitude and spectral range, the sensitivity of the measurements is already quite reduced before it “hits” the point. In contrast, the volume lying between the instrument and the tangent points can be slightly better resolved.

While the information is not as well localised as in the circular flight path, it is however still an improvement over standard 1-D retrievals. Comparing the overall shape of rows of the averaging kernel matrix with the typical corresponding shape for a 1-D retrieval (e.g. see Fig. 4.22(b)), one can see that the 3-D averaging kernel matrix does not oscillate at higher altitudes to the same extent as the 2-D/1-D averaging kernel matrix of the 1-D retrieval does. The 3-D retrieval of the linear flight path is therefore more robust against gradients in the atmosphere. Further, it is expected to achieve a better vertical resolution than conventional 1-D retrievals as the 3-D retrieval setup requires only a weak vertical regularisation.

The given setup can provide a good 3-D picture of the atmosphere, albeit in a very limited volume defined by the volume covered by tangent points. Increasing the instrument altitude would significantly enlarge the well-resolved volume, especially within the UTLS region and make this measurement mode more useful. Within this well resolved volume, a vertical resolution of $\approx$300 m, an along track resolution of $\approx$30 km, and an across track resolution of $\approx$50 km seem feasible.

4.5. Circular flight track with advection

In this section, the effect of a time-varying atmosphere on 3-D tomographic retrievals is analysed. While the time required to acquire the measurements is usually negligible for a conventional 1-D retrieval, the atmosphere might change significantly during the time required to fly a full circle. For simplicity’s sake, the passing of time was neglected for the simulations presented in the previous sections. The retrievals were based on the assumption of an unchanging atmospheric state. In reality, the measurements are not determined by a 3-D state of the atmosphere, but they are determined by a time-varying four-dimensional (4-D) state instead. In contrast to closed flight tracks, the effect of advection on measurements taken while following linear flight tracks is expected to be smaller, as the time shift between measurements of the same volume element is rather small compared to the time shift exhibited by circular flight tracks. Therefore, this section concentrates again on the circular flight path.

First, the effect of a time-varying atmosphere on the 3-D retrieval result needs to be quantified. To this end, the 3-D retrieval is embedded into a 4-D context including time to determine the resolution/averaging of the result in time in Sect. 4.5.1. Then, Sect. 4.5.2 proposes a counter-measure against the smoothing in time by incorporating a priori information on advection into the retrieval. The effectiveness of this counter-measure is then analysed in Sect. 4.5.3.

4.5.1. 4-D analysis of the baseline setup

It is possible to approximately quantify the effect of a time-varying atmosphere on a tomographic retrieval, without knowing in which way it actually changes. Just as the 1-D retrievals ignore the horizontal variation of the atmosphere, the up-to-now presented 3-D retrievals ignore variability in time. So the technique used in Sect. 4.3.6 to quantify the effect of the neglected horizontal dimension on 1-D retrievals can be applied here to determine the effect of the neglected time dimension on 3-D retrievals.

Consequently, the usual 3-D atmosphere is expanded by a fourth dimension representing time. Time is thereby discretised in 150 s steps as a compromise between exactness and memory requirements. The 4-D atmosphere is filled with the 3-D result of the baseline retrieval, which is by definition homogeneous in time. As the simulated measurements were not generated using a time-varying atmosphere, this simplification introduces no error (if the atmosphere were time-varying, an error is introduced by this simplification due to the non-linearity of the forward model). It is straightforward to calculate the Jacobian matrix with respect to the 4-D atmosphere and multiply the 3-D gain matrix of the baseline setup with the 4-D Jacobian matrix to acquire a 4-D/3-D averaging kernel matrix (mapping the 4-D true atmospheric state onto the 3-D retrieval result) that gives quantitative insights into the averaging over time.

As the 4-D/3-D averaging kernel matrix is less well-shaped than the 3-D averaging kernel matrix, it is difficult to condense its shape into simple measures as for example the horizontal resolution, especially with respect to the time dimension. Instead, 2-D cutting planes through the 4-D objects determined by the rows of the 4-D/3-D averaging kernel matrix are presented to demonstrate how the averaging in time affects the end result.

Starting with a data element located in the centre of the volume, Fig. 4.27 shows cutting planes through one row of the 3-D (above) and 4-D/3-D (below)

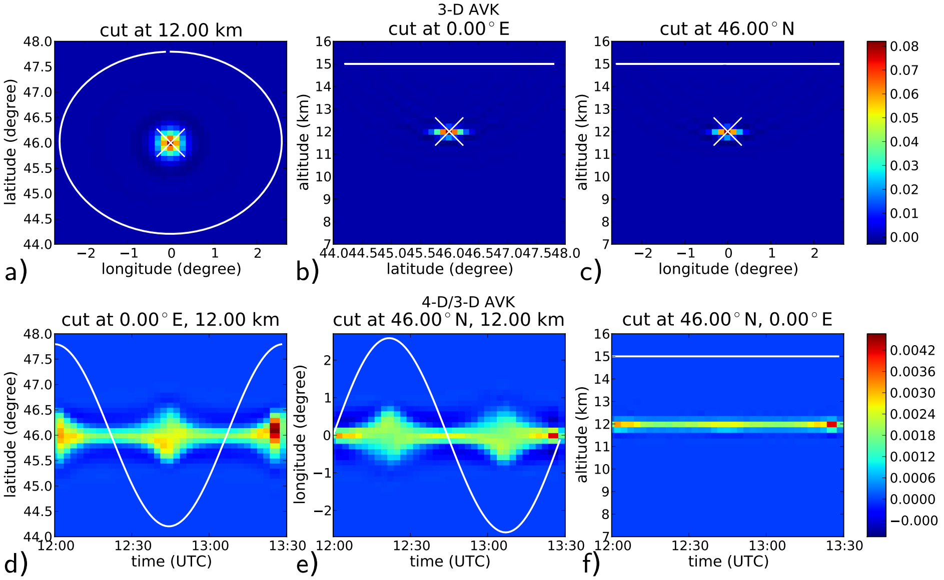

Figure 4.27: A comparison between one row of the 3-D averaging kernel matrix and its 4-D/3-D equivalent for a central element. In the upper three panels, three cutting planes through a row of the 3-D averaging kernel matrix are depicted, all belonging to the element at 0° E, 46° N, and 12 km altitude. The projection of the flight track of the instrument onto the cutting plane is drawn as a white line. The location of the data element is marked by a white cross. For the same data element, the three lower panels depict three cutting planes through the 4-D space described by the row of the 4-D/3-D averaging kernel matrix, given a deeper insight by expanding the time dimension of the central column of the panel above.

averaging kernel matrices. The upper row depicts cutting planes orthogonal to the three major axes of one 3-D averaging kernel matrix row, while the lower row of panels essentially blows up the central column of the panel above it, adding time as a new dimension. In panels (a)–(c), the non-zero part is well localised in space around the retrieved data element at 12 km altitude in the central profile. However, panels (d)–(f) reveal that with respect to localisation in time, it is averaged rather evenly over the whole retrieval time. In addition, one can see that the small “bulges” in panel (d) and panel (e) wax and wane according to the position of the GLORIA instrument. The contribution from each single image is necessarily drawn along its LOS and thereby causes these bulges. The 4-D analysis reveals that the good spatial localisation is realised by summing up many less well localised individual measurements.

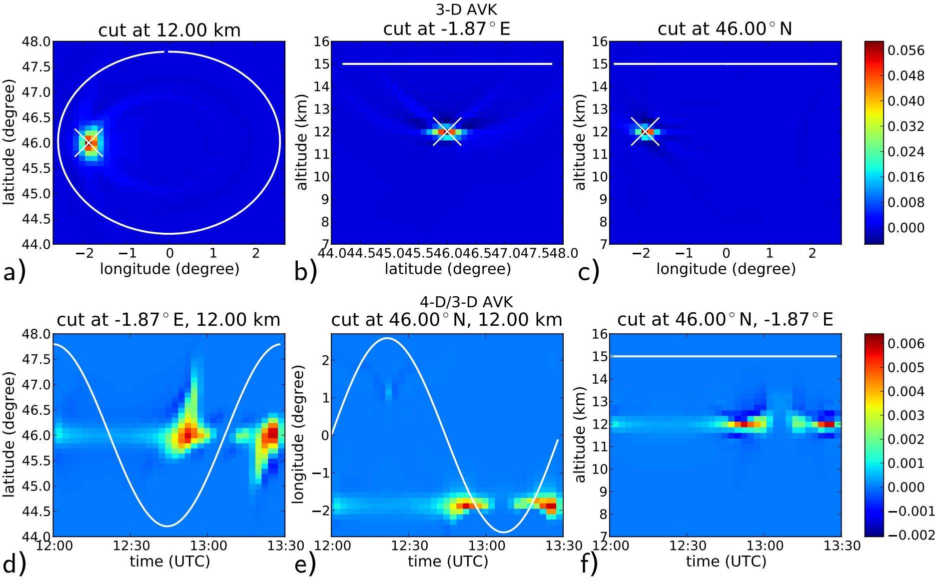

Figure 4.28: A comparison between one row of the 3-D averaging kernel matrix and its 4-D/3-D equivalent for a border element. In the upper row of panels three cutting planes through a row of the 3-D averaging kernel matrix are depicted, all belonging to the element at 1.87° W, 46° N, and 12 km altitude. For the same element, the lower row of panels depicts three cutting planes through the 4-D space described by the row of the 4-D/3-D averaging kernel matrix.

Proceeding westwards, Fig. 4.28 shows cutting planes for a data element close to the border of the area covered with tangent points at 1.87° W, 46° N, and 12 km altitude. While still comparably well localised, some remnants of LOSs can (very faintly) be seen in panels (a) and (b). The smoothing in time looks quite different from the smoothing given for the central element in Fig. 4.27, as it exhibits strong maxima coinciding with the points in time where tangent points of measurements sweep over the data point. Except for the central column of the encircled volume, this usually occurs twice during the flight: once while the instrument is pointing forward, and once while the instrument is pointing backward. This effect is rather typical for all data elements not located on the central profile. Depending on the distance to the centre, these maxima are more or less pronounced.

Concluding, a 4-D Jacobian matrix can be used to analyse how the 3-D retrieval smooths the true 4-D atmospheric state in time to derive the 3-D result. The smoothing in time emphasises those times when tangent points of measurements wander over the data point. The methodology of the 4-D/3-D averaging kernel allows to reliably compare the results of "simple" 3-D tomographic retrievals with corresponding 4-D simulations of atmospheric models or data assimilation systems.

4.5.2. Incorporating advection

This section analyses the effect of the most prevalent source of short-term composition change in the UTLS on the tomographic retrieval, which is advection. Mixing and chemical processes play only a comparatively minor role for the typical time-scale of a tomographic measurement excepting species that are for some reason not in a steady state during the full measurement period. To properly simulate the effect of advection, the so far static true atmospheric state needs to be altered into a time-varying one. Compared to the high contrast in concentration of many trace gas species, mesoscale winds are rather smooth and comparatively well known. It is therefore advantageous to exploit this a priori information about advection, instead of setting up a full 4-D retrieval with an additional regularisation component for time. Although feasible, a true 4-D retrieval requires another magnitude of additional memory and computation time compared to the already demanding 3-D setup.

The European Centre for Medium-range Weather Forecast (ECMWF) maintains an operational assimilation and weather forecasting system providing real-time analysis and forecasting of atmospheric composition. In addition, regular re-analyses of the Earth-system are performed. Amongst other information, ECMWF also provides global wind fields, which are wind speeds in meridional, zonal and vertical direction. The inaccuracies of the provided wind speeds and their effect onto trajectory models were examined by Pickering et al. (1994, 1996) in the southern Atlantic. He found that the ratio of average absolute difference between dropsonde measurements and ECMWF winds to mean of absolute values was up to 0.87. Problematic were especially regions with large horizontal or vertical wind shears, which may not be perfectly located by the generating model. With respect to deriving trajectories from this input data, he suggests to perform a cluster of runs with different closely spaced starting points. Should the resulting trajectories perform similarly, confidence can be placed in the results.

While the ECMWF wind speed data has naturally been improved upon in the past 15 years, one should not rely solely on the data provided by ECMWF or similar institutions. By combining GLORIA measurements with simultaneous dropsonde wind speed measurements around the volume of interest, it would be possible to validate the provided model wind speeds. One might even augment the ECMWF data using data assimilation techniques and the measured wind speeds.

For the following numerical experiments, the ECMWF ERA40 interim data set (Simmons et al., 2006) is used. It is interpolated onto a grid with 0.25° in longitudinal and latitudinal direction and 250 m in vertical direction. It is thereby horizontally ≈2 to 2.5 times as coarse as the retrieval grid. Within the original ECMWF data, the vertical wind speed is given as pressure change ("omega") in Pa/s. Using the supplied pressure values, this value is converted to a vertical velocity in m/s. A trajectory model operating directly on pressure levels might be more exact, though. Two ECMWF ERA40 global data sets were used: 12:00 UTC (Universal Time, Coordinated) and 18:00 UTC of 3 July 2006. Wind speeds at times in between are linearly interpolated from the two supplied datasets. It is assumed that the first simulated image is taken exactly at 12:00 UTC. Pressure changes were small enough during the measurement period to neglect their effect on air temperature. However, more complex meteorological situations might require the implementation of heating and cooling due to pressure changes.

A simple model uses the wind fields to calculate backward trajectories. The intent is to relate any part of the air volume during the circular flight backward in time to the position it had when the first measurement was taken. As it is too time-consuming to calculate a backward-trajectory for each access to an atmospheric data point during the retrieval, lookup tables with pre-calculated trajectories are generated for all grid points of the atmosphere and regular time intervals. During the retrieval, the dis-location of the data point due to advection is derived by linear interpolation in these tables and the atmospheric composition is derived via a 3-D interpolation at the thus discovered original location. In effect, the 4-D state of the retrieval atmosphere is thereby reduced to a simple 3-D state at the time of the first measurement. One might also relate the atmospheric state to the middle of the measurement period instead of its begin and thereby slightly decrease the error introduced by erroneous wind fields to the trajectories.

The trajectory model uses the wind speeds u, v, and w as maps from $\mathbb{R}^4$ (time, longitude, latitude and altitude) to $\mathbb{R}$ given in m/s. Let $x(t)$, $y(t)$, $z(t)$ describe the location of an air parcel at time t. The advection can then be captured by the differential equations

$$\frac{dx(t)}{dt} = u(t, x(t), y(t), z(t)) \tag{4.2}$$

$$\frac{dy(t)}{dt} = v(t, x(t), y(t), z(t)) \tag{4.3}$$

$$\frac{dz(t)}{dt} = w(t, x(t), y(t), z(t)). \tag{4.4}$$

This set of equations can be numerically solved backward from a given time t' towards the start of the measurements at t_0.

A simple fourth-order Runge-Kutta method with fixed step size (e.g. Press et al., 2007) was employed to calculate the trajectories in this study. Varying the step size in the Runge-Kutta scheme, it was found that a step of 10 s gives reliable results, meaning that reducing it further did not provide noticeably different trajectories. Similarly, the effect of the gridding in time on the lookup tables was estimated and a 300 s step size is used for the following numerical experiments.

Under the assumption that during the time frame of taking all measurements mixing and chemical reactions can be neglected, the trajectory model is able to project each point within the 4-D space-time of the retrieval to a 3-D coordinate at the beginning of the retrieval, in this case to 3 July 2006 12:00 UTC.

4.5.3. Trajectory enhanced retrievals

This section analyses the effect of advection on 3-D tomographic retrievals by means of numerical simulations. Three different numerical experiments are now described. In all three, the trajectory model uses the unmodified ECMWF wind fields to generate simulated GLORIA measurements. The impact of the wind on the atmospheric state can be seen in Fig. 4.29, which shows the atmospheric situation at the begin (first measurement) and at the end (last measurement) of the simulated flight. The barbs indicate horizontal wind speeds ranging from 10 m/s to 20 m/s. The wind moves the filament ≈100 km towards north-north-east. Additional visible changes are caused by vertical advection. During the circular flight, the wind changes direction slightly, but overall nearly identical trajectories are calculated by using only the wind field of 12:00 UTC for the time frame of the measurements. The use case at hand is basically a worst-case test, as the wind blows nearly parallel to the steepest gradient observed in the ozone field. This causes a maximal displacement of the ozone filament and is

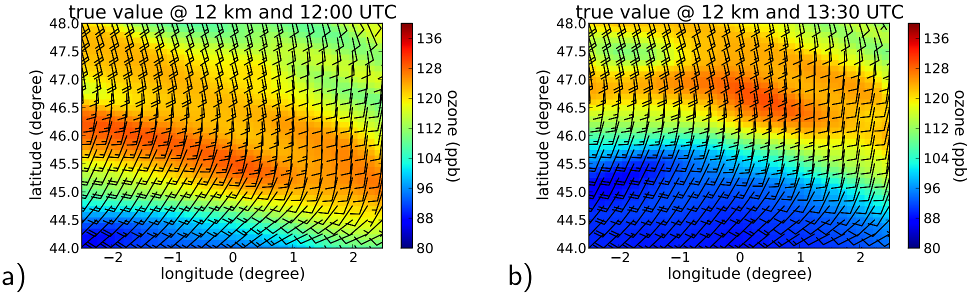

Figure 4.29: The temporal change caused by advection. Panel **(a)** depicts the situation at the begin of the measurement period and is identical to the scene described in Sect. 4.2. In addition, horizontal wind speed at 12 km altitude has been added using barbs, whereby half a line indicates 5 m/s and a full line 10 m/s horizontal wind speed. Panel **(b)** depicts the scene at the end of the measurement period.

thereby well suited to determine the feasibility of the method under adverse circumstances.

Three different retrieval experiments are executed:

1. The first experiment employs the trajectory model for generating the simulated measurements as well as for the retrieval. Thereby, it tries to reconstruct the atmospheric state at the time of the first measurement. This setup shall demonstrate how well the retrieval can compensate for advection with perfect knowledge about the wind.

2. The second experiment uses the trajectory model to generate the simulated measurements but does not use it for the retrieval. Instead, the conventional 3-D retrieval from the previous sections is used. This setup shall examine if a retrieval without compensation is subject to convergence issues and how much the retrieval result is affected by uncompensated advection.

3. The third experiment employs the trajectory model for generating the simulated measurements and for the retrieval. However, it uses a different, degraded wind field consisting of horizontally homogeneous, averaged wind speeds for the retrieval. This setup shall examine the effect of a potentially erroneous wind field on the retrieval result, just as the ECMWF data may also not reflect the true wind speeds.

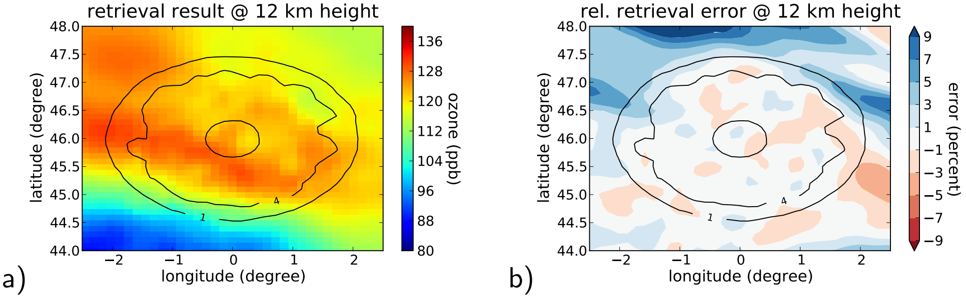

Figure 4.30: The retrieval result of a run with advection and perfect a priori knowledge thereof. Panel **(a)** shows the retrieved ozone values at 12 km height while panel **(b)** depicts the relative error in percent compared to the true values. The number of tangent points within the depicted volume elements is overlaid as a contour plot.

Perfect a priori knowledge

The first experiment takes advection into account for generating the measurements and also uses perfect knowledge about the advection in the retrieval process. As the advection moves air lying southwards of the flight track into the circle described by the instrument, it is expected that those air masses are better resolved than previously, possibly at the cost of reduced resolution for air lying towards the north within the circle.

This is indeed the case as Fig. 4.30 demonstrates. Especially the southern boundary of the ozone filament is well reproduced. The low ozone concentrations towards the south are even quantitatively well given as the error lies below ±2 %. This is quite an improvement compared to Fig. 4.8 of the baseline setup, where southward of 44.5° N the error surpasses 10 %. In contrast, outside the northern half of the circle described by the instrument, the errors are slightly increased with a slight tendency to overestimate true ozone concentrations.

The shape of the averaging kernel matrix rows and the resolution asserts this interpretation. Figure 4.31 depicts two rows of the averaging kernel matrix for two data elements lying outside the circle described by the instrument. The shape of the element towards the south in panel (a) is very well localised contrary to the same element in the baseline setup without wind in Fig. 4.10(b). Another element shown in Fig. 4.31(b), lying as much towards the west as the former element laid towards the south, has the “usual” long-drawn shape. Thus, the achievable resolution depends heavily on the interplay of advection and flight track.

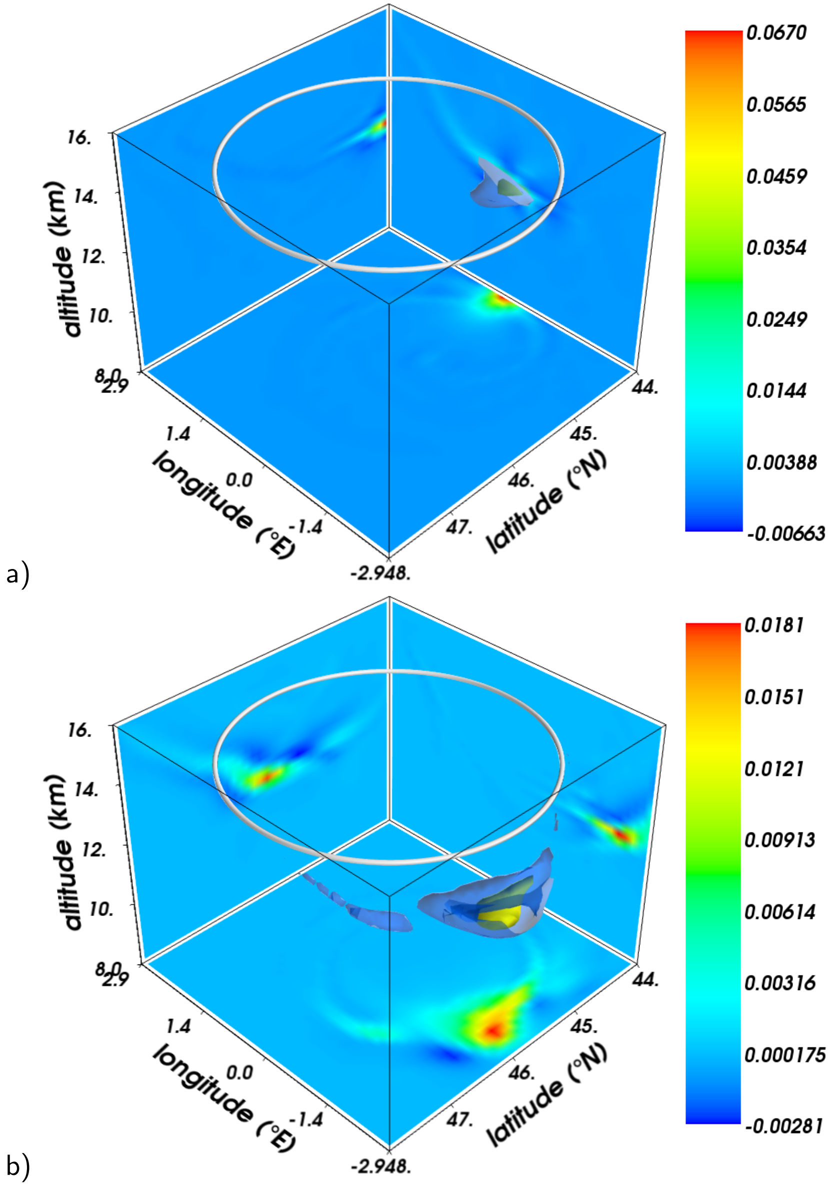

Figure 4.31: 3-D averaging kernel matrix rows for the retrieval with perfect wind speed knowledge that are slightly outside the region encircled by the instrument. Panel **(a)** depicts the row of the averaging kernel matrix for a data element at 0° W, 44° N, and 12 km altitude lying in the direction, from which the wind blows. Panel **(b)** depicts the row for an element at 2.45° W, 46° N, and 12 km altitude lying just as far away from the central profile as (a), but not in down-wind direction.

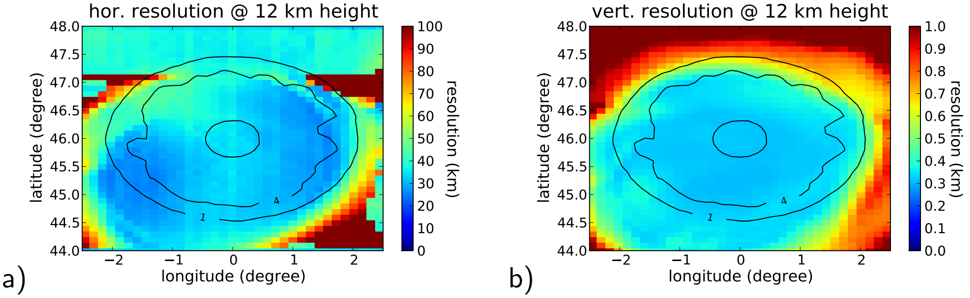

Figure 4.32: Horizontal and vertical resolution of a retrieval with perfect wind speed knowledge. Panel **(a)** shows the horizontal resolution in longitudinal direction and panel **(b)** shows the vertical resolution. The number of tangent points within the volume element is overlaid as a contour plot.

This translates directly to the derived resolution values shown in Fig. 4.32. The horizontal resolution in longitudinal direction is shown in panel (a). Compared to Fig. 4.12, the well resolved area is non-circular and enlarged towards the south, the direction from where the wind blows. The same can be said for the vertical resolution in Fig. 4.32(b). Except for the different distribution of well-resolved elements, the achievable resolution seems to be rather unchanged compared to simulations without advection. The more irregular shape of the rows of the averaging kernel matrix causes the resolution values to be slightly noisier, but the minimum value is nearly unchanged. Seemingly, the GLORIA instrument takes a sufficient amount of measurements to resolve the additional volume of air passing through the circle described by the instrument without a significant degradation of achievable resolution.

No a priori knowledge

While the previous paragraph discussed the best case, perfect knowledge about advection, the worst case is presented in this section: no knowledge about advection. Consequently, this experiment uses measurements that were generated using the ECMWF wind field, but (wrongly) assumes a static atmosphere during the retrieval.

Slightly surprisingly, this setup had no convergence problems and delivered a result within the usual number of iterations. This result is shown in Fig. 4.33(a). It looks quite different from the result of the run incorporating perfect wind speed knowledge in Fig. 4.30. The filament is moved towards the north-north-

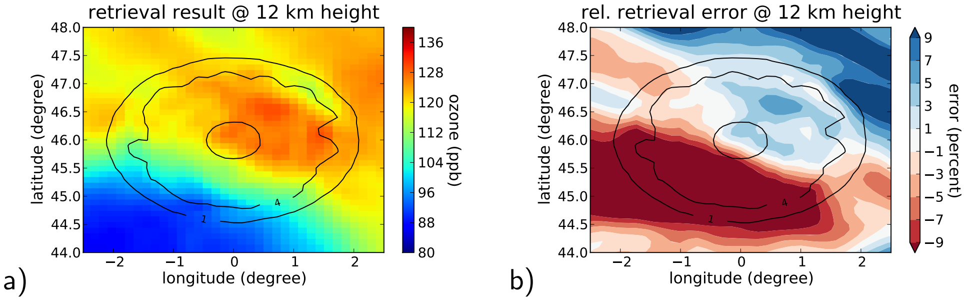

Figure 4.33: The retrieval result of a run with advection and no compensation during the retrieval. Panel **(a)** shows the retrieved ozone values at 12 km height while panel **(b)** depicts the relative error in percent compared to the true values. The number of tangent points within the depicted volume elements is overlaid as a contour plot.

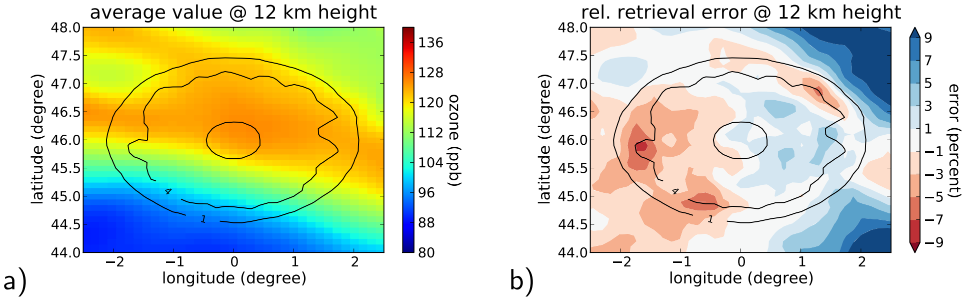

Figure 4.34: The atmospheric state averaged over time in panel **(a)** and the relative error of the retrieval result without wind compensation in relation to the averaged state in panel **(b)**. The number of tangent points within the volume element is overlaid as a contour plot.

west, the same direction the wind blows to. Correspondingly, the relative error plot (comparing with the state at 12:00 UTC) in Fig. 4.30(b) shows large errors in the south-south-east of more than 10 percent.

As discussed in Sect. 4.5.1, the 3-D retrieval without trajectory model compensation averages the true atmospheric state over time. So comparing the result with the state at 12:00 UTC might not be the best frame of reference. Instead an average of the true atmosphere over time might be better suited as is shown in Fig. 4.34. The time-averaged atmosphere in panel (a) was generated by calculating a true 3-D state of the atmosphere for each time a simulated image was taken and averaging all these states with equal weights. While the 4-D/3-D averaging kernel matrix of Sect. 4.5.1 shows that the temporal averaging of the 3-D result is usually not uniform, it is expected that the final result of this retrieval setup is closer to this simple average than to the state at 12:00 UTC. The averaged atmosphere resembles rather closely the retrieval result in Fig. 4.33(a) within the volume covered by tangent points and also towards the south. This impression is asserted in the relative error plot in Fig. 4.34(b). Similar to the retrievals being imparted with perfect knowledge of the wind, the errors are small within the centre and towards the south, the direction from where the wind blows. This implies that the 3-D retrieval without any compensation of advection still generates reliable results, even though they provide only a time-averaged state.

The usual resolution measures cannot be meaningfully employed here, as they ignore the advection. One could perform a 4-D analysis like in Sect. 4.5.1, but a more interesting measure would be the spatial instead of the temporal smoothing. Under the assumption that the only change in atmospheric state is caused by advection, it is possible to express the temporal smoothing in terms of spatial smoothing. This can be achieved by the same method that was previously used to quantify the influence of an additional dimension. An averaging kernel matrix incorporating the spatial smoothing can be constructed by multiplying the gain matrix of the retrieval with a Jacobian matrix that was calculated using the true atmosphere and backward trajectories based on the true advection. The resulting averaging kernel matrix describes the retrieval result in terms of the atmospheric state at 12:00 UTC. The temporal smoothing that the retrieval is actually subject to is thereby effectively translated into a spatial smoothing. Due to the irregular shape of the rows of this averaging kernel matrix, the usual resolution measures along the three spatial axes do not give reliable results. Instead, the diameter of the smallest sphere encompassing all elements of the volume contributing more than half the maximum value of the row is determined and presented in the left panel of Fig. 4.35. This measure is dominated by the horizontal smoothing, so it can be taken as a measure of horizontal resolution that does not distinguish between longitudinal and latitudinal direction. Panel (a) shows that the resolution varies from ≈40 km up to ≈140 km within the usually well resolved region. The first image is taken in the north following the circle in clockwise direction. The worst resolution is given around the start and end point of the instrument's flight path. Here, images from the beginning and end of the flight are recombined, which are taken approximately 90 minutes apart. This leads to maximum displacement of measured air mass and consequently a bad spatial resolution. On the other hand, in the southern part of the circle, the forward and backward looking measurements are taken only 30 minutes apart, leading to a much smaller spatial smoothing.

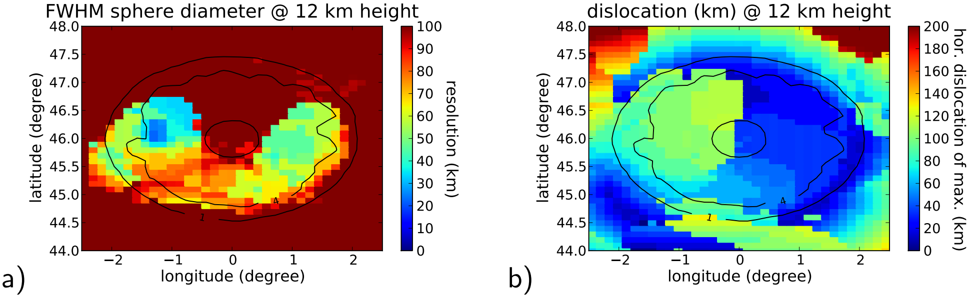

Figure 4.35: The resolution of the retrieval without a priori wind speed information related to the atmospheric state prevalent during the first measurement. The left panel **(a)** shows the diameter of the smallest sphere containing all elements of the associated row of the averaging kernel matrix being at least half as large as the maximum element of the row. Panel **(b)** shows the distance between the shown data element and the element with the largest contribution in the associated row of the averaging kernel matrix. The number of tangent points within the depicted volume elements is overlaid as a contour plot.

Panel (b) of Fig. 4.35 shows the distance between the largest element of the row of the averaging kernel matrix and the data element this row represents. This can be interpreted as a measure for the dislocation of the retrieved element with respect to its location at 12:00 UTC. A value of 0 km means that the retrieved element was at its given location at 12:00 UTC, while a value of 100 km means that the retrieved air parcel was about 100 km away at 12:00 UTC. The right panel shows how the parts of the volume measured first are barely displaced. But the displacement grows larger as more time passes. The nearly linear increase in displacement indicates that the airmass being currently in front of the instrument is effectively measured.

Combining both figures, one can state that except for the northern part of the volume, where measurements from the very start and end of the flight track are combined, the air in front of the instrument at the time of measurement is retrieved. While the resolution in the centre of the volume is quite bad due to the large averaging in time (and correspondingly in space), the outer parts of the volume represent mostly the state of affairs at the time when the instrument is closest.

Imperfect a priori knowledge

The third numerical experiment tries to address the problem of imperfect wind speed knowledge. Just as for the previous two experiments, the trajectory model

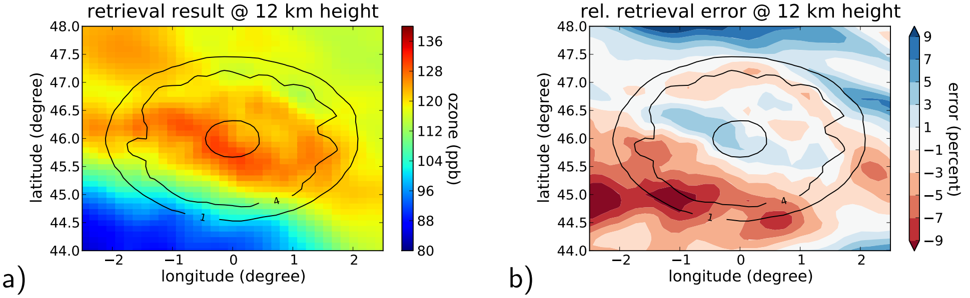

Figure 4.36: The retrieval result of a run with advection and an averaged a priori wind speed knowledge. Panel **(a)** shows the retrieved ozone values at 12 km height while panel **(b)** depicts the relative error in percent compared to the true values. The number of tangent points within the depicted volume elements is overlaid as a contour plot.

is employed to generate the simulated measurements. But for the retrieval, an averaged, horizontally homogeneous wind field is used.

While the wind fields provided by ECMWF may be subject to errors, on average, they provide a good approximation to reality, else they could not be reliably used for weather forecast. For example, Rickard and Lunnon (2001) examined the accuracy of wind predictions by the Met Office with measurements by commercial aircrafts and found that the discrepancy between the predicted wind speeds and the measured ones averaged over the flight duration is only ≈4 percent. This suggests that on average the wind speeds are much better than at individual locations, as is also asserted by Pickering et al. (1996). Consequently, in this numerical experiment, the wind speeds used for the retrieval are generated by using horizontally homogeneous wind fields, whereby the value at each vertical level was generated by horizontally averaging the wind speed from 8° W to 8° E and from 37° N to 52° N. In 12 km altitude this gives a constant wind speed of 10 m/s in zonal and 8 m/s in meridional direction.

Comparing this averaged speed with the true speed used for generating the simulated measurements in Fig. 4.29 it becomes evident that the meridional speed is quite a bit too large as within the centre of the circle described by the instrument the true meridional wind speed is close to zero.

The result of this experiment is presented in Fig. 4.36. The result is an improvement over the simulation run with no a priori knowledge: the filament is placed closer to the true location and the error plot in Fig. 4.36(b) shows errors below 8 %.

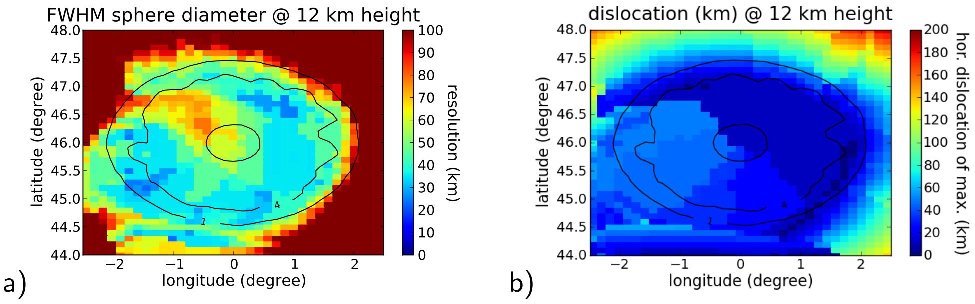

Figure 4.37: The resolution of the retrieval run with advection and an averaged a priori knowledge. The left panel **(a)** shows the diameter of the smallest sphere containing all elements of the associated row of the averaging kernel matrix being at least half as large as the maximum element of the row. Panel **(b)** shows the distance between the shown data element and the element with the largest contribution in the associated row of the averaging kernel matrix. The number of tangent points within the depicted volume elements is overlaid as a contour plot.

The same resolution and displacement figures as for the experiment without a priori wind speed knowledge are shown in Fig. 4.37 for comparison. The worst horizontal resolution within the volume covered by tangent points could be reduced from ≈140 km down to only ≈70 km. The part of the volume with a resolution of ≈40 km is greatly increased and encompasses nearly the full area covered by tangent points except for the middle and north-western part. As before, the volume closest to the start and end of the flight track is still most affected. The right panel of Fig. 4.37 shows the displacement of the retrieved data points. Again, the further the flight progresses, the larger the displacement becomes, even though the maximum displacement has been roughly halved.

This indicates that even inaccurate information about the prevalent wind can be used to improve the retrieval result. It is evident that the quality of knowledge about the advection during the flight is essential for the achievable quality of the retrieval result. Even though plausible results can be generated without any wind speed a priori information, the maximum horizontal resolution of down to 30 km can only be achieved using accurate wind fields.

4.6. Chapter summary

The methodology for large-scale retrievals presented in Chap. 2 was applied on simulated flights of the GLORIA instrument. An ozone filament at 12 km found in GEM-AQ simulations served as a test setup. It was demonstrated that three-dimensionally resolved ozone concentrations can be retrieved.

First, a static atmosphere was assumed. Using a circular flight path, the 3-D structure of the ozone filament was both qualitatively and quantitatively well reproduced in the region well covered by tangent points of measurements. As such a perfectly circular flight track is probably infeasible for practical concerns, different closed curves were examined and it was found that also approximations to a perfect circle deliver comparable results. A 3-D resolution of $\approx$325 m vertically and of $\approx$25 km × 25 km horizontally seems achievable according to the test retrievals employing simulated measurements. The vertical resolution can likely be improved down to 200 m by using a finer vertical measurement grid.

One of the innovative features of the GLORIA instrument is its ability to horizontally pan the LOS of the instrument away from the typical angle of 90° relative to the flight direction of its carrier. Simulations employing no panning demonstrate that this is a key feature, without which 3-D tomographic retrievals are infeasible.

A series of conventional 1-D retrievals was set up to examine the effect of the assumption of horizontal homogeneity. These are subject to large systematic errors depending on the direction of the LOS. A 2-D/1-D averaging kernel matrix was used to analyse the 1-D retrieval and it was found that this matrix is subject to horizontal oscillations, which affect the 1-D retrieval result in the presence of strong gradients and high trace gas concentrations in higher layers of the atmosphere. This influences especially the retrieval quality of ozone concentrations but should also be considered for other species. A tomographic retrieval can use more measurements from different angles to subdue such oscillations and derive a much better inversion result.

As the carrier might not always fly along closed curves for the benefit of the GLORIA instrument, it was also examined, how data collected during a linear flight can be tomographically evaluated. 3-D tomographic retrievals are still possible, even though the volume containing reliable results is greatly reduced. The achievable horizontal resolution is also worse compared to circular flight tracks: $\approx$30 km in along flight track direction and $\approx$50 km in across flight track direction.

Finally, the effect of a time-varying atmosphere on the 3-D tomographic retrieval was examined. First, it was quantified, how the time-varying and thereby 4-D atmospheric state relates to a 3-D retrieval result under the assumption of homogeneity in time: the 3-D result is a weighted average in time of the atmospheric state during the full measurement period, with largest weights at the times and places where the tangent points of measurements are located. Then, the effect of advection on the tomographic retrieval was examined by non-linear end-to-end simulations. Using a trajectory model and wind fields taken from ECMWF ERA40 data sets, it seems possible to fully compensate for the effect of advection by introducing wind speeds as a priori information into the retrieval. It was shown that this can improve the retrieval results for both perfect and imperfect knowledge about true wind speeds. Further, an acceptable retrieval result can be derived even without any compensation at all, albeit at the cost of severe smoothing in time.

The simulations present evidence that the GLORIA instrument will derive highly resolved 3-D volumes of the UTLS, which will enable a better understanding of mesoscale processes and structures in this region. The combination of a 2-D detector array with the ability to pan the LOS delivers sufficient measurements from different angles to enable 3-D reconstructions with a vertical resolution of ≈200 m and a horizontal resolution of ≈25 km. This should allow GLORIA to deliver results with a spatial resolution that is unprecedented for current limb-sounders.

I do not fear computers. I fear the lack of them.

(Isaac Asimov)

5. Summary and outlook

This thesis presented a new methodology for evaluating large-scale, tomographic retrievals. The algorithm scales well from 1-D to 3-D retrievals and also offers diagnostic information for largest problem sizes. It was used to perform studies on two new infrared limb-imager instruments. Both instruments use modern 2-D detector technology that allows for an unprecedented spatial sampling. The first instrument, the PREMIER IRLS, is a satellite-borne instrument with a backward-looking field-of-view. The simulation studies suggest that its dense 3-D measurement sampling can be nearly fully translated into achievable 3-D resolution. The second instrument, GLORIA, is destined to be mounted onto air-borne carriers with a side-ways looking viewing geometry. For the first time, it was demonstrated that 3-D tomographic retrievals are possible using such an instrument.

The introduction posed five main questions regarding problems and characteristics of large-scale tomographic retrievals of limb-sounder measurements. These can now be answered:

How to best ensure the existence and uniqueness of a physically meaningful solution of large-scale 2-D or 3-D inversion problems?

During the analysis of different retrieval schemes, it became evident that a regularisation scheme representable by sparse matrices is crucial due to memory requirements. Otherwise, memory considerations severely limit the retrievable volume size, sampling resolution, and number of retrieved species.

Two such memory conserving regularisation constraints were presented, one based on the auto-regressive approach and one based on Tikhonov regularisation. The former scheme was applied on the evaluation of simulated PREMIER IRLS measurements. It exhibited problems with retrieving wave structures that are not well representable by a coarse retrieval grid. In this case however, refining the retrieval grid solved the problem and the auto-regressive approach is adequate.

A stronger stabilisation can be provided by Tikhonov regularisation, which was successfully applied to the evaluation of simulated GLORIA measurements. In this use case, large parts of the retrieved atmospheric volume lack significant measurement information, requiring the introduction of more a priori knowledge. Future work might consider a location-dependent regularisation strength to differentiate between the applied smoothing within the volume measured from multiple angles and the surroundings.

Both regularisation schemes are adequate for their respective use case, suggesting that the autoregressive approach is sufficient for relatively well-posed problems, whereas more ill-posed ones require a stronger Tikhonov regularisation.

How to numerically solve and diagnose the regularised inverse problem posed by 2-D or 3-D tomographic retrievals?

Gauss-Newton based methods are already state of the art within the field of atmospheric remote sensing and no evidence was found that suggests a different algorithm. These iterative algorithms require the solution of large linear equation systems in each iteration. A complexity analysis of different numerical algorithms suggests that direct solvers for these linear equation systems require too much computation time and memory for large-scale problems. The key point in adapting the Gauss-Newton algorithm for large-scale retrievals lies in avoiding the costly calculation of the linear equation system matrix and its decomposition, and to use a conjugate gradient scheme instead. This method delivers the solution to large scale linear problems in minutes, which would take days using a conventional Cholesky decomposition. This reduces both computation time and memory consumption, and thereby allows even largest problems to be processed. The numerical stability of the method for multi-target retrievals is ascertained by combining the conjugate gradient scheme with a Jacobi preconditioner.

With respect to providing diagnostics for the retrieval result, it seems to be too costly to derive diagnostic quantities for all retrieved data elements. However, a way to calculate said quantities for a selected subset of all data elements was presented. By diagnosing randomly selected points and using interpolation, it is possible to quickly gain an overview over the principal characteristics of the retrieval and to identify, which parts of the volume deserve a closer look.

What kind of spatial resolution can be expected from near-future limb-imager instruments?

The achievable resolution of an emission limb-imager depends largely on its observation geometry. According to the performed simulations, the rearward looking PREMIER IRLS may expect to have a resolution comparable to its measurement grid, which is 50 km along track, 25 km across track and about 0.75 km in the vertical.

For the air-borne GLORIA instrument, which looks sideways and has the ability to pan the field-of-view, the resolution depends largely on the flight track of the carrier. The best resolution seems to be achieved by choosing a roughly circular flight track, delivering a horizontal resolution of ≈25 km by 25 km and a vertical resolution of 200 to 325 m. This would be a significant improvement over what current satellite- and air-borne infrared limb-sounders are capable of and also over what the PREMIER IRLS will be capable of, especially with respect to the vertical direction. This fine resolution may prove very useful for examining fine structures in the UTLS like the tropopause inversion layer.

Practical considerations might sometimes require following less ideal flight tracks, for example a straight line. Even for such linear flight paths, panning the field-of-view of the instrument in combination with a 3-D retrieval gives a significant improvement over traditional 1-D retrievals. The simulations indicate an achievable resolution of 30 km in flight direction and 50 km in perpendicular direction while retaining the same vertical resolution as given for circular flight tracks. This is quite an improvement over typical 1-D retrievals, which usually have a resolution of 100 to 200 km in the line-of-sight direction. A further advantage of the 3-D tomographic evaluation compared to 1-D retrievals is that horizontal homogeneity does not need to be assumed: viewing the same volume from multiple angles gives a sufficient amount of information to significantly decrease the sensitivity of the retrieval against gradients of trace gas concentrations along the line-of-sights.

How does the flight path of the carrier influence the achievable retrieval result for air-borne limb-imager instruments?

As stated above, the flight path has quite an effect on the result of the retrieval. A good agreement between the true state of the atmosphere and the retrieval result can only be expected in that part of the atmospheric volume, which is rather densely covered by tangent points of measurements. An optimal flight path should maximise this volume and should place it over a region of interest in the atmosphere. Flying along closed curves generally delivers good results, whereby the circular route is not necessarily optimal. For example, other curves offer a larger spatially resolved volume albeit with a decreased tangent point density and thereby worse resolution.

For linear flight tracks, the covered volume is much smaller. Using an observer altitude of 15 km (a flight altitude just within reach of the German research aircraft HALO), the extension of the well-resolved region in 12 km altitude in across flight direction is only about 60 km, barely larger than the resolution of the derived atmospheric data elements. Increasing the observer altitude to 19 km (a typical altitude flown by the Russian aircraft Geophysica) doubles that range and makes it much more attractive for the examination of the UTLS region.

How does the temporal variability of the atmosphere relate to the slow carrier speed of air-borne carriers in the context of 3-D tomographic retrievals?

Advection and chemical reactions constantly change the structure and composition of the atmosphere. As tomographic measurement flights may take hours, dynamics and chemistry may significantly alter the atmosphere in this time frame and thereby impact the retrieval. It is therefore important to quantify this effect on tomographic retrievals. Analysing a map between the temporally changing atmosphere and the 3-D retrieval result revealed this result to be a weighted average in time over the changing atmospheric state. In a second step, the retrieval algorithm was enhanced by the capability to compensate for advection, as advection is the most important source of atmospheric change within the examined time frames. The effect of advection can be fully compensated by introducing wind speeds from meteorological sources as a priori knowledge. Numerical experiments indicate that small errors in the assumed wind speeds do not worsen the achievable accuracy and spatial resolution significantly. On the other hand, this implies that the resolution of the retrieval depends largely on the quality of the a priori wind speed fields. But even without any a priori wind speed knowledge, 3-D volumes can be reconstructed albeit with decreased temporal and spatial resolution. However, it is suggested that wind speeds should be accurately measured during the tomographic measurement flight to validate and correct wind fields generated by global or local models.

The large-scale, tomographic evaluation of radiance measurements made by new limb-imagers is a demanding task due to the large amount of involved measurement information and unknowns. The presented algorithms and tools allow dealing with this problem and therefore enable 3-D retrievals. They are also well capable of evaluating conventional retrievals as they currently demonstrate by evaluating CRISTA-NF measurements made during the RECONCILE campaign. Diagnostic tools are available to correctly interpret retrieval results including the effect of a constantly varying target atmosphere. This opens a new window for examining the UTLS and other parts of the atmosphere with an unprecedented resolution and accuracy.

> Something unknown is doing we don't know what.
>
> *(Sir Arthur Eddington)*

A. Appendices

A.1. List of abbreviations

ADM	ADjoint Model
ART	Algebraic Reconstruction Technique
CGA	Curtis-Godson Approximation
CRISTA	Cryogenic Infrared Spectrometers and Telescopes for the Atmosphere
CRISTA-NF	Cryogenic Infrared Spectrometers and Telescopes for the Atmosphere - New Frontiers
DLR	Deutsches Zentrum für Luft und Raumfahrt
ECMWF	European Centre for Medium-range Weather Forecast
EGA	Emissivity Growth Approximation
ESA	European Space Agency
FOV	Field-Of-View
FWHM	Full Width at Half Maximum
GEM-AQ	Global Environmental Multi-scale model, Air Quality
GLORIA	Gimballed Limb Observer for Radiance Imaging of the Atmosphere
GW	Gravity Wave
HALO	High Altitude and LOng range research aircraft
HIRDLS	HIgh Resolution Dynamics Limb Sounder
IRLS	InfraRed Limb-Sounder
JURASSIC	JUelich RApid Spectral SImulation Code
LIMS	Limb Infrared Monitor of the Stratosphere
LOS	Line-Of-Sight
MIPAS	Michelson Interferometer for Passive Atmospheric Sounding

MIPAS-STR	Michelson Interferometer for Passive Atmospheric Sounding on STRatospheric aircraft
MLS	Microwave Limb Sounder
NASA	National Aeronautics and Space Administration
NESR	Noise Equivalent Spectral Radiance
PREMIER	Process Exploration through Measurements of Infrared and millimetre-wave Emitted Radiation
RFM	Reference Forward Model
SAMS	Stratospheric And Mesospheric Sounder
STCE	Software and Tools for Computational Engineering
TLM	Tangent Linear Model
UTC	Universal Time, Coordinated
UTLS	Upper Tropsphere / Lower Stratosphere

A.2. Mathematical notation

This work uses regular cursive symbols (e.g. J) for real numbers, integer number, and functions mapping into $\mathbb{R}$. Bold cursive notation (e.g. $\boldsymbol{x}$) is used for vectors and vector-valued functions, whereas regular bold symbols (e.g. $\mathbf{S}_\mathrm{a}$) refer to matrices and matrix-valued functions.

The following table lists the most important mathematical symbols:

$\mathbf{A}$	Averaging kernel matrix: $\mathbf{A} = \mathbf{G}\mathbf{F}'(\boldsymbol{x}_\mathbf{f})$.
$\boldsymbol{\epsilon}$	Represents a vector of measurement errors.
$\mathbf{G}$	Gain matrix: $\mathbf{G} = \left(\mathbf{S}_\mathbf{a}^{-1} + \mathbf{F}'(\boldsymbol{x}_\mathbf{f})^\mathrm{T}\mathbf{S}_\epsilon^{-1}\mathbf{F}'(\boldsymbol{x}_\mathbf{f})\right)^{-1}\mathbf{F}'(\boldsymbol{x}_\mathbf{f})^\mathrm{T}\mathbf{S}_\epsilon^{-1}$.
$\boldsymbol{F}(\boldsymbol{x})$	The forward model mapping an atmospheric state onto simulated, measurement-error-free radiances.
$\mathbf{F}'(\boldsymbol{x})$	The Jacobian matrix of $\boldsymbol{F}$.
$\mathbf{I}_\mathbf{n}$	The n-by-n identity matrix.
$J(\boldsymbol{x})$	The cost function: $J(\boldsymbol{x}) = (\boldsymbol{F}(\boldsymbol{x}) - \boldsymbol{y})^\mathrm{T}\mathbf{S}_\epsilon^{-1}(\boldsymbol{F}(\boldsymbol{x}) - \boldsymbol{y}) + (\boldsymbol{x} - \boldsymbol{x}_\mathbf{a})^\mathrm{T}\mathbf{S}_\mathbf{a}^{-1}(\boldsymbol{x} - \boldsymbol{x}_\mathbf{a})$.
$\boldsymbol{J}'(\boldsymbol{x})$	The Jacobian matrix of cost function J.
$\mathbf{J}''(\boldsymbol{x})$	The Hessian matrix of cost function J.
$\mathbf{L}_\mathbf{0}$	Zeroth order Tikhonov matrix. Regularises according to absolute value.

$\mathbf{L_1}$	First order Tikhonov matrix. Regularises according to first order derivative of $\boldsymbol{x}$.
$\mathbf{M}$	Equation system matrix of Gauss-Newton: $\mathbf{M} = \left(\mathbf{S}_{\mathbf{a}}^{-1} + \mathbf{F}'(\boldsymbol{x}_i)^{\mathrm{T}}\mathbf{S}_{\epsilon}^{-1}\mathbf{F}'(\boldsymbol{x}_i)\right)$.
$\mathbf{S_a}$	A covariance matrix of the a priori vector $\boldsymbol{x}_{\mathbf{a}}$.
$\mathbf{S}_{\mathbf{a}}^{-1}$	An a priori precision matrix. (Pseudo-)Inverse of $\mathbf{S_a}$.
$\mathbf{S}_{\epsilon}$	A covariance matrix of the measurement error vector $\boldsymbol{\epsilon}$.
$\mathbf{S}_{\epsilon}^{-1}$	Measurement error precision matrix. (Pseudo-)Inverse of $\mathbf{S}_{\epsilon}$.
$\mathbf{S}_{\mathrm{noise}}$	Effect of measurement errors on retrieval result: $\mathbf{S}_{\mathrm{noise}} = \mathbf{G}\mathbf{S}_{\epsilon}\mathbf{G}^{\mathrm{T}}$.
$\boldsymbol{x}$	Represents an atmospheric state.
$\boldsymbol{x}_{\mathbf{f}}$	Represents the final retrieval result.
$\boldsymbol{x}_{\mathbf{t}}$	Represents the true atmospheric state.
$\boldsymbol{y}$	Represents a vector of measurements.
$\boldsymbol{y}_{\mathbf{t}}$	Represents a vector of ideal measurements unaffected by measurement errors.

A.3. Algorithmic differentiation and adjoints

In this section, it is shortly described how the Jacobian matrix of the JURASSIC2 forward model can be efficiently calculated using algorithmic differentiation techniques. A comprehensive description of the algorithms employed in the algorithmic differentiation and their implementation can be found in the technical report of Leppkes and Naumann (2011). The application of these tools on JURASSIC2 is described by Lotz et al. (2011).

For many scientific numerical applications, the tangent linear model (TLM) or the adjoint model (ADM) are of interest. The TLM $\boldsymbol{M}_{\mathrm{TLM}}^{\boldsymbol{x}} : \mathbb{R}^n \mapsto \mathbb{R}^m$ of a real-valued function $\boldsymbol{F} : \mathbb{R}^n \mapsto \mathbb{R}^m$ at location $\boldsymbol{x} \in \mathbb{R}^n$ is just

$$\boldsymbol{M}_{\mathrm{TLM}}^{\boldsymbol{x}}(\boldsymbol{y}) = \mathbf{F}'(\boldsymbol{x})\boldsymbol{y}, \tag{A.1}$$

and the ADM $\boldsymbol{M}_{\mathrm{ADJ}}^{\boldsymbol{x}} : \mathbb{R}^m \mapsto \mathbb{R}^n$ is just

$$\boldsymbol{M}_{\mathrm{ADJ}}^{\boldsymbol{x}}(\boldsymbol{y}) = \mathbf{F}'^{\mathrm{T}}(\boldsymbol{x})\boldsymbol{y}. \tag{A.2}$$

Please note that the implementations of these functions normally do not explicitly use the Jacobian matrix. However with either function available, it is trivial to assemble the Jacobian matrix itself by using unit vectors for $\boldsymbol{y}$.

Typical applications for these functions are sensitivity analyses in the context of meteorological or oceanographic models. The Jacobian matrix shows the sensitivity of output parameters of the model to all input parameters. Consequently, the TLM can be used to examine the effect of a disturbance of one input parameter (i.e. to calculate a column of the Jacobian matrix), while the ADM is used to analyses the cause of anomalies in the result (i.e. to calculate a row of the Jacobian matrix) (Giering and Kaminski, 1998).

Quite often it is possible to manually provide efficient implementations of the TLM or ADM for a given task, but this manual approach requires elaborate adjustment of those programs whenever the main function $\boldsymbol{F}$ is modified. A different approach is to use algorithmic differentiation. JURASSIC2 employs a method that requires only small changes to the source code to automatically generate functions that implement the TLM or ADM based on operator overloading. The normally used floating point types are exchanged by a more complex type provided by the Software and Tools for Computational Engineering (STCE) institute at the RWTH Aachen University that records or “tapes” the execution of the forward model during its execution (Leppkes and Naumann, 2011). This tape can be used afterwards to evaluate the TLM or ADM in an interpretation step. Naturally, the construction of the tape slows down the execution of $\boldsymbol{F}$ and consumes memory per taped operation, yielding serious problems when dealing with large functions $\boldsymbol{F}$.

For example, using the ADM of the cost function J, it is possible to calculate its gradient $\boldsymbol{J}'$ with a single execution of the ADM, which requires in turn a single execution of J itself including the construction of the tape and one interpretation run of the tape. The theoretical minimum for the cost of this operation is 2 to 5 times the cost of the execution of J itself, whereby a factor of 5 can often be achieved in practise (e.g. Griewank and Walther, 2008, p.83ff). This makes this approach much more efficient for large vectors $\boldsymbol{x}$ of length $n \gg 5$ than the method of finite differences, which requires $n+1$ separate executions of the cost function J.

For example, let the function f be

$$f(\boldsymbol{x}) = \exp\left(x_1 x_2\right) + x_2, \tag{A.3}$$

with $\boldsymbol{x} = (x_1, x_2)$. It can then be decomposed in the functions $f_1(a,b) = a + b$, $f_2(a,b) = (\exp(a), b)$, and $f_3(a,b) = (ab, b)$:

$$f(\boldsymbol{x}) = f_1(f_2(f_3(x_1, x_2))). \tag{A.4}$$

According to the chain rule, the ADM calculates

$$f'^{\mathrm{T}}(\boldsymbol{x})y = f_3'^{\mathrm{T}}(x_1,x_2)\cdot f_2'^{\mathrm{T}}(f_3(x_1,x_2))\cdot f_1'^{\mathrm{T}}(f_2(f_3(x_1,x_2)))y \tag{A.5}$$

$$= \begin{pmatrix} x_2 & 0 \\ x_1 & 1 \end{pmatrix}\cdot\begin{pmatrix} \exp(x_1x_2) & 0 \\ 0 & 1 \end{pmatrix}\cdot\begin{pmatrix} 1 \\ 1 \end{pmatrix} y \tag{A.6}$$

by multiplying y successively with the matrix to its left until the gradient of f is given.

The ADM implemented in JURASSIC2 employs a tape to perform the evaluation of the chain rule. First, the execution of the function needs to be taped. Using variables with increasing indices to represent the tape, the evaluation of the example function f can be described as

$$x_3 = x_1\cdot x_2 \tag{A.7}$$

$$x_4 = \exp(x_3) \tag{A.8}$$

$$x_5 = x_2 + x_4, \tag{A.9}$$

where x_5 captures the result. The ADM will now calculate the derivatives in associated variables usually marked with a bar as in $\bar{x}_1$. The values of all x_i are available on the tape. The adjoint interpretation of the tape goes through the tape in reverse order, starting with the last operation:

$$\begin{aligned}
&\bar{x}_5 = y \\
&\left.\begin{aligned}
\bar{x}_2 &= \frac{\partial x_5}{\partial x_2}\bar{x}_5 = \bar{x}_5 \\
\bar{x}_4 &= \frac{\partial x_5}{\partial x_4}\bar{x}_5 = \bar{x}_5
\end{aligned}\right\}\text{Eq. (A.9).} \\
&\left.\bar{x}_3 = \frac{\partial x_4}{\partial x_3}\bar{x}_4 = \exp(x_3)\bar{x}_4\right\}\text{Eq. (A.8).} \\
&\left.\begin{aligned}
\bar{x}_1 &= \frac{\partial x_3}{\partial x_1}\bar{x}_3 = x_2\bar{x}_3 \\
\bar{x}_2 {+}&= \frac{\partial x_3}{\partial x_2}\bar{x}_3 = x_1\bar{x}_3
\end{aligned}\right\}\text{Eq. (A.7).}
\end{aligned}$$

If an $\bar{x}_i$ appears multiple times on the left-hand side, all terms need to be added as in the case of $\bar{x}_2$ above. This reverse interpretation of the tape gives essentially the same calculation that is executed when Eq. (A.6) is evaluated from right to left. Using $y = 1$, the gradient of f is $f'(x_1, x_2) = (\bar{x}_1, \bar{x}_2) = (x_2 \exp(x_1 x_2), 1 + x_1 \exp(x_1 x_2))$. More sophisticated implementations optimise the tape already during its recording, which speeds up the following interpretation.

The efficient calculation of Jacobian matrices of the JURASSIC2 forward model $\boldsymbol{F}$ as described in Sect. 2.2.5 is a direct application of an ADM at the appropriate place, which is in this case not the full forward model function $\boldsymbol{F}$. Splitting the forward model $\boldsymbol{F}$ therefore into an instrument model $\boldsymbol{H}$ and the pencilbeam calculation $\boldsymbol{P}$ gives

$$\boldsymbol{F}(\boldsymbol{x}) = \boldsymbol{H}(\boldsymbol{P}(\boldsymbol{x})), \tag{A.10}$$

which implies for the Jacobian matrix according to the chain rule:

$$\mathbf{F}'(\boldsymbol{x}) = \mathbf{H}'(\boldsymbol{P}(\boldsymbol{x})) \cdot \mathbf{P}'(\boldsymbol{x}). \tag{A.11}$$

Ignoring for simplicity's sake the instrument parameters gain, offset and elevation angle, the instrument model $\boldsymbol{H}$ is a simple linear map representable by a matrix $\mathbf{H}$, so that Eq. (A.11) simplifies to

$$\mathbf{F}'(\boldsymbol{x}) = \mathbf{H} \cdot \mathbf{P}'(\boldsymbol{x}). \tag{A.12}$$

The function $\boldsymbol{P}$ consists of the combined pencilbeam calculations that each map the full atmospheric state onto individual radiance values. As the pencilbeams are mutually independent from one another, the function $\boldsymbol{P}$ can be split into p individual functions p_i, each mapping the full atmospheric state onto a single radiance value. For each p_i, an ADM model can be constructed and used to calculate the gradient $\boldsymbol{p}'_\mathbf{i}(\boldsymbol{x})$ in the time it usually costs to evaluate just p_i times a small constant factor. Evaluating a single pencilbeam in this manner is a small enough problem so that the memory consumption of the taping process is negligible. The gradients $\boldsymbol{p}'_\mathbf{i}(\boldsymbol{x})$ are then assembled to construct the Jacobian matrix $\mathbf{P}'(\boldsymbol{x})$, which in turn can be multiplied with $\mathbf{H}$ to calculate $\mathbf{F}'(\boldsymbol{x})$.

As the exemplary calculations in Fig. 2.4 show, the time needed to construct the full Jacobian matrix $\mathbf{F}'$ takes about five times as long as a single evaluation of the forward model $\boldsymbol{F}$ for the tomographic test cases and is thereby close to the theoretical optimum.

A.4. Setup of $\mathbf{L}_1^\mathbf{z}$ for Tikhonov regularisation

The three-dimensional, rectilinear grid is defined by three vectors $\boldsymbol{g}^x \in \mathbb{R}^{n_x}$, $\boldsymbol{g}^y \in \mathbb{R}^{n_y}$ and $\boldsymbol{g}^z \in \mathbb{R}^{n_z}$ that consist of the ordered (ascending in the JURASSIC2 implementation) coordinates (in JURASSIC2 longitude for $\boldsymbol{g}^x$, latitude for $\boldsymbol{g}^y$ and altitude for $\boldsymbol{g}^z$). The elements of the state space vector $\boldsymbol{x}$ are ordered also according to the coordinates, varying fastest in altitude (z) and slowest in latitude (x). Last, three maps h_x, h_y and h_z are needed that map the coordinates of the i-th element of $\boldsymbol{x}$ onto the corresponding index of the coordinate in the coordinate vectors $\boldsymbol{g}^x$, $\boldsymbol{g}^y$ or $\boldsymbol{g}^z$. For example, if the x-coordinate of the i-th element of $\boldsymbol{x}$ would be the smallest one contained in the grid, the function h_x would map i onto the index 0, as the first element of $\boldsymbol{g}^x$ is the smallest x-coordinate. Here, also the convention is used that g_i^x denotes the i-th element of $\boldsymbol{g}^x$.

With $\mathbf{L}_1^\mathbf{x} = (l_{i,j}^x)_{i,j}$, the individual $l_{i,j}^x$ are defined as

$$l_{i,j}^x = \begin{cases} -1/\left|{\boldsymbol{g}^x}_{h_x(i)+1} - {\boldsymbol{g}^x}_{h_x(i)}\right| \\ \qquad \text{if } i = j \text{ and } h_x(i) < n_x - 1 \\ 1/\left|{\boldsymbol{g}^x}_{h_x(i)+1} - {\boldsymbol{g}^x}_{h_x(i)}\right| \\ \qquad \text{if } h_x(i) + 1 = h_x(j),\, h_x(i) < n_x - 1,\, h_y(i) = h_y(j), \\ \qquad \text{and } h_z(i) = h_z(j) \\ 0 \quad \text{else.} \end{cases} \tag{A.13}$$

Please note that the absolute value function $|\cdot|$ in this case shall also imply a conversion to kilometres (where applicable), which means that the same difference in longitude results in different values for points at different latitudes. The first term describes the main diagonal, the second term a side diagonal. In the case of multi-target retrievals, an additional condition must ensure that the entry is zero if i and j describe different target types and a row-scaling must be introduced that introduces different weights for each target type as described by Steck et al. (2005) for 2-D regularisation. The inverse of the typical standard deviation of a target seems a reasonable starting value for such a scaling factor. In the same manner, it is possible to introduce a location-dependent regularisation by scaling the rows of the $\mathbf{L}$ matrices differently. The matrices $\mathbf{L}_1^\mathbf{y}$ and $\mathbf{L}_1^\mathbf{z}$ can be likewise constructed.

Multiplying the matrix $\mathbf{L}_1^\mathbf{x}$ with the vector $\boldsymbol{x}$ corresponds to computing the partial derivative $\partial/\partial x$ of the atmospheric profile using finite differences and the closest neighbouring point. It is straightforward to extend this approach to include higher moments. One can also use formulae that better approximate the first order derivative by including further neighbouring point, but looses thereby constraints on further boundary values.

A.5. Analytical inverse of S_a for the autoregressive model

To exploit any given sparsity of the inverse of $\mathbf{S_a}$, said inverse needs to be easily accessible. For the autoregressive model as described in Sect. 2.3.1, one can define three simple matrices, which each remove all exponential terms belonging to one space dimension. Each such matrix is symmetric and only three of its diagonals are non-zero. The product of all three matrices is then the inverse $\mathbf{S_a}^{-1}$. This is a straightforward extension of the analytical inverse for 1-D problems described by Steck and von Clarmann (2001). With an efficient implementation, the inverse can be set up in linear time, taking only a second for the discussed 3-D problems.

The three-dimensional, rectilinear grid is defined by three vectors $\boldsymbol{g^x} \in \mathbb{R}^{n_x}$, $\boldsymbol{g^y} \in \mathbb{R}^{n_y}$ and $\boldsymbol{g^z} \in \mathbb{R}^{n_z}$ that consist of the ordered (ascending in the JURASSIC2 implementation) coordinates (the units of which are in JURASSIC2 longitude for $\boldsymbol{g^x}$, latitude for $\boldsymbol{g^y}$ and altitude for $\boldsymbol{g^z}$). The elements of the state space vector $\boldsymbol{x}$ are ordered also according to the coordinates, varying fastest in altitude and slowest in latitude. Last three maps h_x, h_y and h_z are needed that map the coordinates of the i-th element of $\boldsymbol{x}$ onto the corresponding index of the coordinate in the coordinate vectors $\boldsymbol{g^x}$, $\boldsymbol{g^y}$ or $\boldsymbol{g^z}$. For example, if the x-coordinate of the i-th element of $\boldsymbol{x}$ would be the smallest one contained in the grid, the function h_x would map i onto the index 0, as the first element of $\boldsymbol{g^x}$ is the smallest x-coordinate. Here, also the convention is used that g_i^x denotes the i-th element of $\boldsymbol{g^x}$.

Let the helper expression $\alpha^x(i,j)$ be $\exp\left(-\frac{g_i^x - g_j^x}{c_x}\right)$, and $b_{i,j}^x$ the element in the i-th row and j-th column of the matrix $\mathbf{B^x}$. Then

$$b^x_{i,j} = \begin{cases} \dfrac{1}{\left(1-\alpha^x(h_x(i)+1,h_x(i))^2\right)} \\ \qquad \text{if } i=j \text{ and } h_x(i)=0 \\ \dfrac{1-\alpha^x(h_x(i)+1,h_x(i)-1)^2}{\left(1-\alpha^x(h_x(i),h_x(i)-1)^2\right)\left(1-\alpha^x(h_x(i)+1,h_x(i))^2\right)} \\ \qquad \text{if } i=j \text{ and } 0<h_x(i)<n_x-1 \\ \dfrac{1}{\left(1-\alpha^x(h_x(i),h_x(i)-1)^2\right)} \\ \qquad \text{if } i=j \text{ and } h_x(i)=n_x-1 \\ -\dfrac{\alpha^x(h_x(i)+1,h_x(i))}{\left(1-\alpha^x(h_x(i)+1,h_x(i))^2\right)} \\ \qquad \text{if } h_x(i)=h_x(j)-1,\ h_x(i)<n_x-1,\ h_y(i)=h_y(j), \\ \qquad \text{and } h_z(i)=h_z(j) \\ -\dfrac{\alpha^x(h_x(i),h_x(i)-1)}{\left(1-\alpha^x(h_x(i),h_x(i)-1)^2\right)} \\ \qquad \text{if } h_x(i)=h_x(j)+1,\ h_x(i)>0,\ h_y(i)=h_y(j), \\ \qquad \text{and } h_z(i)=h_z(j) \\ 0 \quad \text{else.} \end{cases} \tag{A.14}$$

The first three terms describe the main diagonal, the following two describe the two side-diagonals. In the case of multi-target retrievals, an additional condition must ensure that the entry is zero in case i and j describe different entities. It is straightforward to likewise define the matrices $\mathbf{B^y}$ and $\mathbf{B^z}$. To handle the σ_i in $\mathbf{S_a}$, one finally needs to do an element-wise division of only $\mathbf{B^x}$ by the matrix $(\sigma_i \cdot \sigma_j)_{i,j}$. Then $\mathbf{B^x} \cdot \mathbf{B^y} \cdot \mathbf{B^z}$ is equal to $\mathbf{S_a}^{-1}$. The resulting matrix will only have up to 27 non-zero entries per row independent of n and m.

Due to the peculiar distribution of the non-zero elements of the matrices and their symmetry, it is possible to construct the inverse row-by-row as interestingly all other rows do not contribute to the result of the multiplication. By further optimising the construction and the multiplication to only work on non-zero entries, the full inverse can be constructed in a few seconds for problems for up to millions of unknowns on commodity hardware using only a single thread. Especially this latter optimisation is important to achieve linear performance.

A.6. Analytical root of $S_{\mathbf{a}}^{-1}$ for the autoregressive model

With the sparse inverse matrix $\mathbf{S}_{\mathbf{a}}^{-1}$ given, one can apply the Cholesky-Banachiewicz algorithm to quite efficiently build a Cholesky-decomposition, which delivers ${\mathbf{S}_{\mathbf{a}}}^{-\frac{1}{2}}$. As shorthand, the individual elements of the inverse and the root are identified by ${\mathbf{S}_{\mathbf{a}}}^{-1} = \left(a_{i,j}\right)_{i,j}$ and ${\mathbf{S}_{\mathbf{a}}}^{-\frac{1}{2}} = \left(l_{i,j}\right)_{i,j}$. Then the root can be constructed row by row as

$$l_{i,j} = \begin{cases} \sqrt{a_{i,i} - \sum\limits_{k=1}^{i-1} l_{i,k}^2}, & \text{for } i = j, \\ l_{j,j}^{-1} \left(a_{i,j} - \sum\limits_{k=1}^{j-1} l_{i,k} l_{j,k} \right), & \text{for } i > j, \\ 0, & \text{for } i < j. \end{cases} \tag{A.15}$$

Using this definition, the root can be row-wise constructed. However, the already assigned elements are accessed column-wise during the construction of further elements. In JURASSIC2, the root is stored in a row-major compressed matrix storage but sorted indices of the non-zero elements of each column are stored during construction, too. As the root is just as sparse as ${\mathbf{S}_{\mathbf{a}}}^{-1}$, this results in only a handful of costly random accesses. Adding the usual optimisations of avoiding accessing zero elements, the calculation of the root can also be performed in linear time and is of comparable complexity to the calculation of the inverse. The numerical stability of this decomposition is adequate for the given problems. Especially for multi-target retrievals, it is important to scale all quantities to a value close to ‘1’ before proceeding to reduce rounding errors. Due to the sparsity of both matrices, the number of operations is rather small and therefore the rounding errors stays acceptable.

A.7. Conjugate gradient algorithm

This section presents the conjugate gradient algorithm as it is implemented in JURASSIC2 for reference.

```
$r_0 = b - \mathbf{A}x_0$
$p_0 = \mathbf{M}^{-1} r_0$
$\alpha_0 = \langle r_0, p_0 \rangle$
for $i$ in range(1, maxiter):
    if $(||r_{i-1}||_2 < \epsilon_{\text{abs}})$ or $(||r_{i-1}||_2 / ||b||_2 < \epsilon_{\text{rel}})$ :
        break
    $v_i = \mathbf{A} p_{i-1}$
    $\lambda_i = \alpha_{i-1} / \langle v_i, p_{i-1} \rangle$
    $x_i = x_{i-1} + \lambda_i p_{i-1}$
    $r_i = r_{i-1} - \lambda_i v_i$
    $z_i = \mathbf{M}^{-1} r_i$
    $\alpha_i = \langle r_i, z_i \rangle$
    $p_i = (\alpha_i / \alpha_{i-1}) p_{i-1} + z_i$
return $x_i$
```

Table A.3: This algorithm describes the conjugate gradient algorithm in a pseudo code similar to Python. The equation system matrix $\mathbf{A}$, the preconditioner matrix $\mathbf{M}^{-1}$ and the r.h.s. b need to be supplied. Per iteration, only one matrix-vector product with $\mathbf{A}$ and one with $\mathbf{M}^{-1}$ is required.

A.8. Parametrisation of the conjugate gradient algorithm

The combination of a Newton-based minimiser with the conjugate gradient algorithm as described in Sect. 2.3.3 exhibits itself regularising properties (Hanke, 1997). This may be exploited to reduce the amount of time required for the inversion. While the most computation time in non-linear retrievals is used for calculating the Jacobian matrices $\mathbf{F}'(x_i)$, test runs can be executed very efficiently with a linearised retrieval using a fixed, pre-calculated Jacobian matrix. Further, the conjugate gradient method does not lend itself as easily to efficient parallelisation on shared memory machines as the calculation of the Jacobian matrix, implying that currently spending long time in the iterative solver decreases the overall speed-up factor of the parallelisation.

According to Hanke (1995), the regularisation properties of the conjugate gradient algorithm depend on the number of performed iterations. Further, us-

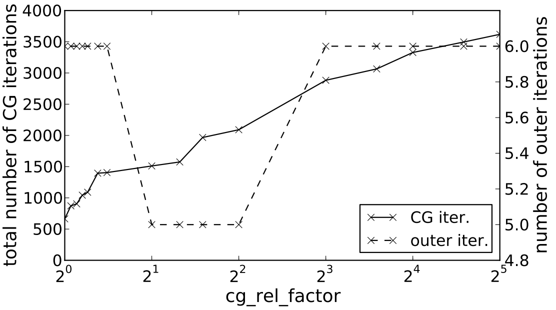

Figure A.1: The effect of parameterising the conjugate gradient scheme on solving the baseline setup of Sect. 4.2. 'cg_rel_factor' describes a multiplicative adjustment factor for modifying the required reduction of the residuum after each outer iteration.

ing only a single iteration corresponds to a steepest descent step while iterating until the error becomes zero corresponds to a Newton step. This shows the similarity to the Levenberg-Marquardt iteration scheme that varies the strength λ of a Tikhonov regularisation to, in effect, also vary between a steepest descent step and a Newton step (Rodgers, 2000).

To reduce computation time, it is more efficient, not to use many iterations in the conjugate gradient method to exactly solve the problem posed by each step of the minimiser, but to reduce the number of iterations in the conjugate gradient scheme to implicitly introduce a regularisation that can replace the Levenberg-Marquardt regularisation.

"Exact solution" in this sense means that the norm of the error of the solution $\boldsymbol{x}$ to the equation system $||\mathbf{A}\boldsymbol{x} - \boldsymbol{b}||_2$ is numerically zero, if the residuum is less than 10^{-12}. An heuristic was implemented that varies the required relative reduction of error $||\mathbf{A}\boldsymbol{x} - \boldsymbol{b}||_2/||\boldsymbol{b}||_2$ in the conjugate gradient scheme similarly to how the Levenberg-Marquardt parameter is usually varied. That is, it is reduced, if a reduction of the cost function could be achieved, or increased in case no reduction could be achieved. The aim is to both reduce the amount of (outer) Newton iterations and (inner) conjugate gradient iterations to save computation time. This scheme converges according to Nocedal and Wright (2006, Theorem 7.1) and uses for the discussed 3-D tomographic problems much less costly evaluations of the forward model than other usual choices based on the norm of the current gradient of the cost function (e.g. Nocedal and Wright, 2006, p.165ff).

Some exemplary results are depicted in Fig. A.1. The initial required reduction of the residuum is set to 0.1, meaning that the residuum should be reduced until its norm is smaller than 10 percent of the norm of the right hand side. Depicted is how the number of outer and inner iterations changes if the adjustment factor is modified. For an adjustment factor smaller than 1.2, the outer iteration stops with a negligibly larger value of the cost function (with a relative error of 0.01 percent), which could be fixed by adjusting the convergence criteria of the outer iteration. For smaller reduction and adjustment factors than depicted, the number of necessary outer iterations increases significantly. The figure is typical for other initial required reduction values. There is usually an optimum, where the number of outer iterations is minimal while the number of required inner iterations steadily increases.

Acknowledgments

I'd like to address my first thanks to Prof. Dr. Martin Riese for trusting me with this interesting research topic and for offering me the opportunity to work at the IEK-7. Thanks for the regular helpful discussions about my scientific results and papers to be published.

I am very grateful to Dr. Martin Kaufmann, whose open door and nagging questions proved invaluable during the past years. He simply managed to push me beyond my limits.

I thank also Dr. Lars Hoffmann for the great work he did with JURASSIC, upon the extension of which this thesis is based, and for the frequent discussions we had about it.

I'd like to express my sincere gratitude to all remaining colleagues from the IEK-7 and from the atmosphere physics department of the Bergische Universität Wuppertal. Working with them for the past three years has been a real pleasure.

A special thanks goes to the German Research Foundation, who provided the funding for my first year by the RASGLO project within the HALO SPP, and to the German Research School for Simulation Sciences, who sponsored me during the last two years.

Last but by far not least, I express my heartfelt gratitude to my wife Martina Ungermann for bearing with me for the whole time. Without her loving support, this would have been infeasible.

Bibliography

Alexander, M. J., 1998: Interpretations of observed climatological patterns in stratospheric gravity wave variance. *Geophys. Res. Lett.*, 103:8627–8640, doi:10.1029/97JD03325.

Alexander, M. J., S. D. Eckermann, D. Broutman, and J. Ma, 2009: Momentum flux estimates for South Georgia Island mountain waves in the stratosphere observed via satellite. *Geophys. Res. Lett.*, 36(L12816), doi:10.1029/2009GL038587.

Alexander, M. J., J. Gille, C. Cavanaugh, M. Coffey, C. Craig, V. Dean, T. Eden, G. Francis, C. Halvorson, J. Hannigan, R. Khosravi, D. Kinnison, H. Lee, S. Massie, and B. Nardi, 2008: Global estimates of gravity wave momentum flux from high resolution dynamics limb sounder (HIRDLS) observations. *J. Geophys. Res.*, 113(D15S18), doi:10.1029/2007JD008807.

Alexander, M. J. and K. H. Rosenlof, 2003: Gravity-wave forcing in the stratosphere: Observational constraints from the upper atmosphere research satellite and implications for parameterization in global models. *Geophys. Res. Lett.*, 108, doi:10.1029/2003JD003373.

Birner, T., D. Sankey, and T. G. Shepherd, 2006: The tropopause inversion layer in models and analyses. *Geophys. Res. Lett.*, 33(L14804), doi:10.1029/2006GL026549.

Burger, M. and B. Kaltenbacher, 2006: Regularizing Newton-Kaczmarz methods for nonlinear ill-posed problems. *SIAM J. Numer. Anal.*, 44(1):153–182, doi:10.1137/040613779.

Carlotti, M., G. Brizzi, E. Papandrea, M. Prevedelli, M. Ridolfi, B. M. Dinelli, and L. Magnani, 2006: GMTR: Two-dimensional geo-fit multitarget retrieval model for Michelson Interferometer for Passive Atmospheric Sounding/Environmental Satellite observations. *Appl. Optics*, 45(4):716–727, doi:10.1364/AO.45.000716.

Carlotti, M., B. M. Dinelli, P. Raspollini, and M. Ridolfi, 2001: Geo-fit approach to the analysis of limb-scanning satellite measurements. *Appl. Optics*, 40:1872–1885, doi:10.1364/AO.40.001872.

von Clarmann, T., C. De Clercq, M. Ridolfi, M. Höpfner, and J.-C. Lambert, 2009: The horizontal resolution of MIPAS. *Atmos. Meas. Tech.*, 2:47–54, doi:10.5194/amt-2-47-2009.

Curtis, A. R., 1952: Discussion of 'A statistical model for water vapour absorption' by R. M. Goody. *Quart. J. Roy. Meteorol. Soc.*, 78:638–640.

Deuflhard, P. and A. Hohmann, 1993: *Numerische Mathematik I.* de Gruyter.

DLR, 2010: Halo website. URL `http://www.halo.dlr.de/aircraft/specifications.html`. Retrieved on 2010-08-06.

Dobson, G. M. B., 1968: Forty years' research on atmospheric ozone at Oxford: a history. *Appl. Optics*, 7(4):387–405, doi:10.1364/AO.7.000387.

Drummond, J. R., J. T. Houghton, G. D. Peskett, C. D. Rodgers, M. J. Wale, J. Whitney, and E. J. Williamson, 1980: The stratospheric and mesospheric sounder on Nimbus 7. *Philos. T. R. Soc. S.-A*, 296:219–241, doi:10.1098/rsta.1980.0166.

Dudhia, A., P. E. Morris, and R. J. Wells, 2002: Fast monochromatic radiative transfer calculations for limb sounding. *J. Quant. Spectrosc. Radiat. Transfer*, 74:745–756, doi:10.1016/S0022-4073(01)00285-0.

Dunkerton, T., 1997: The role of gravity waves in the quasi-biennial oscillation. *J. Geophys. Res.*, 102:26053–26076, doi:10.1029/96JD02999.

Eckermann, S. D., L. Hoffmann, M. Höpfner, D. L. Wu, and M. J. Alexander, 2009: Antarctic NAT PSC belt of June 2003: Observational validation of the mountain wave seeding hypothesis. *Geophys. Res. Lett.*, 36(L02807), doi:10.1029/2008GL036629.

Eckermann, S. D. and P. Preusse, 1999: Global measurements of stratospheric mountain waves from space. *Science*, 286(5444):1534–1537, doi:10.1126/science.286.5444.1534.

Elbern, H. and H. Schmidt, 1999: A four-dimensional variational chemistry data assimilation scheme for Eulerian chemistry transport modeling. *J. Geophys. Res.*, 104(D15):18583–18598, doi:10.1029/1999JD900280.

Engl, H., M. Hanke, and A. Neubauer, 1996: *Regularization of Inverse Problems*. kluwer academic publishers.

Ern, M., P. Preusse, M. J. Alexander, and C. D. Warner, 2004: Absolute values of gravity wave momentum flux derived from satellite data. *J. Geophys. Res.*, 109(D20103), doi:10.1029/2004JD004752.

Ern, M., P. Preusse, and C. D. Warner, 2005: A comparison between CRISTA satellite data and Warner and McIntyre gravity wave parameterization scheme: horizontal and vertical wavelength filtering of gravity wave momentum flux. *Adv. Space Res.*, 35:2017–2023, doi:10.1016/j.asr.2005.04.109.

Ern, M., P. Preusse, and C. D. Warner, 2006: Some experimental constraints for spectral parameters used in the Warner and McIntyre gravity wave parameterization scheme. *Atmos. Chem. Phys.*, 6(12):4361–4381, doi:10.5194/acp-6-4361-2006.

ESA, 2008: *Candidate Earth Explorer Core Missions - Report for Assessment: PREMIER - PRocess Exploitation through Measurements of Infrared and millimetre-wave Emitted Radiation*, volume SP-1313/5. ESA Publications Division, ESTEC, Keplerlaan 1, 2200 AG Noordwijk, The Netherlands.

Fetzer, E. J. and J. C. Gille, 1994: Gravity wave variance in LIMS temperatures. part I: Variability and comparison with background winds. *J. Atmos. Sci.*, 51(17):2461–2483, doi:10.1175/1520-0469(1994)051<2461:GWVILT>2.0.CO;2.

Fischer, H., M. Birk, C. Blom, B. Carli, M. Carlotti, T. von Clarmann, L. Delbouille, A. Dudhia, D. Ehhalt, M. Endemann, J. M. Flaud, R. Gessner, A. Kleinert, R. Koopman, J. Langen, M. López-Puertas, P. Mosner, H. Nett, H. Oelhaf, G. Perron, J. Remedios, M. Ridolfi, G. Stiller, and R. Zander, 2008: MIPAS: an instrument for atmospheric and climate research. *Atmos. Chem. Phys.*, 8(8):2151–2188, doi:10.5194/acp-8-2151-2008.

Forster, P. M. d. F. and K. P. Shine, 1997: Radiative forcing and temperature trends from stratospheric ozone changes. *J. Geophys. Res.*, 102:10841–10855, doi:10.1029/96JD03510.

Francis, G. L., D. P. Edwards, A. Lambert, C. M. Halvorson, J. M. Lee-Taylor, and J. C. Gille, 2006: Forward modeling and radiative transfer for the NASA EOS-Aura High Resolution Dynamics Limb Sounder (HIRDLS) instrument. *J. Geophys. Res.*, 111(D13301), doi:10.1029/2005JD006270.

Friedl-Vallon, F., M. Riese, G. Maucher, A. Lengel, F. Hase, P. Preusse, and R. Spang, 2006: Instrument concept and preliminary performance analysis of GLORIA. *Adv. Space Res.*, 37:2287–2291, doi:10.1016/j.asr.2005.07.075.

Fritts, D. C. and M. J. Alexander, 2003: Gravity wave dynamics and effects in the middle atmosphere. *Rev. Geophys.*, 41(1003), doi:10.1029/2001RG000106.

Geppert, G., 2010: *Numerische Verfahren zur Lösung inverser Probleme aus der Atmosphärenfernerkundung*. Master's thesis, Friedrich-Schiller-Universität Jena.

Giering, R. and T. Kaminski, 1998: Recipes for adjoint code construction. *ACM T. Math. Software*, 24:437–474, doi:10.1145/293686.293695.

Gille, J. C., J. J. Barnett, J. G. Whitney, M. A. Dials, D. Woodard, W. P. Rudolf, A. Lambert, and W. Mankin, 2003: The High-Resolution Dynamics Limb Sounder (HIRDLS) experiment on AURA. *Proc. SPIE*, 5152:161–171, doi:10.1117/12.507657.

Gille, J. C. and J. M. Russel III, 1984: The limb infrared monitor of the stratosphere: Experiment description, performance, and results. *J. Geophys. Res.*, 89:5125–5140, doi:10.1029/JD089iD04p05125.

Godson, W. L., 1953: The evaluation of infra-red radiative fluxes due to atmospheric water vapour. *Quart. J. Roy. Meteorol. Soc.*, 79:367–379.

Gordley, L. L. and J. M. Russell, 1981: Rapid inversion of limb radiance data using an emissivity growth approximation. *Appl. Optics*, 20:807–813, doi:10.1364/AO.20.000807.

Griewank, A. and A. Walther, 2008: *Evaluating Derivatives: Principles and Techniques of Algorithmic Differentiation*. Number 105 in Other Titles in Applied Mathematics. SIAM, Philadelphia, PA, 2nd edition.

Hadamard, J., 1902: Sur les problèmes aux dérivées partielles et leur signification physique. *Princeton University Bulletin*, pages 49–52.

Hanke, M., 1995: *Conjugate gradient type methods for ill-posed problems*. John Wiley & Sons.

Hanke, M., 1997: Regularizing properties of a truncated Newton-CG algorithm for nonlinear inverse problems. *Numer. Func. Anal. Opt.*, 18(9):971–993, doi:10.1080/01630569708816804.

Hansen, P. C., 1992: Analysis of discrete ill-posed problems by means of the L-curve. *SIAM Rev.*, 34(4):561–580, doi:10.1137/1034115.

Hansen, P. C. and D. P. O'Leary, 1993: The use of the L-curve in the regularization of discrete ill-posed problems. *SIAM J. Sci. Comput.*, 14(6):1487–1503, doi:10.1137/0914086.

Hase, F. and M. Höpfner, 1999: Atmospheric ray path modeling for radiative transfer algorithms. *Appl. Optics*, 38:3129–3133, doi:10.1364/AO.38.003129.

Hegglin, M. I., C. D. Boone, G. L. Manney, and K. A. Walker, 2009: A global view of the extratropical tropopause transition layer from atmospheric chemistry experiment fourier transform spectrometer O_3, H_2O, and CO. *J. Geophys. Res.*, 114(D00B11), doi:10.1029/2008JD009984.

Hertzog, A., G. Boccara, R. A. Vincent, F. Vial, and P. Coquerez, 2008: Estimation of gravity-wave momentum flux and phase speeds from long-duration stratospheric balloon flights. 2: Results from the Vorcore campaign in Antarctica. *J. Atmos. Sci.*, 65:3056–3070, doi:10.1175/2008JAS2710.1.

Hoffmann, L., 2006: Schnelle Spurengasretrieval für das Satellitenexperiment Envisat MIPAS. Technical Report JUEL-4207, Forschungszentrum Jülich, Germany. ISSN 0944-2952.

Hoffmann, L. and M. J. Alexander, 2009: Retrieval of stratospheric temperatures from Atmospheric Infrared Sounder radiance measurements for gravity wave studies. *J. Geophys. Res.*, 114(D07105), doi:10.1029/2008JD011241.

Hoffmann, L., M. Kaufmann, R. Spang, R. Müller, J. J. Remedios, D. P. Moore, C. M. Volk, T. von Clarmann, and M. Riese, 2008: Envisat MIPAS measurements of CFC-11: retrieval, validation, and climatology. *Atmos. Chem. Phys.*, 8:3671–3688, doi:10.1016/j.asr.2005.03.112.

Hoffmann, L., K. Weigel, R. Spang, S. Schroeder, K. Arndt, C. Lehmann, M. Kaufmann, M. Ern, P. Preusse, F. Stroh, and M. Riese, 2009: CRISTA-NF measurements of water vapor during the SCOUT-O_3 Tropical Aircraft Campaign. *Adv. Space Res.*, 43(1):74–81, doi:10.1016/j.asr.2008.03.018.

Hoor, P., C. Gurk, D. Brunner, M. I. Hegglin, H. Wernli, and H. Fischer, 2004: Seasonality and extent of extratropical TST derived from in-situ CO measurements during spurt. *Atmos. Chem. Phys.*, 4:1427–1442, doi:10.5194/acp-4-1427-2004.

Höpfner, M., C. Blom, T. Clarmann, F. Fischer, N. Glatthor, T. Gulde, F. Hase, C. Keim, W. Kimmig, K. Lessenich, C. Piesch, C. Sartorius, and G. Stiller, 2001: MIPAS-STR data analysis of APE-GAIA measurements. In Smith, W. (editor), *IRS 2000: Current Problems in Atmospheric Radiation; Proc. of the Internat. Radiation Symp.*, pages 1136–1139. DEEPAK Publ.

Kaczmarz, M., 1937: Angenäherte Auflösung von Systemen linearer Gleichungen. *Bull. Acad., Polon. Sci. Letter*, 5(37):355–357.

Kaminski, J. W., L. Neary, J. Struzewska, J. C. McConnell, A. Lupu, J. Jarosz, K. Toyota, S. L. Gong, J. C364t351, X. Liu, K. Chance, and A. Richter, 2008: GEM-AQ, an on-line global multiscale chemical weather modelling system: model description and evaluation of gas phase chemistry processes. *Atmos. Chem. Phys.*, 8(12):3255–3281, doi:10.5194/acp-8-3255-2008.

Keim, C., G. Y. Liu, C. E. Blom, H. Fischer, T. Gulde, M. Höpfner, C. Piesch, F. Ravegnani, A. Roiger, H. Schlager, and N. Sitnikov, 2008: Vertical profile of peroxyacetyl nitrate (PAN) from MIPAS-STR measurements over Brazil in February 2005 and its contribution to tropical UT NO_y partitioning. *Atmos. Chem. Phys.*, 8(16):4891–4902, doi:10.5194/acp-8-4891-2008.

Kiefer, M., E. Arnone, A. Dudhia, M. Carlotti, E. Castelli, T. von Clarmann, B. M. Dinelli, A. Kleinert, A. Linden, M. Milz, E. Papandrea, and G. Stiller, 2010: Impact of temperature field inhomogeneities on the retrieval of atmospheric species from MIPAS IR limb emission spectra. *Atmos. Meas. Tech.*, 3(5):1487–1507, doi:10.5194/amt-3-1487-2010.

Konopka, P., J.-U. Grooß, F. Plöger, and R. Müller, 2009: Annual cycle of horizontal in-mixing into the lower tropical stratosphere. *J. Geophys. Res.*, 114(D19):0148–0227, doi:10.1029/2009JD011955.

Lane, T. P., M. J. Reeder, and T. L. Clark, 2001: Numerical modeling of gravity wave generation by deep tropical convection. *J. Atmos. Sci.*, 58(10):1249–1274, doi:10.1175/1520-0469(2001)058<1249:NMOGWG>2.0.CO;2.

Leppkes, K. and U. Naumann, 2011: DCO/C - efficient derivative code by overloading in C++. Technical Report AIB-2011-06, RWTH Aachen.

Livesey, N., W. Van Snyder, W. Read, and P. Wagner, 2006: Retrieval algorithms for the EOS microwave limb sounder (MLS). *IEEE T. Geosci. Remote. Sens.*, 44(5):1144 – 1155, doi:10.1109/TGRS.2006.872327.

Lotz, J., 2010: *Analyse adjungierten-basierter Optimierungsverfahren unter Verwendung algorithmischen Differenzierens*. Master's thesis, RWTH Aachen.

Lotz, J., U. Naumann, and J. Ungermann, 2011: Efficient discrete adjoint computation in a spectral simulation code. Technical Report AIB-2011-05, RWTH Aachen and Forschungszentrum Jülich.

Marquardt, D. W., 1963: An algorithm for least-squares estimation of nonlinear parameters. *J. Soc. Ind. Appl. Math.*, 11:431–441.

McLandress, C., 1998: On the importance of gravity waves in the middle atmosphere and their parameterization in general circulation models. *J. Atmos. Sol. Terr. Phys.*, 60:1357–1383, doi:10.1016/S1364-6826(98)00061-3.

McLandress, C. and T. G. Shepherd, 2009: Simulated anthropogenic changes in the Brewer-Dobson circulation, including its extension to high latitudes. *J. Clim.*, 22:1516–1540, doi:10.1175/2008JCLI2679.1.

Natterer, F., 2001: *The mathematics of computerized tomography*. Society for Industrial and Applied Mathematics, Philadelphia, PA, USA.

Nocedal, J., 1980: Updating quasi-newton matrices with limited storage. *Math. Comput.*, 35:773–782.

Nocedal, J. and S. J. Wright, 2006: *Numerical Optimization*. Springer.

Nolet, G., 1985: Solving or resolving inadequate and noisy tomographic systems. *J. Comput. Phys.*, 61(3):463–482, doi:10.1016/0021-9991(85)90075-0.

Offermann, D., K.-U. Grossmann, P. Barthol, P. Knieling, M. Riese, and R. Trant, 1999: Cryogenic Infrared Spectrometers and Telescopes for the Atmosphere (CRISTA) experiment and middle atmosphere variability. *J. Geophys. Res.*, 104:16311–16325, doi:10.1029/1998JD100047.

Paige, C. C. and M. A. Saunders, 1982: LSQR: An algorithm for sparse linear equations and sparse least squares. *ACM T. Math. Software*, 8(1):43.

Piani, C., D. Durran, M. J. Alexander, and J. R. Holton, 2000: A numerical study of three-dimensional gravity waves triggered by deep tropical convection and their role in the dynamics of the qbo. *J. Atmos. Sci.*, 57(22):3689–3702, doi:10.1175/1520-0469(2000)057<3689:ANSOTD>2.0.CO;2.

Pickering, K. E., A. M. Thompson, D. P. McNamara, and M. R. Schoeberl, 1994: An intercomparison of isentropic trajectories over the south atlantic. *Mon. Weath. Rev.*, 122(5):864–879, doi:10.1175/1520-0493(1994)122<0864:AIOITO>2.0.CO;2.

Pickering, K. E., A. M. Thompson, D. P. McNamara, M. R. Schoeberl, H. F. Fuelberg, R. O. Loring Jr., M. V. Watson, K. Fakhruzzaman, and A. S. Bachmeier, 1996: TRACE a trajectory intercomparison 1. effects of different input analyses. *J. Geophys. Res.*, 101(D19):23909–23925, doi:10.1029/95JD03297.

Press, W. H., S. A. Teukolsky, W. T. Vetterling, and B. P. Flannery, 2007: *Numerical Recipes, The Art of Scientific Computing*, volume 1. Cambridge University Press, 3. edition.

Preusse, P., A. Dörnbrack, S. D. Eckermann, M. Riese, B. Schaeler, J. T. Bacmeister, D. Broutman, and K. U. Grossmann, 2002: Space-based measurements of stratospheric mountain waves by CRISTA, 1. sensitivity, analysis method, and a case study. *J. Geophys. Res.*, 107(D23)(8178), doi:10.1029/2001JD000699.

Preusse, P., S. D. Eckermann, and M. Ern, 2008: Transparency of the atmosphere to short horizontal wavelength gravity waves. *J. Geophys. Res.*, 113(D24104), doi:10.1029/2007JD009682.

Preusse, P., S. D. Eckermann, and D. Offermann, 2000: Comparison of global distributions of zonal-mean gravity wave variance inferred from different satellite instruments. *Geophys. Res. Lett.*, 27(23):3877–3880, doi:10.1029/2000GL011916.

Preusse, P., S. Schroeder, L. Hoffmann, M. Ern, F. Friedl-Vallon, J. Ungermann, H. Oelhaf, H. Fischer, and M. Riese, 2009: New perspectives on gravity wave remote sensing by spaceborne infrared limb imaging. *Atmos. Meas. Tech.*, 2(1):299–311, doi:10.5194/amt-2-299-2009.

Remedios, J. J., R. J. Leigh, A. M. Waterfall, D. P. Moore, H. Sembhi, I. Parkes, J. Greenhough, M. Chipperfield, and D. Hauglustaine, 2007: MIPAS reference atmospheres and comparisons to V4.61/V4.62 MIPAS level 2 geophysical data sets. *Atmos. Chem. Phys. Discuss.*, 7(4):9973–10017, doi:10.5194/acpd-7-9973-2007.

Rickard, G. J. and R. W. Lunnon, 2001: The Met Office upper air winds: Prediction and verification in the context of commercial aviation data. *Meteorol. Appl.*, 8(3):351–360, doi:10.1017/S1350482701003115.

Riese, M., F. Friedl-Vallon, R. Spang, P. Preusse, C. Schiller, L. Hoffmann, P. Konopka, H. Oelhaf, T. von Clarmann, and M. Höpfner, 2005: GLObal limb Radiance Imager for the Atmosphere (GLORIA): Scientific objectives. *Adv. Space Res.*, 36:989–995, doi:10.1016/j.asr.2005.04.115.

Riese, M., P. Preusse, R. Spang, M. Ern, M. Jarisch, U. Grossmann, and D. Offermann, 1997: Measurements of trace gases by the cryogenic infrared spectrometers and telescopes for the atmosphere CRISTA experiment. *Adv. Space Res.*, 19:563–566, doi:10.1016/S0273-1177(97)00172-5.

Riese, M., R. Spang, P. Preusse, M. Ern, M. Jarisch, D. Offermann, and K. U. Grossmann, 1999: Cryogenic Infrared Spectrometers and Telescopes for the Atmosphere (CRISTA) data processing and atmospheric temperature and trace gas retrieval. *J. Geophys. Res.*, 104:16349–16367, doi:10.1016/S0273-1177(97)00172-5.

Rodgers, C. D., 2000: *Inverse Methods for Atmospheric Sounding: Theory and Practice*, volume 2 of *Series on Atmospheric, Oceanic and Planetary Physics*. World Scientific.

Saad, Y., 2003: *Iterative Methods for Sparse Linear Systems*. S.I.A.M., Philadelphia, 2nd edition.

Schiller, C., J.-U. Grooß, P. Konopka, F. Plöger, F. H. Silva dos Santos, and N. Spelten, 2009: Hydration and dehydration at the tropical tropopause. *Atmos. Chem. Phys.*, 9(24):9647–9660, doi:10.5194/acp-9-9647-2009.

Sibson, R., 1981: A brief description of natural neighbour interpolation. In Barnett, V. (editor), *Interpreting Multivariate Data*, pages 21–36. John Wiley & Sons, Chichester.

Simmons, A., S. Uppala, D. Dee, and S. Kobayashi, 2006: ERA-Interim: New ECMWF reanalysis products from 1989 onwards. *ECMWF Newsletter*, 110:25–35.

Solomon, S. C., P. B. Hays, and V. J. Abreu, 1984: Tomographic inversion of satellite photometry. *Appl. Opt.*, 23(19):3409–3414, doi:10.1364/AO.23.003409.

Spang, R., L. Hoffmann, A. Kullmann, F. Olschewski, P. Preusse, P. Knieling, S. Schroeder, F. Stroh, K. Weigel, and M. Riese, 2008: High resolution limb observations of clouds by the CRISTA-NF experiment during the SCOUT-O3 tropical aircraft campaign. *Adv. Space Res.*, 42(10):1765–1775, doi:10.1016/j.asr.2007.09.036.

Steck, T. and T. von Clarmann, 2001: Constrained profile retrieval applied to the observation mode of the Michelson Interferometer for Passive Atmospheric Sounding. *Appl. Optics*, 40:3559–3571, doi:10.1364/AO.40.003559.

Steck, T., M. Höpfner, T. von Clarmann, and U. Grabowski, 2005: Tomographic retrieval of atmospheric parameters from infrared limb emission observations. *Appl. Optics*, 44(16):3291–3301, doi:10.1364/AO.44.003291.

Struzewska, J. and J. W. Kaminski, 2008: Formation and transport of photooxidants over Europe during the July 2006 heat wave; observations and GEM-AQ model simulations. *Atmos. Chem. Phys.*, 8(3):721–736, doi:10.5194/acp-8-721-2008.

Tarantola, A., 2004: *Inverse Problem Theory*. Society for Industrial and Applied Mathematics, Philadelphia.

Tikhonov, A. N. and V. Y. Arsenin, 1977: *Solutions of ill-posed problems*. Winston, Washington D.C., USA.

Twomey, S., 1977: *Introduction to the Mathematics of Inversion in Remote Sensing and Indirect Measurements*. Dover.

Ungermann, J., L. Hoffmann, P. Preusse, M. Kaufmann, and M. Riese, 2010a: Tomographic retrieval approach for mesoscale gravity wave observations by the PREMIER infrared limb-sounder. *Atmos. Meas. Tech.*, 3(2):339–354, doi:10.5194/amt-3-339-2010.

Ungermann, J., M. Kaufmann, L. Hoffmann, P. Preusse, H. Oelhaf, F. Friedl-Vallon, and M. Riese, 2010b: Towards a 3-D tomographic retrieval for the air-borne limb-imager GLORIA. *Atmos. Meas. Tech.*, 3(6):1647–1665, doi:10.5194/amt-3-1647-2010.

Weigel, K., 2009: *Infrared limb-emission observations of the upper troposphere, lower stratosphere with high spatial resolution*. Ph.D. thesis, University of Wuppertal.

Weigel, K., M. Riese, L. Hoffmann, S. Hoefer, C. Kalicinsky, P. Knieling, F. Olschewski, P. Preusse, F. Stroh, R. Spang, and C. M. Volk, 2010: CRISTA-NF measurements during the AMMA-SCOUT-O_3 aircraft campaign. *Atmos. Meas. Tech.*, 3(2):1437–1455, doi:10.5194/amt-3-1437-2010.

Weinreb, M. P. and A. C. Neuendorffer, 1973: Method to apply homogeneous-path transmittance models to inhomogenous atmospheres. *J. Atmos. Sci.*, 30:662–666, doi:10.1175/1520-0469(1973)030<0662:MTAHPT>2.0.CO;2.

Whaley, R. C., A. Petitet, and J. J. Dongarra, 2001: Automated empirical optimization of software and the ATLAS project. *Parallel Comput.*, 27(1-2):3–35, doi:10.1145/1512762.1512773.

Wright, C. J., S. M. Osprey, J. J. Barnett, L. J. Gray, and J. C. Gille, 2009: High Resolution Dynamics Limb Sounder measurements of gravity wave activity in the 2006 Arctic stratosphere. *J. Geophys. Res.*, doi:10.1029/2009JD011858.

Schriften des Forschungszentrums Jülich
Reihe Energie & Umwelt / Energy & Environment

1. **Einsatz von multispektralen Satellitenbilddaten in der Wasserhaushalts- und Stoffstrommodellierung – dargestellt am Beispiel des Rureinzugsgebietes**
   von C. Montzka (2008), XX, 238 Seiten
   ISBN: 978-3-89336-508-1

2. **Ozone Production in the Atmosphere Simulation Chamber SAPHIR**
   by C. A. Richter (2008), XIV, 147 pages
   ISBN: 978-3-89336-513-5

3. **Entwicklung neuer Schutz- und Kontaktierungsschichten für Hochtemperatur-Brennstoffzellen**
   von T. Kiefer (2008), 138 Seiten
   ISBN: 978-3-89336-514-2

4. **Optimierung der Reflektivität keramischer Wärmedämmschichten aus Yttrium-teilstabilisiertem Zirkoniumdioxid für den Einsatz auf metallischen Komponenten in Gasturbinen**
   von A. Stuke (2008), X, 201 Seiten
   ISBN: 978-3-89336-515-9

5. **Lichtstreuende Oberflächen, Schichten und Schichtsysteme zur Verbesserung der Lichteinkopplung in Silizium-Dünnschichtsolarzellen**
   von M. Berginski (2008), XV, 171 Seiten
   ISBN: 978-3-89336-516-6

6. **Politikszenarien für den Klimaschutz IV – Szenarien bis 2030**
   hrsg.von P. Markewitz, F. Chr. Matthes (2008), 376 Seiten
   ISBN 978-3-89336-518-0

7. **Untersuchungen zum Verschmutzungsverhalten rheinischer Braunkohlen in Kohledampferzeugern**
   von A. Schlüter (2008), 164 Seiten
   ISBN 978-3-89336-524-1

8. **Inorganic Microporous Membranes for Gas Separation in Fossil Fuel Power Plants**
   by G. van der Donk (2008), VI, 120 pages
   ISBN: 978-3-89336-525-8

9. **Sinterung von Zirkoniumdioxid-Elektrolyten im Mehrlagenverbund der oxidkeramischen Brennstoffzelle (SOFC)**
   von R. Mücke (2008), VI, 165 Seiten
   ISBN: 978-3-89336-529-6

10. **Safety Considerations on Liquid Hydrogen**
    by K. Verfondern (2008), VIII, 167 pages
    ISBN: 978-3-89336-530-2

11. **Kerosinreformierung für Luftfahrtanwendungen**
    von R. C. Samsun (2008), VII, 218 Seiten
    ISBN: 978-3-89336-531-9

12. **Der 4. Deutsche Wasserstoff Congress 2008 – Tagungsband**
    hrsg. von D. Stolten, B. Emonts, Th. Grube (2008), 269 Seiten
    ISBN: 978-3-89336-533-3

13. **Organic matter in Late Devonian sediments as an indicator for environmental changes**
    by M. Kloppisch (2008), XII, 188 pages
    ISBN: 978-3-89336-534-0

14. **Entschwefelung von Mitteldestillaten für die Anwendung in mobilen Brennstoffzellen-Systemen**
    von J. Latz (2008), XII, 215 Seiten
    ISBN: 978-3-89336-535-7

15. **RED-IMPACT**
    Impact of Partitioning, Transmutation and Waste Reduction Technologies on the Final Nuclear Waste Disposal
    SYNTHESIS REPORT
    ed. by W. von Lensa, R. Nabbi, M. Rossbach (2008), 178 pages
    ISBN 978-3-89336-538-8

16. **Ferritic Steel Interconnectors and their Interactions with Ni Base Anodes in Solid Oxide Fuel Cells (SOFC)**
    by J. H. Froitzheim (2008), 169 pages
    ISBN: 978-3-89336-540-1

17. **Integrated Modelling of Nutrients in Selected River Basins of Turkey**
    Results of a bilateral German-Turkish Research Project
    project coord. M. Karpuzcu, F. Wendland (2008), XVI, 183 pages
    ISBN: 978-3-89336-541-8

18. **Isotopengeochemische Studien zur klimatischen Ausprägung der Jüngeren Dryas in terrestrischen Archiven Eurasiens**
    von J. Parplies (2008), XI, 155 Seiten, Anh.
    ISBN: 978-3-89336-542-5

19. **Untersuchungen zur Klimavariabilität auf dem Tibetischen Plateau -**
    Ein Beitrag auf der Basis stabiler Kohlenstoff- und Sauerstoffisotope in Jahrringen von Bäumen waldgrenznaher Standorte
    von J. Griessinger (2008), XIII, 172 Seiten
    ISBN: 978-3-89336-544-9

20. **Neutron-Irradiation + Helium Hardening & Embrittlement Modeling of 9%Cr-Steels in an Engineering Perspective (HELENA)**
by R. Chaouadi (2008), VIII, 139 pages
ISBN: 978-3-89336-545-6

21. **in Bearbeitung**

22. **Verbundvorhaben APAWAGS (AOEV und Wassergenerierung) – Teilprojekt: Brennstoffreformierung – Schlussbericht**
von R. Peters, R. C. Samsun, J. Pasel, Z. Porš, D. Stolten (2008), VI, 106 Seiten
ISBN: 978-3-89336-547-0

23. **FREEVAL**
Evaluation of a Fire Radiative Power Product derived from Meteosat 8/9 and Identification of Operational User Needs
Final Report
project coord. M. Schultz, M. Wooster (2008), 139 pages
ISBN: 978-3-89336-549-4

24. **Untersuchungen zum Alkaliverhalten unter Oxycoal-Bedingungen**
von C. Weber (2008), VII, 143, XII Seiten
ISBN: 978-3-89336-551-7

25. **Grundlegende Untersuchungen zur Freisetzung von Spurstoffen, Heißgaschemie, Korrosionsbeständigkeit keramischer Werkstoffe und Alkalirückhaltung in der Druckkohlenstaubfeuerung**
von M. Müller (2008), 207 Seiten
ISBN: 978-3-89336-552-4

26. **Analytik von ozoninduzierten phenolischen Sekundärmetaboliten in *Nicotiana tabacum* L. cv Bel W3 mittels LC-MS**
von I. Koch (2008), III, V, 153 Seiten
ISBN 978-3-89336-553-1

27. **IEF-3 Report 2009. Grundlagenforschung für die Anwendung**
(2009), ca. 230 Seiten
ISBN: 978-3-89336-554-8

28. **Influence of Composition and Processing in the Oxidation Behavior of MCrAlY-Coatings for TBC Applications**
by J. Toscano (2009), 168 pages
ISBN: 978-3-89336-556-2

29. **Modellgestützte Analyse signifikanter Phosphorbelastungen in hessischen Oberflächengewässern aus diffusen und punktuellen Quellen**
von B. Tetzlaff (2009), 149 Seiten
ISBN: 978-3-89336-557-9

30. **Nickelreaktivlot / Oxidkeramik – Fügungen als elektrisch isolierende Dichtungskonzepte für Hochtemperatur-Brennstoffzellen-Stacks**
    von S. Zügner (2009), 136 Seiten
    ISBN: 978-3-89336-558-6

31. **Langzeitbeobachtung der Dosisbelastung der Bevölkerung in radioaktiv kontaminierten Gebieten Weißrusslands – Korma-Studie**
    von H. Dederichs, J. Pillath, B. Heuel-Fabianek, P. Hill, R. Lennartz (2009), Getr. Pag.
    ISBN: 978-3-89336-532-3

32. **Herstellung von Hochtemperatur-Brennstoffzellen über physikalische Gasphasenabscheidung**
    von N. Jordán Escalona (2009), 148 Seiten
    ISBN: 978-3-89336-532-3

33. **Real-time Digital Control of Plasma Position and Shape on the TEXTOR Tokamak**
    by M. Mitri (2009), IV, 128 pages
    ISBN: 978-3-89336-567-8

34. **Freisetzung und Einbindung von Alkalimetallverbindungen in kohlebefeuerten Kombikraftwerken**
    von M. Müller (2009), 155 Seiten
    ISBN: 978-3-89336-568-5

35. **Kosten von Brennstoffzellensystemen auf Massenbasis in Abhängigkeit von der Absatzmenge**
    von J. Werhahn (2009), 242 Seiten
    ISBN: 978-3-89336-569-2

36. **Einfluss von Reoxidationszyklen auf die Betriebsfestigkeit von anodengestützten Festoxid-Brennstoffzellen**
    von M. Ettler (2009), 138 Seiten
    ISBN: 978-3-89336-570-8

37. **Großflächige Plasmaabscheidung von mikrokristallinem Silizium für mikromorphe Dünnschichtsolarmodule**
    von T. Kilper (2009), XVII, 154 Seiten
    ISBN: 978-3-89336-572-2

38. **Generalized detailed balance theory of solar cells**
    by T. Kirchartz (2009), IV, 198 pages
    ISBN: 978-3-89336-573-9

39. **The Influence of the Dynamic Ergodic Divertor on the Radial Electric Field at the Tokamak TEXTOR**
    von J. W. Coenen (2009), xii, 122, XXVI pages
    ISBN: 978-3-89336-574-6

40. **Sicherheitstechnik im Wandel Nuklearer Systeme**
von K. Nünighoff (2009), viii, 215 Seiten
ISBN: 978-3-89336-578-4

41. **Pulvermetallurgie hochporöser NiTi-Legierungen für Implanat- und Dämpfungsanwendungen**
von M. Köhl (2009), XVII, 199 Seiten
ISBN: 978-3-89336-580-7

42. **Einfluss der Bondcoatzusammensetzung und Herstellungsparameter auf die Lebensdauer von Wärmedämmschichten bei zyklischer Temperaturbelastung**
von M. Subanovic (2009), 188, VI Seiten
ISBN: 978-3-89336-582-1

43. **Oxygen Permeation and Thermo-Chemical Stability of Oxygen Permeation Membrane Materials for the Oxyfuel Process**
by A. J. Ellett (2009), 176 pages
ISBN: 978-3-89336-581-4

44. **Korrosion von polykristallinem Aluminiumoxid (PCA) durch Metalljodidschmelzen sowie deren Benetzungseigenschaften**
von S. C. Fischer (2009), 148 Seiten
ISBN: 978-3-89336-584-5

45. **IEF-3 Report 2009. Basic Research for Applications**
(2009), 217 Seiten
ISBN: 978-3-89336-585-2

46. **Verbundvorhaben ELBASYS (Elektrische Basissysteme in einem CFK-Rumpf) - Teilprojekt: Brennstoffzellenabgase zur Tankinertisierung - Schlussbericht**
von R. Peters, J. Latz, J. Pasel, R. C. Samsun, D. Stolten
(2009), xi, 202 Seiten
ISBN: 978-3-89336-587-6

47. **Aging of ^{14}C-labeled Atrazine Residues in Soil: Location, Characterization and Biological Accessibility**
by N. D. Jablonowski (2009), IX, 104 pages
ISBN: 978-3-89336-588-3

48. **Entwicklung eines energetischen Sanierungsmodells für den europäischen Wohngebäudesektor unter dem Aspekt der Erstellung von Szenarien für Energie- und CO_2 - Einsparpotenziale bis 2030**
von P. Hansen (2009), XXII, 281 Seiten
ISBN: 978-3-89336-590-6

49. **Reduktion der Chromfreisetzung aus metallischen Interkonnektoren für Hochtemperaturbrennstofzellen durch Schutzschichtsysteme**
von R. Trebbels (2009), iii, 135 Seiten
ISBN: 978-3-89336-591-3

50. **Bruchmechanische Untersuchung von Metall / Keramik-Verbundsystemen für die Anwendung in der Hochtemperaturbrennstoffzelle**
von B. Kuhn (2009), 118 Seiten
ISBN: 978-3-89336-592-0

51. **Wasserstoff-Emissionen und ihre Auswirkungen auf den arktischen Ozonverlust**
Risikoanalyse einer globalen Wasserstoffwirtschaft
von T. Feck (2009), 180 Seiten
ISBN: 978-3-89336-593-7

52. **Development of a new Online Method for Compound Specific Measurements of Organic Aerosols**
by T. Hohaus (2009), 156 pages
ISBN: 978-3-89336-596-8

53. **Entwicklung einer FPGA basierten Ansteuerungselektronik für Justageeinheiten im Michelson Interferometer**
von H. Nöldgen (2009), 121 Seiten
ISBN: 978-3-89336-599-9

54. **Observation – and model – based study of the extratropical UT/LS**
by A. Kunz (2010), xii, 120, xii pages
ISBN: 978-3-89336-603-3

55. **Herstellung polykristalliner Szintillatoren für die Positronen-Emissions-Tomographie (PET)**
von S. K. Karim (2010), VIII, 154 Seiten
ISBN: 978-3-89336-610-1

56. **Kombination eines Gebäudekondensators mit H2-Rekombinatorelementen in Leichwasserreaktoren**
von S. Kelm (2010), vii, 119 Seiten
ISBN: 978-3-89336-611-8

57. **Plant Leaf Motion Estimation Using A 5D Affine Optical Flow Model**
by T. Schuchert (2010), X, 143 pages
ISBN: 978-3-89336-613-2

58. **Tracer-tracer relations as a tool for research on polar ozone loss**
by R. Müller (2010), 116 pages
ISBN: 978-3-89336-614-9

59. **Sorption of polycyclic aromatic hydrocarbon (PAH) to Yangtze River sediments and their components**
by J. Zhang (2010), X, 109 pages
ISBN: 978-3-89336-616-3

60. **Weltweite Innovationen bei der Entwicklung von CCS-Technologien und Möglichkeiten der Nutzung und des Recyclings von CO_2**
Studie im Auftrag des BMWi
von W. Kuckshinrichs et al. (2010), X, 139 Seiten
ISBN: 978-3-89336-617-0

61. **Herstellung und Charakterisierung von sauerstoffionenleitenden Dünnschichtmembranstrukturen**
von M. Betz (2010), XII, 112 Seiten
ISBN: 978-3-89336-618-7

62. **Politikszenarien für den Klimaschutz V – auf dem Weg zum Strukturwandel, Treibhausgas-Emissionsszenarien bis zum Jahr 2030**
hrsg. von P. Hansen, F. Chr. Matthes (2010), 276 Seiten
ISBN: 978-3-89336-619-4

63. **Charakterisierung Biogener Sekundärer Organischer Aerosole mit Statistischen Methoden**
von C. Spindler (2010), iv, 163 Seiten
ISBN: 978-3-89336-622-4

64. **Stabile Algorithmen für die Magnetotomographie an Brennstoffzellen**
von M. Wannert (2010), ix, 119 Seiten
ISBN: 978-3-89336-623-1

65. **Sauerstofftransport und Degradationsverhalten von Hochtemperaturmembranen für CO2-freie Kraftwerke**
von D. Schlehuber (2010), VII, 139 Seiten
ISBN: 978-3-89336-630-9

66. **Entwicklung und Herstellung von foliengegossenen, anodengestützten Festoxidbrennstoffzellen**
von W. Schafbauer (2010), VI, 164 Seiten
ISBN: 978-3-89336-631-6

67. **Disposal strategy of proton irradiated mercury from high power spallation sources**
by S. Chiriki (2010), xiv, 124 pages
ISBN: 978-3-89336-632-3

68. **Oxides with polyatomic anions considered as new electrolyte materials for solid oxide fuel cells (SOFCs)**
by O. H. Bin Hassan (2010), vii, 121 pages
ISBN: 978-3-89336-633-0

69. **Von der Komponente zum Stack: Entwicklung und Auslegung von HT-PEFC-Stacks der 5 kW-Klasse**
von A. Bendzulla (2010), IX, 203 Seiten
ISBN: 978-3-89336-634-7

70. **Satellitengestützte Schwerewellenmessungen in der Atmosphäre und Perspektiven einer zukünftigen ESA Mission (PREMIER)**
von S. Höfer (2010), 81 Seiten
ISBN: 978-3-89336-637-8

71. **Untersuchungen der Verhältnisse stabiler Kohlenstoffisotope in atmosphärisch relevanten VOC in Simulations- und Feldexperimenten**
von H. Spahn (2010), IV, 210 Seiten
ISBN: 978-3-89336-638-5

72. **Entwicklung und Charakterisierung eines metallischen Substrats für nanostrukturierte keramische Gastrennmembranen**
von K. Brands (2010), vii, 137 Seiten
ISBN: 978-3-89336-640-8

73. **Hybridisierung und Regelung eines mobilen Direktmethanol-Brennstoffzellen-Systems**
von J. Chr. Wilhelm (2010), 220 Seiten
ISBN: 978-3-89336-642-2

74. **Charakterisierung perowskitischer Hochtemperaturmembranen zur Sauerstoffbereitstellung für fossil gefeuerte Kraftwerksprozesse**
von S.A. Möbius (2010) III, 208 Seiten
ISBN: 978-3-89336-643-9

75. **Characterization of natural porous media by NMR and MRI techniques: High and low magnetic field studies for estimation of hydraulic properties**
by L.-R. Stingaciu (2010), 96 pages
ISBN: 978-3-89336-645-3

76. **Hydrological Characterization of a Forest Soil Using Electrical Resistivity Tomography**
by Chr. Oberdörster (2010), XXI, 151 pages
ISBN: 978-3-89336-647-7

77. **Ableitung von atomarem Sauerstoff und Wasserstoff aus Satellitendaten und deren Abhängigkeit vom solaren Zyklus**
von C. Lehmann (2010), 127 Seiten
ISBN: 978-3-89336-649-1

78. **18th World Hydrogen Energy Conference 2010 – WHEC2010 Proceedings**
Speeches and Plenary Talks
ed. by D. Stolten, B. Emonts (2010)
ISBN: 978-3-89336-658-3

78-1. **18th World Hydrogen Energy Conference 2010 – WHEC2010 Proceedings**
Parallel Sessions Book 1:
Fuel Cell Basics / Fuel Infrastructures
ed. by D. Stolten, T. Grube (2010), ca. 460 pages
ISBN: 978-3-89336-651-4

78-2. **18th World Hydrogen Energy Conference 2010 – WHEC2010 Proceedings**
Parallel Sessions Book 2:
Hydrogen Production Technologies – Part 1
ed. by D. Stolten, T. Grube (2010), ca. 400 pages
ISBN: 978-3-89336-652-1

78-3. **18th World Hydrogen Energy Conference 2010 – WHEC2010 Proceedings**
Parallel Sessions Book 3:
Hydrogen Production Technologies – Part 2
ed. by D. Stolten, T. Grube (2010), ca. 640 pages
ISBN: 978-3-89336-653-8

78-4. **18th World Hydrogen Energy Conference 2010 – WHEC2010 Proceedings**
Parallel Sessions Book 4:
Storage Systems / Policy Perspectives, Initiatives and Cooperations
ed. by D. Stolten, T. Grube (2010), ca. 500 pages
ISBN: 978-3-89336-654-5

78-5. **18th World Hydrogen Energy Conference 2010 – WHEC2010 Proceedings**
Parallel Sessions Book 5:
Stategic Analysis / Safety Issues / Existing and Emerging Markets
ed. by D. Stolten, T. Grube (2010), ca. 530 pages
ISBN: 978-3-89336-655-2

78-6. **18th World Hydrogen Energy Conference 2010 – WHEC2010 Proceedings**
Parallel Sessions Book 6:
Stationary Applications / Transportation Applications
ed. by D. Stolten, T. Grube (2010), ca. 330 pages
ISBN: 978-3-89336-656-9

78 Set (complete book series)

18th World Hydrogen Energy Conference 2010 – WHEC2010 Proceedings
ed. by D. Stolten, T. Grube, B. Emonts (2010)
ISBN: 978-3-89336-657-6

79. **Ultrafast voltex core dynamics investigated by finite-element micromagnetic simulations**
by S. Gliga (2010), vi, 144 pages
ISBN: 978-3-89336-660-6

80. **Herstellung und Charakterisierung von keramik- und metallgestützten Membranschichten für die CO_2-Abtrennung in fossilen Kraftwerken**
von F. Hauler (2010), XVIII, 178 Seiten
ISBN: 978-3-89336-662-0

81. **Experiments and numerical studies on transport of sulfadiazine in soil columns**
by M. Unold (2010), xvi, 115 pages
ISBN: 978-3-89336-663-7

82. **Prompt-Gamma-Neutronen-Aktivierungs-Analyse zur zerstörungsfreien Charakterisierung radioaktiver Abfälle**
von J.P.H. Kettler (2010), iv, 205 Seiten
ISBN: 978-3-89336-665-1

83. **Transportparameter dünner geträgerter Kathodenschichten der oxidkeramischen Brennstoffzelle**
von C. Wedershoven (2010), vi, 137 Seiten
ISBN: 978-3-89336-666-8

84. **Charakterisierung der Quellverteilung von Feinstaub und Stickoxiden in ländlichem und städtischem Gebiet**
von S. Urban (2010), vi, 211 Seiten
ISBN: 978-3-89336-669-9

85. **Optics of Nanostructured Thin-Film Silicon Solar Cells**
by C. Haase (2010), 150 pages
ISBN: 978-3-89336-671-2

86. **Entwicklung einer Isolationsschicht für einen Leichtbau-SOFC-Stack**
von R. Berhane (2010), X, 162 Seiten
ISBN: 978-3-89336-672-9

87. **Hydrogen recycling and transport in the helical divertor of TEXTOR**
by M. Clever (2010), x, 172 pages
ISBN: 978-3-89336-673-6

88. **Räumlich differenzierte Quantifizierung der N- und P-Einträge in Grundwasser und Oberflächengewässer in Nordrhein-Westfalen unter besonderer Berücksichtigung diffuser landwirtschaftlicher Quellen**
von F. Wendland et. al. (2010), xii, 216 Seiten
ISBN: 978-3-89336-674-3

89. **Oxidationskinetik innovativer Kohlenstoffmaterialien hinsichtlich schwerer Lufteinbruchstörfälle in HTR´s und Graphitentsorgung oder Aufarbeitung**
von B. Schlögl (2010), ix, 117 Seiten
ISBN: 978-3-89336-676-7

90. **Chemische Heißgasreinigung bei Biomassenvergasungsprozessen**
von M. Stemmler (2010), xv, 196 Seiten
ISBN: 978-3-89336-678-1

91. **Untersuchung und Optimierung der Serienverschaltung von Silizium-Dünnschicht-Solarmodulen**
von S. Haas (2010), ii, 202 Seiten
ISBN: 978-3-89336-680-4

92. **Non-invasive monitoring of water and solute fluxes in a cropped soil**
by S. Garré (2010), xxiv, 133 pages
ISBN: 978-3-89336-681-1

93. **Improved hydrogen sorption kinetics in wet ball milled Mg hydrides**
by L. Meng (2011), II, 119 pages
ISBN: 978-3-89336-687-3

94. **Materials for Advanced Power Engineering 2010**
ed. by J. Lecomte-Beckers, Q. Contrepois, T. Beck and B. Kuhn
(2010), 1327 pages
ISBN: 978-3-89336-685-9

95. **2D cross-hole MMR – Survey design and sensitivity analysis for cross-hole applications of the magnetometric resistivity**
by D. Fielitz (2011), xvi, 123 pages
ISBN: 978-3-89336-689-7

96. **Untersuchungen zur Oberflächenspannung von Kohleschlacken unter Vergasungsbedingungen**
von T. Melchior (2011), xvii, 270 Seiten
ISBN: 978-3-89336-690-3

97. **Secondary Organic Aerosols: Chemical Aging, Hygroscopicity, and Cloud Droplet Activation**
by A. Buchholz (2011), xiv, 134 pages
ISBN: 978-3-89336-691-0

98. **Chrom-bezogene Degradation von Festoxid-Brennstoffzellen**
von A. Neumann (2011), xvi, 218 Seiten
ISBN: 978-3-89336-692-7

99. **Amorphous and microcrystalline silicon applied in very thin tandem solar cells**
by S. Schicho (2011), XII, 190 pages
ISBN: 978-3-89336-693-4

100. **Sol-gel and nano-suspension electrolyte layers for high performance solid oxide fuel cells**
by F. Han (2011), iv, 131 pages
ISBN: 978-3-89336-694-1

101. **Impact of different vertical transport representations on simulating processes in the tropical tropopause layer (TTL)**
by F. Plöger (2011), vi, 104 pages
ISBN: 978-3-89336-695-8

102. **Untersuchung optischer Nanostrukturen für die Photovoltaik mit Nahfeldmikroskopie**
von T. Beckers (2011), xiii, 128 Seiten
ISBN: 978-3-89336-696-5

103. **Impact of contamination on hydrogenated amorphous silicon thin films & solar cells**
by J. Wördenweber (2011), XIV, 138 pages
ISBN: 978-3-89336-697-2

104. **Water and Organic Nitrate Detection in an AMS: Laboratory Characterization and Application to Ambient Measurements**
by A. Mensah (2011), XI, 111 pages
ISBN: 978-3-89336-698-9

105. **Entwicklung eines neuen Konzepts zur Steuerung der thermischen Ausdehnung von glaskeramischen Verbundwerkstoffen mit angepasster Fließfähigkeit am Beispiel der Hochtemperatur-Brennstoffzelle**
von E. Wanko (2011), xi, 134 Seiten
ISBN: 978-3-89336-705-4

106. **Tomographic reconstruction of atmospheric volumes from infrared limb-imager measurements**
by J. Ungermann (2011), xiv, 153 pages
ISBN: 978-3-89336-708-5

Energie & Umwelt / Energy & Environment
Band / Volume 106
ISBN 978-3-89336-708-5